TU WIEN

TECHNISCHE
UNIVERSITÄT
WIEN
Vienna University of Technology

DISSERTATION

Neuronal activation characteristics in the electrically stimulated retina - A model-based study

Ausgeführt zum Zwecke der Erlangung des akademischen Grades eines
Doktors der technischen Wissenschaften

unter der Leitung von
Prof. DDDr. Frank Rattay
Institut für Analysis und Scientific Computing (E101)

eingereicht an der Technischen Universität Wien
Fakultät für Mathematik und Geoinformation

von
Paul Werginz
Matrikelnummer: 0433526
Wimbergergasse 42/11, 1070 Wien

Wien am 8. März 2016

Acknowledgements

First of all, I would like to thank Professor Frank Rattay for his encouraging guidance and for countless discussions throughout my graduate studies. I truly could not have hoped for a better supervision and personal support. Professor Shelley Fried from Harvard Medical School has been a precious mentor and strongly supported me in getting insights into the fundamentals of electrophysiology and experimental procedures. His constructive comments and suggestions were invaluable for this dissertation. I sincerely thank Dr. Günther Zeck from University of Tübingen for accepting to be member of the jury and deeply criticizing my work.

I am pleased to have had wonderful experience with Seungwoo Lee, Maesoon Im and Vineeth Raghuram and want to thank them for the stimulating discussions during my stays in Boston. Furthermore, I am especially grateful to Alexander Hadjinicolaou for providing experimental data to this thesis. I would also like to thank my former labmate Simon Danner for sharing his expertise with me.

Finally, I would like to express gratitude to the Austrian Science Fund (FWF) for financial support of this project.

Abstract

Using inner eye prostheses, the restoration of vision to the blind has achieved a low level which hopefully will be enhanced in the future. Patients suffering from degeneration of their photoreceptors, cells which modulate light input to neuronal output, can regain visual perceptions by electrically stimulating the remaining retinal neurons. The aim of the investigated modeling approach was to contribute to the understanding of the responses of extracellularly stimulated bipolar and ganglion cells, the primary target cells of current retinal implants. Related to physiological vision, subretinal implants should primarily cause graded potentials in bipolar cells, whereas higher stimuli are needed to directly excite ganglion cells as they are more distant to the electrodes. Epiretinal implants stimulate the retina from the inner portion of the retina with the sensitively excitable axons of ganglion cells closest to the electrodes.

Plenty of *stimulus-response phenomena*, depending on stimulus strength, polarity, cell geometry, ion channel types and other geometric and electrical parameters were systematically investigated. The neural response was calculated in a two-step procedure: i) the electrical field was either obtained with the finite element method or with a simpler analytical approach for point sources and ii) the response of a model neuron was computed by employing a multi-compartment model with the applied electric field as input parameter. Additionally, a model for neurotransmitter release from ribbon synapses at bipolar cell terminals was developed in order to study the temporal impact of L-type calcium channels.

Membrane polarization was shown to be stronger for ON than for OFF bipolar cells because of their longer axonal processes. Depolarization of synaptic terminals and consequent vesicle release was only triggered by anodal subretinal stimulation. Strong depolarization above the Nernst potential of calcium, however, led to reversed calcium currents in synaptic terminals. These outward currents prevented an increase of intracellular calcium concentration and consequently less or no neurotransmitter were released. Surprisingly, by stimulating multiple bipolar cells located within a region of 100x100µm the calcium reversal led to a pronounced center-surround effect of vesicle release. That is, three stimulation regimes could be discriminated: i) stimulation at

low amplitudes did not activate bipolar cells at all (lower threshold), ii) stimulation at appropriate amplitudes only activated bipolar cells close to the stimulating electrode and iii) stimulation in the current reversal regime shut down cells located near the electrode but activated distant cells (upper threshold).

The major goal for spatial visual performance is to activate ganglion cells focally, i.e. within a closely spaced region on the retina. Membrane-specific properties such as a distinct distribution of sodium channels of different opening sensitivity ($Na_v1.2$ & $Na_v1.6$) were included into the ganglion cell model. During epiretinal cathodic stimulation, passing axons had thresholds approximately 120% higher than lowest thresholds at the proximal portion of the ganglion cell axon. Consequently, the arising operating window could be used to focally activate a number of ganglion cells without co-activating passing axons from ganglion cells located far away. Generally, thresholds were lower during cathodic stimulation and the site of spike initiation was easier to predict. Anodic stimulation, on the other hand, resulted in complicated activation patterns which hindered to derive general rules for determination of the site of spike initiation. Additionally, simulations suggest that the dendritic portion of the target ganglion cell is also of high importance in spike generation, even when stimulation is applied epiretinally. Dendritic edge compartments (i.e. fiber ends) turned out to have lowered thresholds and therefore played an important role in spike generation under certain circumstances, especially during subretinal stimulation. Furthermore, spike latency was shown to reliably act as a good predictor for site of spike initiation. Adding a noisy transmembrane current component allowed to compute spiking probability as a function of stimulus amplitude resulting in sigmoid response curves similar to experimental determined data.

In sum, the spatial and temporal response of retinal neurons was monitored during electrical stimulation with a special emphasis on neurotransmitter release in bipolar cells and the site of spike initiation in ganglion cells. Some of the conclusions could even be found using extremely simplified model neurons, others were confirmed simulating the geometric data of real cells.

Zusammenfassung

Die Entwicklung von Netzhautimplantaten ermöglicht es blinden Menschen eine einfache Art des Sehens wiederzuerlangen. Patienten, die an einer Degeneration ihrer Photorezeptoren, Zellen die das einfallende Licht in Nervensignale umwandeln, leiden, können mittels Elektrostimulation rudimentäre Seheindrücke zurückerlangen. Das Ziel der präsentierten Modellierung war es zum Verständnis der Vorgänge in der elektrisch stimulierten Netzhaut beizutragen. Subretinale Implantate im Bereich der degenerierten Photorezeptoren stimulieren in erster Linie Bipolarzellen und können weit entfernte Ganglienzellen nur mit hohen Stimulationsamplituden anregen. Mit epiretinalen Implantaten hingegen wird die Retina von der inneren Seite aus stimuliert und damit werden vorrangig die sensiblen Axone von Ganglienzellen aktiviert.

Eine Vielzahl an *Erregungs-Phänomenen* welche von Stimulusstärke, Polarität, Zellgeometrie, Ionenkanaltypen and andern geometrischen und elektrischen Parametern abhängen wurde systematisch untersucht. Die neuronale Antwort wurde in einem zweistufigen Verfahren simuliert: i) das elektrische Feld, welches von einer Elektrode hervorgerufen wird, wurde entweder mit der Methode der finiten Elemente oder mit einer einfachen analytischen Lösung für Punktquellen berechnet und ii) die resultierenden elektrischen Potenziale wurden als Eingangsparameter für ein Multi-Kompartment Modell verwendet. Zusätzlich wurde ein einfaches Synapsenmodell entwickelt, welches die Freisetzung von Neurotransmittern an Ribbon-Synapsen an den Enden von Bipolarzellen simuliert.

Es wurde gezeigt, dass längerer Axone in ON-Bipolarzellen zu einer stärkere Polarisation der Zellmembrane als in OFF-Bipoalrzellen führen. Depolarisation und die einhergehende Freisetzung von Neurotransmittern an den Enden von Bipolarzellen konnte nur durch anodische Stimulation von subretinaler Seite erzeugt werden. Stimulation von Bipolarzellen über das Nernst-Potenzial von Kalzium hinaus führte zu invertierten Kalziumströmen in den synaptischen Enden. Diese auswärtsgerichteten Ströme waren nicht dazu in der Lage die intrazelluläre Kalziumkonzentration hinreichend zu erhöhen um eine Ausschüttung von Neurotransmittern auszulösen. Überraschenderweise führten diese invertierten Kalziumströme bei Stimulation einer Vielzahl von Bipolarzellen im

Umkreis von 100x100µm zu einem ausgeprägten Center-Surround Effekt. Dabei konnten drei Stimulationsverläufe unterschieden werden: i) Stimulation mit niedrigen Amplituden war nicht in der Lage Zellen zu aktivieren (unterer Schwelle), ii) Stimulation mit mittleren Amplituden regte nur Zellen an welche nahe an der Stimulationselektrode lagen und iii) Stimulation im Regime der invertierten Ströme verhinderte Aktivität in Bipolarzellen nah an der Elektrode führte jedoch zu einer Freisetzung von neuronalen Botenstoffen in weiter entfernten Zellen (oberer Schwelle).

Das große Ziel für eine erhöhte räumliche Auflösung ist eine fokale, d.h. innerhalb eines räumlich begrenzten Gebiets, Anregung von Ganglienzellen. Die Membraneigenschaften wie die spezifische Verteilung von Natriumkanälen verschiedener Sensitivität ($Na_v1.2$ & $Na_v1.6$) wurden im Modell beachtet. Während epiretinaler Stimualtion hatten vorbeiziehende Axone einen um 120% erhöhten Schwellwert gegenüber dem niedrigsten Schwellwert im proximalen Teil des Axons. Der dadurch entstehenden Arbeitsbereich konnte dazu genutzt werden um eine kleine Anzahl von Ganglienzellen zu aktivieren ohne eine Co-Aktivierung von weit entfernten Ganglienzellen hervorzurufen. Kathodische Stimulation resultierte generell in niedrigeren Schwellwerten und der Ort der Signalentstehung war einfacher nachzuvollziehen. Für anodische Stimulation ergaben sich komplizierte Aktivierungsmuster die es verhinderten generelle Regeln für den Entstehungsort eines Aktionspotenzials abzuleiten. Zusätzlich wurde festgestellt, dass auch der dendritische Teil von Ganglienzellen während epiretinaler Stimulation zur Signalaktivierung beitragen kann. Faserenden zeigten erniedrigte Schwellwerte und spielten deshalb, unter gewissen Umständen, eine wichtige Rolle in der Entstehung von Aktionspotenzialen. Die Latenzzeit von Aktionspotenzialen wurde außerdem als guter Indikator für den Ort der Signalentstehung bestimmt. Simuliertes Zufallsrauschen des Membranpotenziales erlaubte es die Wahrscheinlichkeit für die Entstehung eines Aktionspotenzials zu berechnen und simulierte Ergebnisse deckten sich mit experimentellen Befunden.

Zusammengefasst befasste sich die vorgestellte Arbeit mit den räumlichen und zeitlichen Charakteristika des Antwortverhaltens retinaler Neurone während Elektrostimulation. Spezielles Augenmerk wurde auf die Ausschüttung neuronaler Botenstoffe in Bipolarzellen und dem Ort der Signalentstehung in Ganglienzellen gelegt. Einige der Schlussfolgerungen dieser Arbeit wurden mit vereinfachten Modellneuronen simuliert während andere mittels Geometriedaten aus Experimenten modelliert wurden.

Contents

Chapter 1

Introduction

1.1   Motivation & Background

A large number of diseases as well as severe injuries lead to motor and/or sensory impairments in humans. The reason for such malfunctions can be the interruption of neuronal signaling between the peripheral and the central nervous system. Paraplegic patients, for example, are not able to move their lower limbs because of an secession of the spinal cord which makes it impossible to control motor neurons in the legs. Another wide-spread sensory disfunction is deafness resulting from the loss of hair cells in the inner ear. In consequence, the mechanical sound waves arriving at the cochlear will not be transformed into neuronal signals. In order to overcome this specific cause of deafness cochlear implants have been developed and refined since the 1970s (Desoyer & Hochmair (1977)). Today, these devices are capable to restore auditory information to deaf people by bypassing the damaged hair cells using electrical stimulation. Major improvements in speaking and hearing up to speech comprehension can be seen in patients wearing cochlear implants, especially when implanted in young patients (Peterson *et al.* (2010)). The outstanding success of cochlear implants encouraged researchers and investors to adopt the underlying technology to assist blind patients.

Restoration of visual sensations, however, turned out to be more complicated. Whereas in cochlear implants less than 20 stimulating electrodes are sufficient to restore auditory information visual prostheses require a more sophisticated design. Multiple implantation sites can be found along the visual pathway, all of them having their assets and drawbacks. Also the vast number of over 100 million neurons and their

interconnections within the retina make it complicated to find general approaches to stimulate them in a controlled way. Furthermore, the exact functioning of the visual cortex is still being elucidated with many unknowns remaining.

The restoration of low-level vision is currently investigated using various approaches. The most common method to restore vision is to employ electrical stimulation in order to activate parts of the optic pathway. However, aside from electrical stimulation also gene therapy (Solinís *et al.* (2014)), optogenetics (Busskamp *et al.* (2010)) and small molecule photoswitches (Tochitsky *et al.* (2014)) were shown to be promising approaches to cure blindness in the future.

Generally, it is possible to activate the optic pathway using electrical stimulation at several different anatomic locations. Since the visual pathway plays an important role in signal processing approaches located at more upstream locations (i.e. closer to the retina) in the visual pathway are supposed to be the most promising. By utilizing as many parts of the remaining (and functioning) neuronal pathway as possible the stimulus and activation complexity can therefore be reduce enormously. However, depending on the disease or injury within the visual system higher centers along the optic pathway have to be activated. Electrical stimulation of the optic nerve (Sakaguchi *et al.* (2009); Veraart *et al.* (1998)) or the visual cortex (Bak *et al.* (1990); Brindley & Lewin (1968); Dobelle & Mladejovsky (1974)) was successfully utilized to elicit visual perceptions in clinical trials. More recent work on optic nerve (e.g. Lu *et al.* (2013)) and cortex (e.g. Normann *et al.* (2009)) stimulation is still in the preclinical phase. Also stimulation of the lateral geniculate nucleus (LGN) showed promising results in non-human trials (Panetsos *et al.* (2011); Pezaris & Reid (2007)). Several detailed reviews elucidating multiple aspects of vision restoration are available (e.g. Dowling (2009); Shepherd *et al.* (2013); Werginz & Rattay (2015); Zrenner (2013)). As it stands now, from the currently employed approaches electrical stimulation seems to be the most promising one.

Although tremendous progress was made in the last two decades, visual perceptions generated by electrically-driven neuro-prostheses are still not from higher quality. The complexity of multiple involved scientific issues such as biocompatibility, nano-fabrication of small stimulating elements, development of extra-ocular camera systems and wireless transmission systems and surgical procedures still hinder better results in clinical trials. The most important question, however, is how controlled and focal stimulation of neurons within the visual pathway can be achieved via electrical stimulation.

In sum, at least some of these issues will have to be solved in order to give blind people better support in their daily life routines.

1.2 Retinal implants

The subfield in visual prostheses which attracts most researchers is the field of retinal prostheses. In the recent past several groups worked on neuro-stimulators to restore rudimentary vision to the blind (subretinal: Chow *et al.* (2010); Lorach *et al.* (2015b); Rizzo (2011); Stingl *et al.* (2013); epiretinal: Keserü *et al.* (2012); Klauke *et al.* (2011); Rizzo *et al.* (2014); suprachoroidal: Ayton *et al.* (2014); Fujikado *et al.* (2007); Villalobos *et al.* (2013)). Located directly within the inner eye such devices aim to directly activate retinal neurons and therefore to take advantage of almost the whole visual pathway up to the cortex. Depending on implantation site three different major approaches can be distinguished (Fig. 1.1): i) subretinal implants which are implanted *under* the retina close to the retinal pigment epithelium; ii) epiretinal implants placed at the inner portion of the retina just contacting the inner limiting membrane and iii) suprachoroidal implants inserted outside of the choroid.

Retinal implants can further be divided by their functionality. The majority of all devices use external cameras to capture the incoming light (e.g. Rizzo (2011)). These inputs must further be transferred to the electrode carrier into the inner eye. In such a system, however, a sophisticated eye-tracking system has to be employed which balances the patients eye-movements. Another possibility which can be employed in subretinal implants is to use a multi-photodiode array that captures the incoming light is located directly within the inner eye (Stingl *et al.* (2013)). Each photodiode is connected to a stimulating element and the information about the incoming radiation can be converted into stimuli directly on the chip.

The communication from outside of the body to the implanted electronic chip is of highest importance. Some systems make use of a subdermal coil behind the ear in order to supply the implant with energy an other system information (Stingl *et al.* (2013)). Other approaches make use of wireless connections between the external and internal parts of the device, respectively (Rizzo (2011)).

Aside from standard electrical stimulation using external power sources one research group developed a photovoltaic-driven prosthesis without additional internal

Suprachoroidal implant

Choroid

Retinal pigment
epithelium

Subretinal implant

Degenerated PRs

Horizontal cells

Bipolar cells
Amacrine cells

Ganglion cells

Optic nerve fiber
Inner limiting membrane
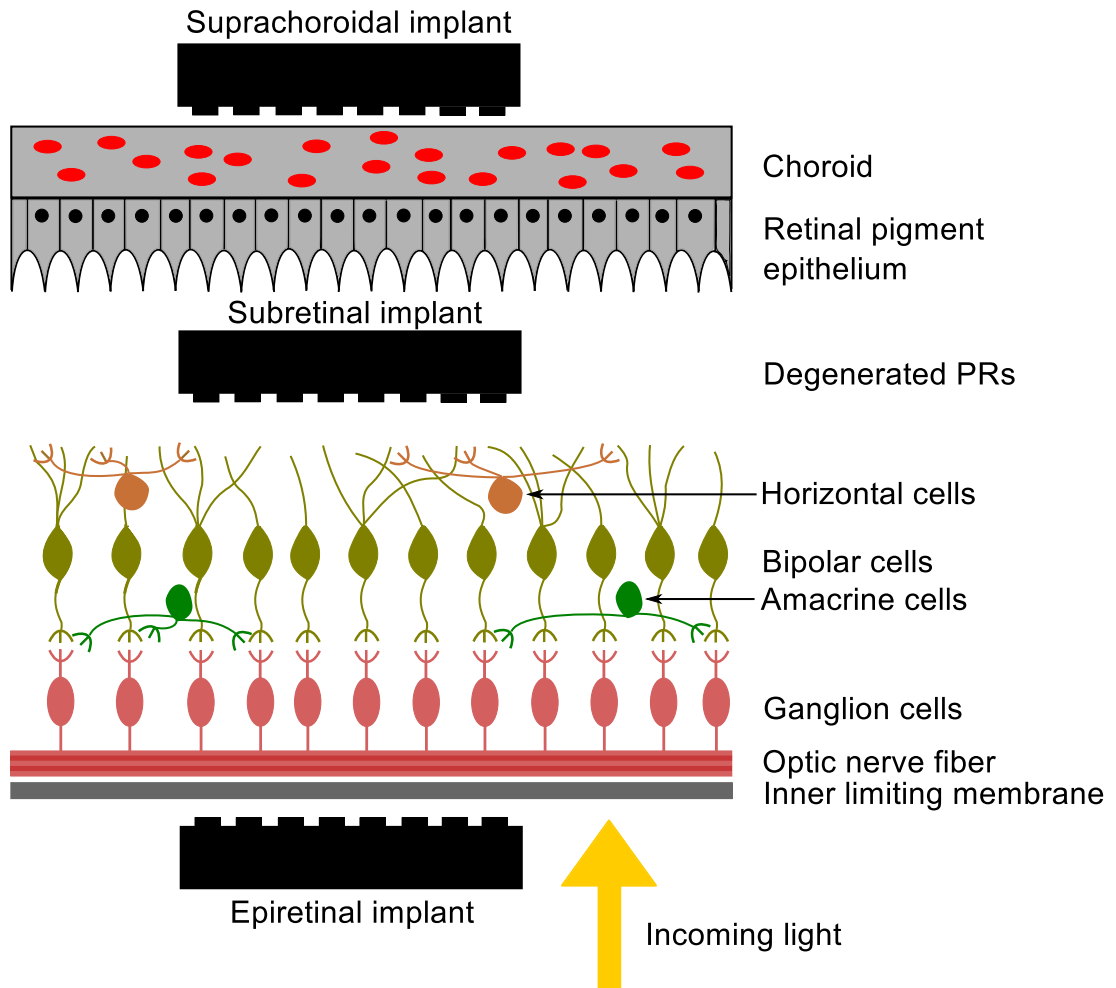
Epiretinal implant

Incoming light

Figure 1.1: **Scheme of the retina with most common locations for retinal implants** - About 120-130 million input elements (photoreceptors) are compressed by a factor of $\sim$100 to approximately 1 million output neurons (ganglion cells). Therefore, the eye carries out complex signal pre-processing within the retina in natural (i.e. healthy) condition. The 5 major retinal cell types can be divided into several subtypes which perform specific tasks during this signal-manipulation. A subretinal implant fills the region that was formerly occupied by photoreceptors. Primary target neurons during stimulation are bipolar cells. The same holds true for suprachoroidal prostheses except for the implantation site which is located further disatnt of the target neurons. It is placed outside the subretinal space behind the choroid which provides nutrition and oxygen to the retina. Epiretinal implants on the other hand face the retina from the opposite direction towards the back of the eye. These implants are attached to the inner part of the retina and their primary target neurons are ganglion cells. The illustration shows the general layout of the retina without depicting the complexity of the network and the curvature of the retina. Figure and caption from Werginz & Rattay (2015).

power supply (Lorach *et al.* (2015b)). Images are projected pixel-wise onto the subretinally implanted photovoltaic arrays which convert infrared illumination into electric stimuli (Goetz *et al.* (2013)). Irradiation wavelength was chosen to be near the infrared spectrum (915nm) in order to be able to use the device wirelessly. The system successfully elicited cortex activity in mouse and might be a promising approach for the close future because of the avoidance of profound extraocular surgical interventions (e.g. cables for power supply).

1.3 Visual pathway

In order to receive visual perception in the visual cortex several pre-processing steps have to be traversed. Starting at the front of the eye incoming light is passing through the cornea, pupil and vitreous to finally be focussed onto the retina at the very back of the eye. Photoreceptors, light sensitive cells located in the outer retina, convert the light input into an electric signal which gets forwarded to bipolar cells via neurotransmitter release at so-called ribbon synapses. The neuronal signals further cross through a complex network of various cell types in the retina to finally get processed towards the brain via ganglion cell axons that converge to the optic nerve. The optic nerve exits the eye via the optic disc, a small region lacking photoreceptors and therefore a functional blind spot. At the optic chiasm visual information from the left eye crosses to the right side and vice versa. The following optic tract ends in the lateral geniculate nucleus. From there, the optic pathway proceeds to the visual cortex at the backside of the eye at the occipital lobe. The visual cortex consists of several sub-structures V1 (the primary visual cortex) to V5.

Anatomy of the retina

The retina is a thin piece of tissue at the backside of the eye. It is circular in shape and has a thickness of approximately 0.5mm and a diameter of about 30-40mm in human (Polyak (1941)). It consists of several layers and cell types, each of it responsible for a specific task in processing visual information. Classification of the various retinal cell types has begun over one century ago (y Cajal (1893)) and is still lacking completion, however, all major cell types are known up to date.

1. INTRODUCTION

Photoreceptors (PRs) are the input elements of the retina and are sensitive to the incoming light in the visible spectrum. In the human retina two different PR types can be distinguished: i) rods that perform scotopic (low-light) vision and ii) cones, responsible for photopic (high-light) vision. In human, the majority (∼95%) of all approximately 120-130 million PRs are rods, only about 6 million PRs are cones (Osterberg (1935)). In humans three types of cones can be distinguished by their sensitivity to different wavelengths of light, thus, humans are, in contrast to other mammals, trichromates. S(hort)-type cones are most sensitive to wavelengths around 420nm (blue light), M(edium)-type cones show their maximum response sensitivity at 530nm (green light) and L(ong)-type cones respond maximally to red light with a wavelength of ∼560nm. PRs are not evenly distributed across the retina, cones are mostly present in the central area with the highest visual acuity, the so-called fovea. Rods, on the other side, are almost only present in the peripheral retina.

Bipolar cells (BCs) are second-order neurons and connect PRs with ganglion cells (GCs) and amacrine cells (ACs). Generally, BCs receive their inputs from rods and cones except for the rod BC which only makes connections to rods (Boycott *et al.* (1969)). Additionally, BC axons receive inhibitory signals from ACs (Masland (2001)). Currently, based on either immunocytochemical methods (Euler & Wässle (1995)) or ion channel expression (Fyk-Kolodziej & Pourcho (2007); Ivanova & Müller (2006)) more than ten different BC types in rat have been identified. Similarly, in mouse Waessle and coworkers reported a number of twelve BC types (Wässle *et al.* (2009)).

GCs can be divided into several subclasses based on their dendritic tree size, dendritic branching level and their measured electrophysiology. One GC can receive thousands of excitatory and inhibitory inputs by BCs and ACs shaping its output pattern (Soto *et al.* (2011)). GCs collect input data over a wide range of the retina and transform these signals into trains of action potentials (APs) along their axons. In man, approximately one million GC axons converge to the optic nerve to further process visual information towards the brain (Polyak (1941); Quigley *et al.* (1982)).

Another large fraction of retinal neurons are amacrine cells. Thus far, about 30 AC-types are known which fulfill a wide range of specific tasks in retinal signal processing (Masland (2012b)). They can be distinguished by their dendritic tree size (narrow-, small-, medium- and wide-field, (Kolb *et al.* (1981))) and further by their stratification stratum within the inner plexiform layer (IPL). Additionally, ACs can be mono-, bi-
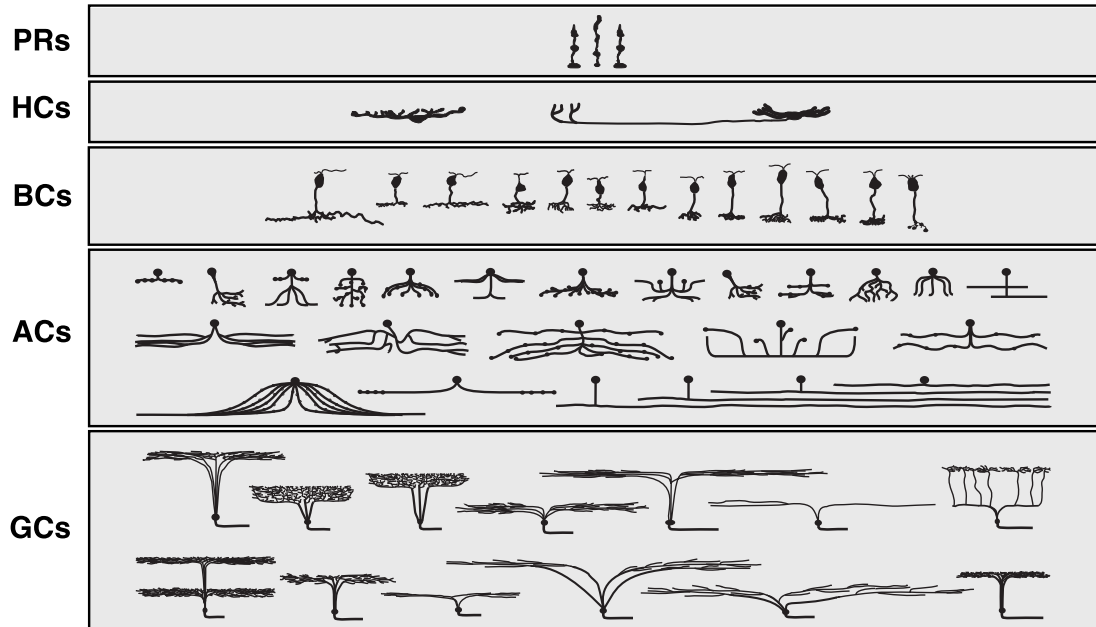
Figure 1.2: **Dominant neuron classes of the mammalian retina -** Large differences across cell types exist. Whereas some classes (PRs, BCs) are aligned vertically through the retina others (HCs, ACs) make mainly horizontal connections. Except for BCs which are from work in rat all other neuron classes are from work in rabbit. From Masland (2001)

or multi-stratified within the IPL, i.e. they have connections in various strata. ACs show diverse functionality like tuning the ON-center/OFF-center mechanism of GCs or possible paracrine functions by releasing various different neurotransmitters (Masland (2012b)).

Horizontal cells (HCs) display a rather small number compared to the total number of retinal neurons. Whereas in mammals two types of HCs can be found rat and mice only display one HC type (Masland (2001)). HCs are thought to control contrast levels between adjacent light and dark regions.

For deeper insights into classification and function of the retina multiple extensive reviews are available (e.g. Euler *et al.* (2014); Masland (2001, 2012a); Wässle (2004)).

1.4 Pathology of the retina

Depending on the site and dimension of the affecting disease the location for a visual prostheses has to be chosen. In the case of a damaged optic nerve, for example, it does

not make any sense to employ a retinal prosthesis since the generated signals will not be transferred into the cortex where the final visual perception arises. However, when talking about the usage of retinal prostheses two major causes for blindness can be discerned: Retinitis pigmentosa (RPI) and age-related macular degeneration (AMD). Both of these diseases lead to prolonged photoreceptor loss and therefore to partial and consequent total blindness. Patients suffering from either one of these diseases are the main targets for retinal prostheses.

The term *retinitis pigmentosa* has a long history in medicine. It was mentioned the first time back in the 19th century and since then a large group of hereditary diseases gets summarized under this term (Inglehearn (1998)). It is the main reason for photoreceptor loss and consequent blindness (Zrenner *et al.* (1992)). RPI progresses in the following way: After an impaired night vision in an early stage a decreasing visual field (tunnel vision) affects the visual performance strongly. The prevalence of RPI is estimated to be between 1/3000 and 1/7000 and worldwide several million patients are affected (Haim (2002)).

Multiple factors influence the development and course of AMD. AMD is the main cause for blindness in developed countries for people above the age of 50 (Smith *et al.* (2001)). Aside from genetic factors the development of AMD is also supposed to be influenced by non-genetic factors such as diet and smoking (Chakravarthy *et al.* (2010); Ristau *et al.* (2014)). In contrast to RPI, AMD starts with a loss of central vision because of the loss of photoreceptors in the central region of the human eye, the macula. AMD also does only lead to total blindness in a minority of all cases. The prevalence for AMD rises with increasing age and averages to 1/10 and 1/4 in people over 65 and 75 years of age, respectively (Ratnapriya & Chew (2013)). A steadily aging society, especially in developed countries, will lead to an expected increase to 288 million AMD patients in 2040 (Wong *et al.* (2014)).

1.5 Issues of focal stimulation

Aside from numerous technical and biological obstacles which still hinder the restoration of higher vision, the focal stimulation of target neurons seems to be the most tricky issue. A perfect retinal prosthesis would have to utilize a strategy to stimulate each remaining retinal neuron (BC and/or GC, depending on implant type) with a specific

stimulus pulse generated by one out of a manifold of stimulating elements. Since external electrical stimulation is not capable of activating single neurons like natural synaptic transmission the following three major problems arise: i) What is the *perfect* electrode size? ii) What is the *perfect* pulse form? and iii) what is the *perfect* electrode configuration?

By having a closer look on these questions one discovers a multi-dimensional parameter space which one will never be able to scan completely (neither in experimental nor in theoretical work) in order to find the perfect stimulating pulse (i.e. a pulse which activates one neuron without activating its neighbor) for each neuron. This parameter space is spanned by temporal, spatial and other parameters. Stimulus onset, duration and amplitude are highly important parameters for sure, however, also pulse shape (rectangular (cathodic, anodic), sinusoidal etc.) as well as pulse polarity (monophasic, biphasic (cathodic first, anodic first) etc.) seem to have an influence on the generated electric field and consequently on the response of the target neuron(s). Therefore, developers of future retinal implants will have to find strategies to shrink this huge parameter space to a suitable size. But how to achieve this? Lots of previous exploratory work was conducted by multiple researchers in the past. Many interesting findings were made in experimental and theoretical studies. However, the problem of how to focally activate retinal neurons (and all other neurons) still exists.

In order to find a good predictor for spike initiation Rattay presented the concept of the activating function for long fibers of constant diameter (Rattay (1986)). It states that the second derivative of the extracellular potential is the driving force for neuronal excitation. The activating function defines virtual injected currents for every compartment and thereby their first response at pulse onset (Rattay (1999)). This theoretically developed but also experimentally verified (e.g. Eickenscheidt & Zeck (2014)) assertion gave many insights into the (previously unknown) basics of extracellular electrical stimulation (i.e. What is the influence of an arbitrary electric field onto a neuronal structure?). With Rattay's tool it was possible to explain multiple phenomena such as a) why are activation thresholds for cathodic pulses lower than for anodic monophasic pulses in most cases? b) where is the site of spike initiation during extracelullar stimulation located? and c) why occurs the experimentally observed *anodal (surround) block* phenomenon (a block of AP propagation due to hyperpolarizion of neighbored fiber segments at high stimulus amplitudes, Ranck (1975))? The activating function was

further generalized to simulate the first response of arbitrary cell geometries (Rattay (1999)). However, this is again a first approach that does not include axial currents along the neural axis and inhomogeneous ion channel distributions along the neuron. This assumptions hold in case of stimulation of the peripheral nerve stimulation and lead to results which also can be explored in actual experiments. Admittedly, for more complex morphological environments containing inhomogeneities in their ion channel expression (like in the axon initial segment (AIS) of GCs, Boiko *et al.* (2003); Van Wart *et al.* (2007); Wollner & Catterall (1986)) a better hint to suitable stimulating strategies is still not available.

More recent studies also tried to find ways to activate a certain group of neurons without generating activity in another group. A tremendous improvement would be the possibility to focally activate either the ON or the OFF pathway. Whereas cells of the ON pathway depolarize due to light onset OFF cells respond with hyperpolarization of their cell membrane when light enters the retina. In natural vision these two signaling routes are separated at the synapse between PRs and BCs. During extracellular stimulation, however, BCs are not activated by synaptic inputs from PRs but are directly de- or hyperpolarized by the applied electric field. Therefore, focal stimulation of both pathways requires more knowledge on how ON and OFF BCs respond to electrical stimulation. When both pathways are activated simultaneously, the contrast in the evoked visual percepts is not likely to be very strong. Biphasic stimulation was shown to activate ON and OFF BCs differently depending on the polarity of the first pulse (cathodic or anodic first, Werginz *et al.* (2015), also see Benav (2012)). On the level of GCs high frequency stimulation (HFS) in the range of 2kHz was shown to be a promising approach to achieve differential activation of the ON and OFF pathway. An experimental study by Twyford and others (2014) revealed that by modulating the amplitude of the HFS stimulus the activity of ON and OFF GCs can be in- or decreased, respectively. A follow-up study using a computational model was also able to confirm this effect (Guo *et al.* (2014)).

Depending on the location of the implanted device one could think of two main possible stimulating strategies. If the device is located *under* the retina (subretinal and suprachoroidal) it seems to be a promising approach to stimulate BCs exclusively without activate GCs directly at the same time. If successful, a focal activation of the intermediately located BCs would lead to a quite natural signal transmission along the

visual pathway. Freeman and coworkers (2010) showed in their study that sinusoidal stimulation can elicit different responses in PRs, BCs and GCs, respectively, when the frequency gets varied. The experimentally determined results were also underlined by a simple computational approach which confirmed the possibility of focal activation of these neuronal classes. It is not totally clear so far, however, what kind of degenerations and rewiring processes BCs undergo when they do not receive PR inputs over a long time. Some studies reported strong rewiring across BCs (Jones *et al.* (2012); Marc *et al.* (2007)), however, as can be seen in clinical trials and other experimental studies BCs seem to be still viable (and functioning) under these conditions (Humayun *et al.* (1999); Santos *et al.* (1997)). Therefore, it seems that strong rewiring between retinal neurons as well as physiologic changes occur, however, these changes do not affect the functionality of these neurons. Certainly, this fact makes it more difficult to extrapolate data from healthy model animals to a potential outcome in actual clinical trials.

If stimulation is presented from the inner portion of the retina (epiretinally) GCs are the main targets for activation. The close neighborhood of the stimulating electrodes and GCs makes it more likely to elicit direct responses in these cells without activating the upstream retinal network (HCs, BCs, ACs). However, because of the morphological design of the GC layer with all of its output axons projecting towards the optic disc it is a complicated task to activate GCs close to the site of stimulation and concurrently avoiding spike generation in passing axons from GCs located far away. This co-activation was also suggested to be one one reason for deformed percepts during epiretinal stimulation in clinical trials (Nanduri *et al.* (2012)). A previous study showed that the region around the axon initial segment shows lowest threshold when stimulated extracellularly (Fried *et al.* (2009)). The reason for lowest threshold is an accumulation of sodium channels as well as geometric factors such as a decreased fiber diameter along this region. Computational studies confirmed this lowest threshold region too (Jeng *et al.* (2011); Werginz *et al.* (2014)). In sum, the described low-threshold region in closely related portions of the ganglion cell layer might be exploited to achieve focal stimulation.

Also multiple electrode configurations were tested previously aiming to achieve percepts of higher quality in retinal prostheses. Current retinal implants prefer multielectrode arrays with circular or rectangular contacts. The number of stimulating electrode varies between tens up to thousands on carriers only a few square millimeter
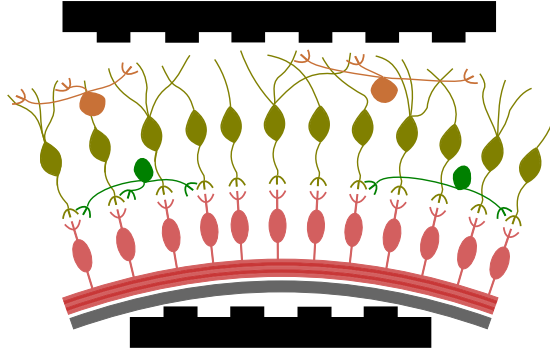
Figure 1.3: **Rigid electrode carriers and curvature of the retina lead to varying electrode-to-target distance -** Subretinal (top) implants are closely attached to the retinal surface at their centers and electrodes outside of this region have a larger distance to the target neurons. Epiretinally located implants (bottom), on the other hand, contact the inner limiting membrane (gray) at the edges of the electrode carrier and centered electrodes show larger distances to ganglion cells. Flexible multi-electrode arrays can adapt better to the surface of the retina and therefore might guarantee a more constant electrode-to-target distance (Bendali *et al.* (2015); Mathieson *et al.* (2013)).

in size. Therefore, the resolution and visual field for the patient in such devices is strongly impaired. Additionally, the diameter of stimulating electrodes is in the range of 50 up to hundreds of micrometers. Also the distance between electrode carrier and target fibers strongly varies depending on the location of the implant. Whereas sub- and epiretinal implants are assumed to be only tens of micrometer distant to their targets a suprachoroiddal prosthesis is a few hundred up to one thousand micrometers away from BCs (Ayton *et al.* (2014)). Additionally to varying surgical placement of the electrode carrier also moving implants over time were reported which seems to be important since electrode-to-target distance was shown to be a crucial factor (Ahuja *et al.* (2013)). The curvature of the eye together with inflexible electrode arrays also lead to varying electrode-to-target distance across the implants surface (Fig. 1.3). Because of the relatively small number and large size of these electrodes in contrast to the distance between target neurons it is of high importance to use the available resources precisely and efficiently.

Smaller spacing between stimulating elements will not necessarily lead to a higher spatial resolution for the patient (Behrend *et al.* (2011)). One problem occuring in closely spaced and simultaneously activated electrodes is called *electric cross-talk*

(Khalili Moghadam *et al.* (2011, 2013); Savage *et al.* (2012); Wilke *et al.* (2011)). Electric fields generated by multiple electrodes show an overlap and thus influence each other. In order to avoid unpredictable stimulating protocols and consequently unwanted neuronal activation this fact must be considered carefully. One solution to avoid electric crosstalk might be to use multipolar electrode configurations which lead to quasi-monopolar stimulation (Khalili Moghadam *et al.* (2013); Wilke *et al.* (2011)). In such a configuration multiple surrounding electrodes of the active electrode are set to ground and therefore hinder current from spreading out distantly. Another possibility for avoiding electric crosstalk is to sequentially activate stimulating electrodes. By avoiding simultaneous onset of two electrodes located next to each other the generated electric field will only be disturbed by the distal ground electrode.

In the recent past it was also proposed to apply stimulation from more than one electrode concurrently. This so-called *current steering* was proposed in several studies (e.g. Butson & McIntyre (2008); Matteucci *et al.* (2013)). For epiretinal prostheses this approach was exploited too and showed that a simple (piecewise) linear model can describe the effect of simultaneously stimulating electrodes in stimulation of single GCs (Jepson *et al.* (2014a)). Furthermore, the same group showed successful restoration of spatiotemporal visual signals during electrical stimulation (Jepson *et al.* (2014b)). However, these studies only examined focal stimulation of a small number of GCs without investigating possible activation of passing axons.

1.6 Objective & Outline

The presented work aims to elucidate crucial activation characteristics of bipolar and ganglion cells during extracellular electrical stimulation. A fast and accurate framework to compute these responses for multi-compartment models was established. Furthermore, simple analytical and realistic electrode models are introduced. The presented computational framework combines the method of finite elements (FEM) with realistic neuronal geometries and nerve fiber models as well as a mechanism to simulate synaptic vesicle release. Most results are compared to actual electrical stimulation of *in-vitro* retina. Furthermore, the *current reversal phenomenon*, an important mechanism during high amplitude stimulation hindering neurotransmitter release at BC terminals, and its consequences in the electrically stimulated retina is discussed.

1. INTRODUCTION

Substantial parts of the results section of this thesis were published previously (Werginz & Rattay (2015); Werginz *et al.* (2013, 2015)) or are submitted for review (Werginz P., Rattay F., *The impact of calcium current reversal on neurotransmitter release in the electrically stimulated retina*) or in preparation (Werginz P., Hadjinicolaou A., Fried S.I., Rattay F. and Hadjinicolaou A., Werginz P., Rattay F., Fried S.I.).

- **Chapter 2** *Methods* presents all necessary methods for computing the presented results. All computational and mathematical basics are located here.

- **Chapter 3** *Part I: Bipolar cell stimulation* presents the neuronal response of BCs during extracellular stimulation from the subretinal space.

- **Chapter 4** *Part I: Ganglion cell stimulation* contains results and a discussion of computed resonses of GCs during epi- and subretinal stimulation.

- **Chapter 5** *Conclusions* states concluding remarks on this work.

- *Appendix A* contains a detailed description of the simulation framework and an instruction how the freely available software package can be installed and used.

- *Appendix B* contains the CV of the author.

Chapter 2

Methods

This chapter describes all mathematical, computational and experimental methods necessary to compute the response of model neurons during extracellular electrical stimulation. First, the basics of compartmental modeling and modeled extracellular stimulation will be explained. Second, passive and active cell membrane models based on the seminal Hodgkin Huxley formalism will be introduced. After this, an efficient and accurate framework to obtain numerical solutions of the given equations is presented. A model of synaptic vesicle release will be introduced in section 2.7. Finally, an overall scheme of the implementation and a thorough testing procedure of the framework is presented.

2.1 Compartment models

The most common approach to model the neuronal signaling is the so-called compartmental modeling. Thereby, the modeled neuron will be represented by either one (single-compartment) or multiple (multi-compartment) segments or compartments. Whereas single-compartment models describe the whole morphology with only a single geometric shape (mostly spheres or cylinders), a multi-compartment model often comprises thousands of interconnected compartments mimicking an actual traced neuron morphology.
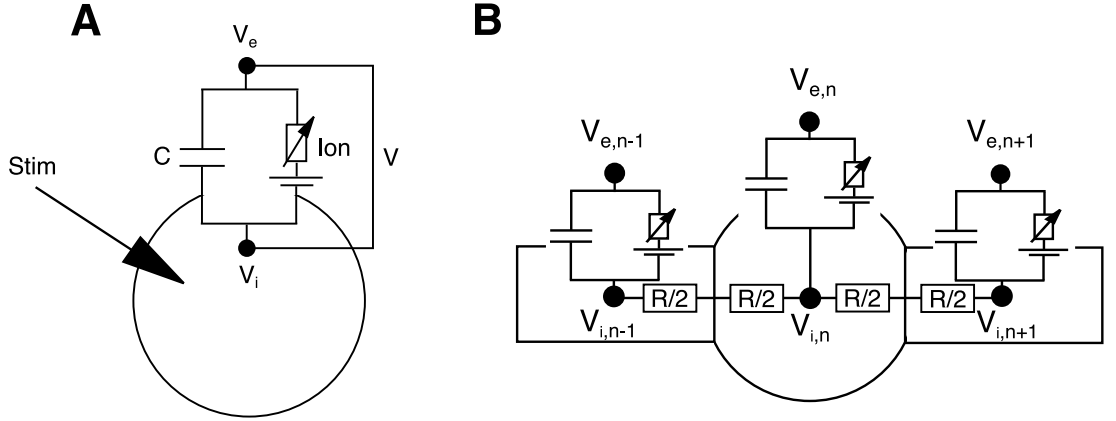
Figure 2.1: **Schematic depiction of single- and a multi-compartment models -** Whereas single-compartment models consist of only a stimulus, an ionic and a capacitive current, multi-compartment models also contain an axial component between neighbored compartments. The membrane voltage V is defined as the difference between the internal and external potential.

Single-compartment model

In order to compute the time course of the membrane potential with the single-compartment approach the following three components influence the membrane potential (Fig. 2.1A): i) a capacitive current that charges the membrane; ii) a ionic current consisting of electrically charged ions that cross the membrane through voltage- or ligand-gated ion channels and iii) an externally applied stimulus current. Applying Kirchhoffs first law leads to:

$$I_{cap} + I_{ion} + I_{stim} = 0 \quad \rightarrow \quad \frac{dV}{dt} * C + I_{ion} + I_{stim} = 0 \tag{2.1}$$

In this equation V stands for the current membrane potential, the terms I_{ion} and I_{stim} denote the ionic and an injected current, respectively. C denotes the membrane capacitance in µF. Throughout this work, the membrane potential V will always be in the unit of mV, currents will be denoted by capital letters and have the unit µA. Current densities which are indicated by lower case initial letters have the unit µA/cm^2. Time t will always be given in ms.

The calculation of the term I_{ion} will be presented in section 2.2.

Multi-compartment model

Although single-compartment models can assist exploring the basic mechanisms of action potential generation it is important to incorporate actual three-dimensional morphologies of neurons to realistically mimic their behavior (especially during extracellular stimulation).

To compute and analyze the current flow along nerve fibers the so-called neuronal cable theory was developed. This theory, again, has its fundament in the classical cable theory established by William Thomson (the later Lord Kelvin) in the mid 19th century (Thomson (1854)). At approximately the same time Hermann von Helmholtz was able to measure the velocity of signal conduction in nerve fibers which was assumed to be infinite before (Helmholtz (1850)). Although all prerequisites for further progress were already fulfilled it took another century until the next major milestones were achieved. Descriptions of active cell membranes by Hodgkin and Huxley (1952d, also see section 2.2), the formalization of a cylinder model equivalent to a dendritic tree (Rall (1962a,b)) and first utilization of simple multi-compartment models (Rall (1964)) made it possible to develop computational models of neurons.

Compartmental modeling starts with dividing a given neuronal morphology into multiple compartments which act as interconnected electric circuits. The shape of these compartments can be chosen arbitrarily, in the course of this thesis all compartments except the soma are modeled as cylinders. The soma is modeled as a sphere in almost all simulations except for comparison with the another software package (see section 2.10). The electric circuit of a simple model neuron consisting of three compartments is shown in Fig. 2.1B. The whole compartment is represented by the electric circuit in the center of the neuron which leads to second order accuracy in space (Hines & Carnevale (1997), more information in section 2.10).

Aside from modeling fiber activation by only taking intracellular currents in axial direction into account also other approaches were published (e.g. Meffin *et al.* (2012); Tahayori *et al.* (2012)). Thereby, additionally to the longitudinal mode - the solution of the neuronal cable equation - also a transversal mode with current flow perpendicular to the cell membrane are simulated.

2. METHODS

Axial currents

The core equation of a multi-compartment model can easily be obtained by extending equation 2.1 with an ohmic current that flows in axial direction through the model neuron. This equation can be interpreted as a spatially and temporally discretized version of the cable equation:

$$I_{cap_n} + I_{axial_n} + I_{ion_n} + I_{stim_n} = 0 \quad \rightarrow \quad \frac{dV}{dt} * C_n + I_{axial_n} + I_{ion_n} + I_{stim_n} = 0 \quad (2.2)$$

The component of the axial current for the nth compartment can be written as

$$I_{axial_n} = \frac{V_n - V_{n-1}}{R_n/2 + R_{n-1}/2} + \frac{V_n - V_{n+1}}{R_n/2 + R_{n+1}/2} + \ldots \quad (2.3)$$

with V_{n-1} and V_{n+1} being the membrane potential at the precedent and subsequent compartments, respectively. The dots at the end stand for possible additional neighbors at compartments with more than two neighbors, so-called node compartments. $R_n/2$ denotes the resistance from the midpoint to the end of a compartment and its unit is kΩ. For a cylindrical compartment with its cross section surface $A = r^2\pi$ (in cm^2) $R_n/2$ is calculated with

$$R_{axial_{cyl}} = \frac{\rho_i l}{A} \quad \rightarrow \quad \frac{R_n}{2} = \frac{\rho_i l_n}{2r_n^2\pi} \quad (2.4)$$

with ρ_i being the specific intracellular resistivity in kΩcm, l_n the compartment length and r_n the radius of the compartment, both in cm. For the spherical soma the resistance to its neighbors and its surface is dependent on the number and radius of the connecting compartment(s) and the resistance has to be computed separately for all neighbors to the soma (Fig. 2.2).

For multiple interconnected compartments equation 2.3 can conveniently be expressed by multiplying an *axial* matrix M with the voltage state vector V.

$$I_{axial} = M * V \quad (2.5)$$

18

$$\frac{R_{s,j}}{2} = \frac{\rho_i}{\pi} \int_0^{z_j} \frac{1}{r_s^2 - x^2} dx$$

$$= \frac{\rho_i}{2r_s\pi} ln \frac{r_s + z_j}{r_s - z_j}$$

$$A_s = 4r_s^2\pi - \sum 2r_s\pi h_j$$

$$z_j = \sqrt{r_s^2 - r_j^2}$$

$$h_j = r_s - z_j$$

Figure 2.2: **Computation of half resistance from soma to its neighbors -** To obtain the half resistance from the soma (black) to each of its neighbors ($\frac{R_{s,j}}{2}$) one has to integrate the resistance from the middle axis of the soma to the contact surface with the connecting cylindrical compartment (green). ρ_i again stands for the axial resistivity in kΩcm. r_s denotes the soma radius and r_j the radius of the connected compartment (both in cm). This formula was presented previously (Rattay *et al.* (2003); Resatz (2005)), however, its derivation was not stated and therefore it is presented in this thesis. Also the surface of the spherical soma (A_s) has to be calculated with respect of its neighbors.

M can be computed by using a connection/neighborhood matrix which contains the information of how compartments are connected to each other. Consequently, M is nonzero at connecting compartments. Fig. 2.3 shows an example of a simple geometry with five compartments and its corresponding neighborhood matrix.

2.2 Membrane models

This section provides all information how passive and active membranes can be modeled and how the term I_{ion} in equations 2.1 and 2.2 can be calculated. First, a simple passive membrane will be described. Accordingly, an active membrane models and its mathematical description will be presented in detail.

Passive membrane

The easiest way to model membrane kinetics is to incorporate a linear leak current which does not display any non-linearities. Thus, the term I_{ion} can be expressed as $I_{ion} = G_L * (V - E_L)$. Thereby, G_L denotes the conductance of the leak channel in mS,
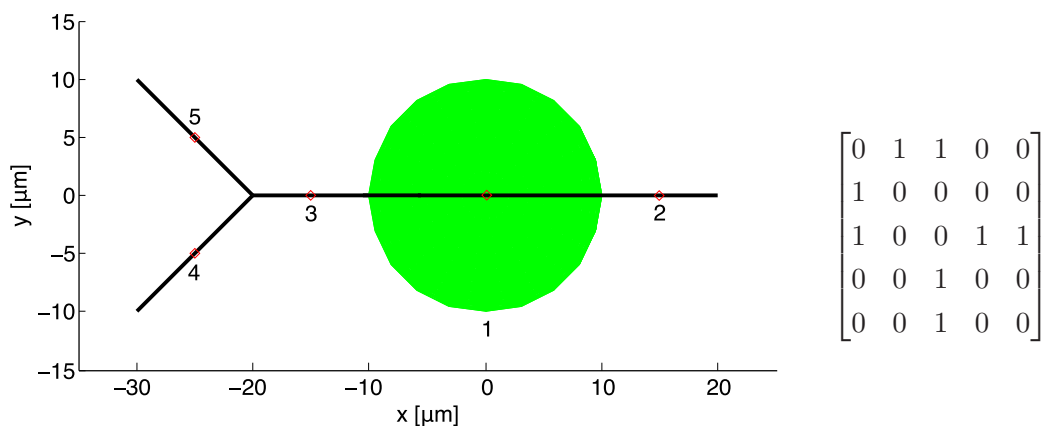
Figure 2.3: **Simple neuron geometry and corresponding neighborhood matrix -** Compartment numbers correspond to each row in the neighborhood matrix, i.e. compartment 1 (in this case the soma) connects to compartments 2 and 3. This type of matrix is used to compute the axial currents in a single matrix-vector multiplication.

V is the current membrane voltage and E_L is the reversal potential of the leak current which equals the resting potential (all in mV).

Active membrane

Hodgkin Huxley formalism

Certainly the most important work on the initiation and propagation of action potentials has been conducted by Alan Lloyd Hodgkin and Andrew Fielding Huxley in the early 1950s. In a series of articles (the most famous with the title: *A quantitative description of membrane current and its application to conduction and excitation in nerve*, (Hodgkin & Huxley (1952a,b,c,d); Hodgkin *et al.* (1952)) they and their co-author Bernard Katz presented a theoretical framework how action potential generation can be described mathematically. Aside from developing this mathematical formalism they also introduced several experimental methods necessary to be able to measure physiologic data. For their groundbreaking work they were awarded with the Nobel Prize in medicine and physiology in 1963.

Two prerequisites for their theoretical work were the development of the so-called space clamp and voltage clamp methods. The main issue of measuring ionic currents across the membrane at given membrane voltages is the presence of axial currents making it impossible to *fix* the membrane potential at a given location, i.e. a small

patch of the membrane that displays uniform membrane potential. The solution for this was the insertion of a silver wire (i.e. an electrode) in axial fiber direction (Marmont (1949)). Thus, it was possible to measure the voltage gradient across the inside and the outside of the membrane (i.e. the membrane voltage) at a predefined location without the side effect of axial currents. Additionally, the voltage clamp method to hold the membrane potential at a given voltage has been developed at about the same time. In brief, to achieve this, a configuration consisting of two electrode-pairs was set up. One pair monitors the actual membrane voltage whereas the other one injects current to keep the membrane voltage at the clamp potential. These new experimental techniques in combination made (and still make) it possible to measure the time course of an action potential as well as measuring ionic currents across a neuron membrane.

Hodgkin and Huxley recognized that a complex interplay of sodium and potassium currents lead to the - at this time - already well-known and recorded shape of the membrane voltage during an action potential. They also understood that the open and closing states of these ion channels were dependent on the current state of the membrane potential. Consequently, they were able to create a set of differential equations describing the sophisticated process of action potential generation. This HH formalism is still valid for the giant squid axon and many models for different species with a number of new ion channels have been developed since the 1950s (e.g. Fitzhugh (1961); Fohlmeister *et al.* (1990); Frankenhaeuser & Huxley (1964)). Although HH did not know biophysical properties of the contributing ion channels, their model predicts the behavior of these fairly well.

There are several conventions in the HH formalism which vary from author to author. In this study, depolarization of the membrane potential is considered to increase the membrane potential. Therefore, all action potentials point upwards. Furthermore, inflow of positive ions will be regarded to be negative and outflow to be positive. Thus, sodium currents will always be displayed as negative and potassium currents as positive, respectively. Additionally, all currents are computed as current densities with units of $\mu A/cm^2$.

2. METHODS

The total ionic current density in the HH model is computed by:

$$i_{Ion} = G_{Na} * (V - E_{Na}) + G_K * (V - E_K) + G_L * (V - E_L) \qquad (2.6)$$

G_{Na} and G_K thereby denote the conductances of the specific ion channels (sodium and potassium). $G_L * (V - E_L)$ acts as a linear leak current. E_{Na}, E_K and E_L stand for the equilibrium potentials of each ion channel type X and can be calculated with the Nernst equation:

$$E_X = \frac{RT}{2F} * ln\frac{[X]_e}{[X]_i} \qquad (2.7)$$

In this equation R stands for the gas constant ($8.3144621\frac{J}{mol*K}$), T is the temperature in Kelvin and F the Faraday constant (96485.3365C/mol). $[X]_i$ and $[X]_e$ denote the ion concentrations at the inside and outside of the cell, respectively.

Values of G_{Na} and G_K are dependent on the current membrane voltage, i.e. changing dynamically during an action potential.

$$G_{Na} = g_{Na} * m^3 * h \quad \text{and} \quad G_K = g_K * n^4 \quad \text{and} \quad G_L = g_L \qquad (2.8)$$

With g_{Na}, g_K and g_L being the maximum channel conductivities in mS/cm². m, h and n are the probabilities for the open/close state of the activating and inactivating gates, respectively, and the change of a state variable x can be modeled as:

$$\frac{dx}{dt} = \alpha_x - x * (\alpha_x + \beta_x) \qquad \text{for x...m,h,n} \qquad (2.9)$$

α and β were experimentally determined by HH to fit the measured data.

At a fixed membrane potential the state variables will reach a steady state value x_∞ for $t \to \infty$. The time constant τ_x describes how long it takes to approach this steady state.

$$x_\infty = \frac{\alpha_x}{\alpha_x + \beta_x} \qquad \tau_x = \frac{1}{\alpha_x + \beta_x} \qquad (2.10)$$

In sum, these equations are sufficient to replicate the time course of an action potential in the giant squid axon.

22

2.3   Extracellular stimulation

Aside from injecting current into one or multiple compartments a neuron can also be activated by an extracellular electric field generated by a stimulating electrode. This section presents methods to compute the influence of an electric field to a multi-compartment model. Furthermore, an analytical as well as a numerical method are presented to calculate the electric field evoked by a stimulating electrode.

In order to model extracellular stimulation I_{stim} in equation 2.2 is equal to an injected current into each compartment can be expressed by the following term (Rattay (1999)):

$$I_{stim_n} = \frac{V_{e_n} - V_{e_{n-1}}}{R_n/2 + R_{n-1}/2} + \frac{V_{e_n} - V_{e_{n+1}}}{R_n/2 + R_{n+1}/2} + \ldots \qquad (2.11)$$

Again, $R_n/2$ denotes the half resistance of each compartment, V_{e_n} stands for extracellular potentials at compartment centers.

It is important to mention that all computations in this thesis neglect the presence of the target fiber during calculation of V_e. More complex models also take this fact into account (e.g. Meffin *et al.* (2014); Tahayori *et al.* (2014)).

Analytical Solution

The most common and simplest approach to compute external potentials generated by an electrode is to assume the stimulating electrode to be a perfect point source within a homogeneous medium. In this case iso-potentials are spheres and V_e (in mV) can be calculated with:

$$V_{e_r} = \frac{\rho_e I_e}{4r\pi} \qquad (2.12)$$

with r (in cm) being the euclidean distance from the electrode, ρ_e (in Ωcm) being the resistivity of the extracellular medium and I_e (in mA) the applied current McNeal (1976)). ρ_e was set to $10^3\Omega$cm in all simulations (see *Numerical Solution* model).

2. METHODS

Numerical Solution, FEM

If the stimulating element has a more complex shape or the medium surrounding the electrode is not electrically homogeneous the method of finite elements (or finite element method, FEM) can be employed. Today, this method is a well established approach to solve complicated problems in various fields of engineering and science.

Generally, FEM bases on the simple principle to divide one large mathematical problem - a boundary value problem for partial differential equations (PDE) - into smaller parts that are simpler to solve. These smaller domains are called finite elements.

In the course of this study, all FEM computations were performed in COMSOL Multiphysics 4.4 (`https://www.comsol.com/`). For calculations of an electric field the electric currents (ec) module in the AC/DC interface was used. This module can be utilized to solve the necessary equations to obtain the distribution of the electric potential in conductive media when a current source is present. In stationary conditions and with the point form of Ohm's law the equation of continuity transforms to:

$$\nabla \cdot J = -\nabla \cdot (\sigma \nabla V - J_e) = 0 \tag{2.13}$$

with σ being the electric conductivity in S/m and J_e being an external current source in A/m^2. In order to incorporate current sources the generalized equation states:

$$-\nabla \cdot (\sigma \nabla V - J_e) = Q_j \tag{2.14}$$

Computed potential distributions (V_e) were stored in .mat files and, if necessary, loaded by the framework. In the next step, the FEM solution was linearly interpolated at the compartment centers. For each electrode geometry only one run has to be performed since the resulting external potentials are linearly dependent on the applied electrode current and can therefore easily be scaled.

The standard FEM model for epiretinal stimulation had a size of 2000µm x 2000µm x 500µm and consisted of three layers: the electrode carrier (thickness=100µm), the retina (thickness=300µm) and the sclera at the subretinal portion of the retina (thickness=100µm, Fig. 2.4). The electrode was embedded into the electrode carrier and had a height of 5µm. Electrode diameter was varied from 4.5-250µm. The electrode carrier was electrically shielded to the retina and the outer boundaries of the model were grounded. The electric resistivity of the four modeled volumes were set to the following
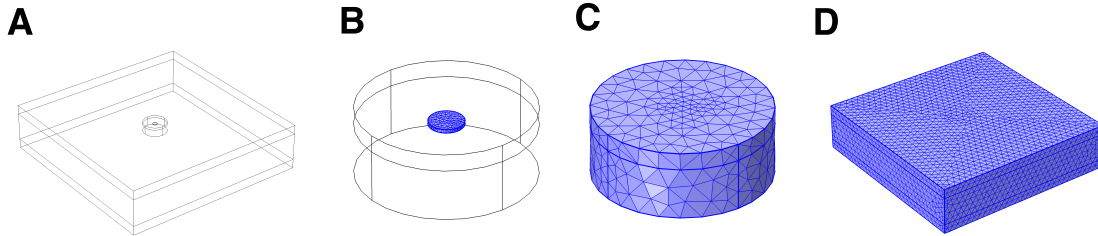
A **B** **C** **D**

Figure 2.4: **Geometry and meshing of the finite element model -** (A) The geometry of the computed finite element volume. The size of the system for epiretinal stimulation is 2000µm x 2000µm x 500µm. A stimulating electrode 50µm in diameter is placed in the middle of the volume. In the proximity of the electrode an additional volume with finer mesh discretization was incorporated. (B & C) The fine-mesh segment with the meshed electrode (blue, B) and completely meshed (C). (D) The whole meshed volume prior to computation.

values: carrier=10^{-6}S/m, retina=10^{-1}S/m (=10^3Ωcm), subretinal volume=10^{-6}S/m and the electrode=10^6S/m. Since the carrier was electrically shielded to the retina its resistivity is not of importance. Retinal resistivity was chosen to be in the mid-range of previously reported values (Greenberg *et al.* (1999); Karwoski *et al.* (1985); Kasi *et al.* (2011a)). Electrode resistivity was in the range of resistivity of platinum.

When subretinal stimulation was modeled the retina thickness was lowered to 200µm since the implant is placed in the region formerly occupied by photoreceptors. Therefore, the height of the remaining modeled retinal tissue is decreased. The electric resistivity of the four modeled volumes were set to the following values: carrier=10^{-6}S/m, retina=10^{-1}S/m (=10^3Ωcm), epiretinal volume=10^{-6}S/m and the electrode=10^6S/m. We assumed the vitreous at the epiretinal side to be replaced by silicone oil as reported in a clinical study (Besch *et al.* (2008)) and therefore specified a high resistivity as suggested previously (Benav (2012)).

The mesh process (i.e. the segmentation of the whole problem into finite elements) was individually adapted to the required accuracy. Element size was set at least to *fine*, however, if even higher accuracy was needed an additional volume close to the electrode with a finer mesh was inserted (Fig. 2.4).

Activating function

The activating function theoretically describes the influence of an extracellularly applied electric field on a straight, long, uniform nerve fiber (Rattay (1986)). In this case it is
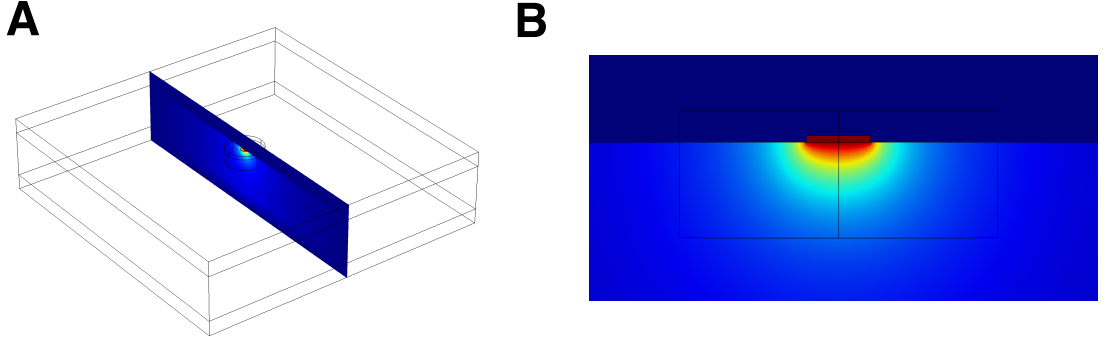
Figure 2.5: **Potential distribution within the modeled patch of the retina -** (A) Voltage plot of a slice through the volume. (B) Finer resolution of potentials on the plane in (A).

proportional to the second derivative of the applied voltage along the fiber. Positive values of the activating function indicate regions (compartments) within a fiber which are depolarized by the external stimulus and therefore are likely to initiate an action potential. Therefore, without much knowledge about the cellular properties of the stimulated fiber the activating function can give a first impression about excitation with little computational effort (e.g. Coburn (1989); Rattay (1986), Fig. 2.6).

The formulation of the *activating function for neurons of arbitrary shape* (Eq. 2.15, Rattay (1999)) can be applied on multi-compartment models and explains important features of neuronal excitation.

$$f_n = \left[\frac{V_{e,n-1} - V_{e,n}}{R_{n-1}/2 + R_n/2} + \frac{V_{e,n+1} - V_{e,n}}{R_{n+1}/2 + R_n/2} \dots \right] \frac{1}{C_n} \tag{2.15}$$

with $V_{e,n}$ being the extracellular voltage, R_n being the intracellular resistance and C_n the membrane capacitance at the nth compartment.
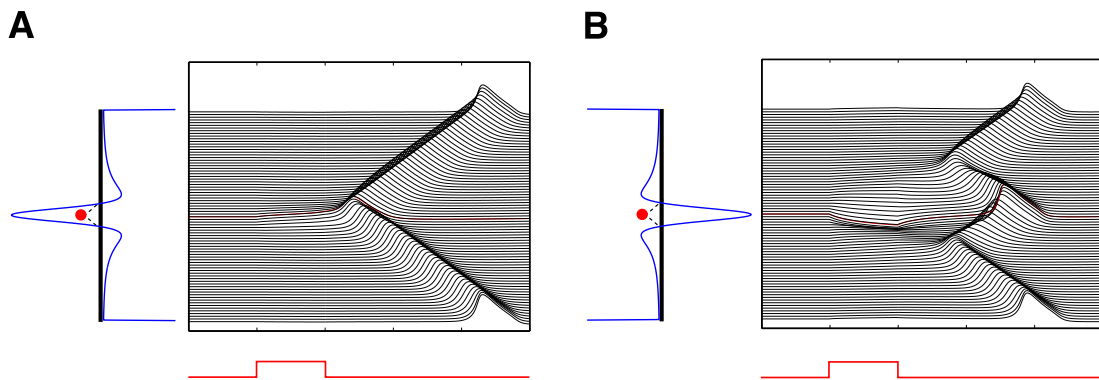
Figure 2.6: **Activating function and spike generation -** A simple stick model was stimulated extracellularly with cathodic and anodic pulses. (A) Cathodic stimulation, corresponding activating function (blue) along the fiber and spike initiation along the fiber (black). The activating function has its maximum directly below the electrode and two negative shoulders to the left and right. Consequently, one action potential is initiated at the midpoint of the fiber and propagates sideways to the fiber ends. (B) Anodic stimulation inverts the activating function and thereby also changes the site of spike initiation. Two positive shoulders lead to two spikes to the left and right of the electrode. Two spikes annihilate at the midpoint of the fiber whereas the other two spikes propagate towards the fiber edges. Zero crossings of f_n are located in a 70 degrees angle from the electrode (dashed). Stimulus was set to 35µA (cathodic) and 140µA (anodic). Model properties: *Morphology:* stick (d=1µm); *Channels:* HH; *Temp:* 20°; *Pulse:* monophasic 1ms; *Potentials:* analytical (ρ_e=0.1S/m).

2.4 Numerical Solution

This section describes how to solve the set of differential equations described so far in order to accurately and efficiently compute the response of multi-compartment models (i.e. mathematically modeled neurons) to electrical stimulation.

In powerful computing environments such as MATLAB (The Mathworks Inc., Natick, Massachusetts, United States, `www.mathworks.com`) several possibilities are available to solve an ordinary differential equation (ODE). Out-of-the-box solvers like the ODE## suite as well as external solvers such as CVODE from the Sundials package (Hindmarsh *et al.* (2005)) facilitate the application of highly efficient computing bundles. Whereas these packages are easy to implement and use they are not perfectly suited for a specific problem as the one described. Therefore, this section presents the mathematical basis for a custom written, fixed step size backward Euler solver which was used to calculate all results in this thesis. The presented solver is first order accurate in time and second order accurate in space which produces accurate results even at large time steps.

Backward Euler method

Since the ordinary differential equations in the previously presented models cannot be solved analytically, a numerical method has to be used in order to compute the solution. Generally, the output of this calculation can be considered as a numerical approximation of the solution of the ODE.

Several methods such as forward (explicit) Euler, backward (implicit) Euler, Crank-Nicholson (Crank & Nicolson (1947)) and Runge-Kutta (Kutta (1901)) method are standard and can be found in the literature. Each of these solvers has its assets and drawbacks. For the given problem, a backward Euler method was used since it is suitable for stiff-equation problems and simple to implement.

In contrast to an explicit method, using the backward Euler method makes it necessary to solve an algebraic equation (or a system of equations) in order to obtain the solution. That is, the forward Euler method directly results in the approximation at the following computation step y_{n+1} whereas using the backward Euler method an equation for y_{n+1} has to be solved. Generally, we are searching for the solution of the initial value problem

$$\frac{dy}{dt} = f(y, t) \qquad y(t = 0) = y_0 \tag{2.16}$$

$$\text{Forward Euler} \qquad y_{n+1} = y_n + f(y_n, t_n) * h \tag{2.17}$$

$$\text{Backward Euler} \qquad y_{n+1} = y_n + f(y_{n+1}, t_{n+1}) * h \tag{2.18}$$

In these equations the step size h is given by $t_n - t_{n-1}$.

Ionic currents

In order to compute the ionic current at time $t+1$ the differential equations for the state variables (x=m, h, n, c...) are solved using the backward Euler method. Compared to the forward Euler method an equation has to be solved to be able to calculate x_{t+1}.

$$\frac{dx}{dt} = \alpha_x - x * (\alpha_x + \beta_x) \tag{2.19}$$

$$\text{Forward Euler} \qquad x_{t+dt} = x_t + (\alpha_x - x_t * (\alpha_x + \beta_x)) * dt \tag{2.20}$$

$$\text{Backward Euler} \qquad x_{t+dt} = x_t + (\alpha_x - x_{t+dt} * (\alpha_x + \beta_x)) * dt \tag{2.21}$$

$$\rightarrow \qquad x_{t+dt} = \frac{x_t + dt * \alpha_x}{1 + (\alpha_x + \beta_x) * dt} \tag{2.22}$$

with dt being the time-step and αs and βs being the experimentally determined rate constants. Therefore, the whole ionic current in the HH model becomes:

$$i_{ion_{t+dt}} = g_{Na} m_{t+dt}^3 h_{t+dt}(V - E_{Na}) + g_K n_{t+dt}^4 (V - E_K) + g_L (V - E_L) \tag{2.23}$$

Hines method

To obtain the numerical approximation of the membrane voltage for all compartments at time $t + dt$ using a backward Euler solver the following equation has to be solved. With x being a vector containing all state variable $V, m, h, n \ldots$ the problem can be written in the following form:

$$V_{t+dt} = V_t + \frac{dV(t+dt, x_{t+dt})}{dt} * dt \tag{2.24}$$

with the voltage derivative being

$$\frac{dV(V_{t+dt}, x_{t+dt})}{dt} = (-M * V_{t+dt} - I_{ion,t+dt} - I_{stim,t+dt}) * \frac{1}{C} \tag{2.25}$$

Combining both equations results in

$$V_{t+dt} = V_t + (-M * V_{t+dt} - I_{ion,t+dt} - I_{stim,t+dt}) * \frac{dt}{C} \tag{2.26}$$

$$(I + M * \frac{dt}{C}) * V_{t+dt} = V_t + (-I_{ion,t+dt} - I_{stim,t+dt}) * \frac{dt}{C} \tag{2.27}$$

Thereby, I is the identity matrix in the size of M, the term $I_{ion,t+dt}$ can be obtained using equation 2.23 and the stimulus current vector at time $t + dt$ ($I_{stim,t+dt}$) is already predefined by the user.

One possibility to solve this last equation is to compute the inverse of $(I + M * \frac{dt}{C})$, however, computation of a matrix inverse using Gaussian elimination has a complexity of $O(n^3)$ and is therefore not computationally efficient for large matrices. For specific constrained problems such as unidirectional fibers without bifurcations M becomes tridiagonal and the inverse can be obtained with the much more efficient Thomas Algorithm ($O(n)$) (Thomas (1949)). However, usually neurons have many such bifurcations, therefore, the following paragraph is going to present a simple and efficient method to compute the solution of the previous equation.

Hines ordering

Hines presented a slightly modified Thomas algorithm which allows to also solve branched cables in $O(n)$ (Hines (1984)). A prerequisite for this algorithm is a so-called Hines ordering of all branches of the neuron.

A branch is a structure within the neuron without bifurcations, i.e. has a tridiagonal neighborhood matrix. A branch that is only connected at one end to the neuron is called a terminal branch or twig. A branch having neighboring branches at both ends is called a node branch. Furthermore, compartments having more than two neighbors are called nodes.

The Hines ordering procedure now comprises the following steps and Fig. 2.7 depicts how the Hines ordering procedure changes the IDs of compartments in a simple morphology:

1. Randomly pick one terminal branch which will be called trunk. Number all compartments of the branch beginning at the connecting node until the terminal of the branch is reached (branch 5 in Fig. 2.7).

2. Order all connecting branches starting at the compartment connected to the node by consequently numbering all compartments in decreasing order until the next node or a terminal compartment is reached (branches 3 and 4 in Fig. 2.7).

3. Repeat step 2 until all compartments are numbered (branches 1 and 2 in Fig. 2.7).

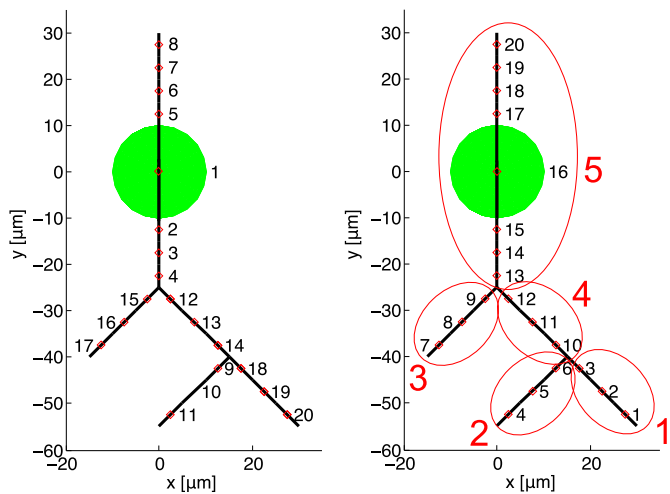| ID	T	X	Y	Z	R	P
1	1	0	10	0	10	-1
2	1	0	-10	0	10	1
3	5	0	-15	0	1	2
4	5	0	-20	0	1	3
5	5	0	-25	0	1	4
6	2	0	15	0	1	1
7	2	0	20	0	1	6
8	2	0	25	0	1	7
9	2	0	30	0	1	8
10	5	10	-45	0	1	15
11	5	5	-50	0	1	10
12	5	0	-55	0	1	11
13	5	5	-30	0	1	5
14	5	10	-35	0	1	13
15	5	15	-40	0	1	14
16	5	-5	-30	0	1	5
17	5	-10	-35	0	1	16
18	5	-15	-40	0	1	17
19	5	20	-45	0	1	15
20	5	25	-50	0	1	19
21	5	30	-55	0	1	20

Figure 2.7: **Specific ordering and numbering of compartments described by Hines -** (Left) The content of a .swc file (see section 2.5) containing the geometry of a simple model neuron. (Middle) A two-dimensional representation of the neuron described in the .swc file. The compartments are numbered as in the original file. Compartments 4 and 14 are nodes. (Right) Compartment numbering changes during the Hines ordering process. Branch number 5 was chosen to be the trunk, branch number 4 is the only node branch, branches 1,2 and 3 are terminal branches or twigs. The sequence for the forward sweep and backsubstitution in this example would be 1,2,3,4,5 and 5,4,1,2,3, respectively.

```
1 1 0 0 1 0 0 0 0 0 0 0 0 0 0 0 0 0 0 0 0        1 1 0 0 0 0 0 0 0 0 0 0 0 0 0 0 0 0 0 0 0
1 1 1 0 0 0 0 0 0 0 0 0 0 0 0 0 0 0 0 0 0        1 1 1 0 0 0 0 0 0 0 0 0 0 0 0 0 0 0 0 0 0
0 1 1 1 0 0 0 0 0 0 0 0 0 0 0 0 0 0 0 0 0        0 1 1 0 0 0 0 0 1 0 0 0 0 0 0 0 0 0 0 0 0
0 0 1 1 0 0 0 0 0 0 0 1 0 0 1 0 0 0 0 0 0        0 0 0 1 1 0 0 0 0 0 0 0 0 0 0 0 0 0 0 0 0
1 0 0 0 1 1 0 0 0 0 0 0 0 0 0 0 0 0 0 0 0        0 0 0 1 1 1 0 0 0 0 0 0 0 0 0 0 0 0 0 0 0
0 0 0 0 1 1 1 0 0 0 0 0 0 0 0 0 0 0 0 0 0        0 0 0 0 1 1 0 0 0 1 0 0 0 0 0 0 0 0 0 0 0
0 0 0 0 0 1 1 1 0 0 0 0 0 0 0 0 0 0 0 0 0        0 0 0 0 0 0 1 1 0 0 0 0 0 0 0 0 0 0 0 0 0
0 0 0 0 0 0 1 1 0 0 0 0 0 0 0 0 0 0 0 0 0        0 0 0 0 0 0 1 1 1 0 0 0 0 0 0 0 0 0 0 0 0
0 0 0 0 0 0 0 1 1 0 0 0 1 0 0 0 1 0 0        0 0 0 0 0 0 0 1 1 0 0 0 1 0 0 0 0 0 0 0
0 0 0 0 0 0 0 1 1 1 0 0 0 0 0 0 0 0 0 0 0        0 0 1 0 0 1 0 0 0 1 1 0 0 0 0 0 0 0 0 0 0
0 0 0 0 0 0 0 0 1 1 0 0 0 0 0 0 0 0 0 0 0        0 0 0 0 0 0 0 0 0 1 1 1 0 0 0 0 0 0 0 0 0
0 0 0 1 0 0 0 0 0 0 1 1 0 1 0 0 0 0 0        0 0 0 0 0 0 0 0 0 0 1 1 1 0 0 0 0 0 0 0 0
0 0 0 0 0 0 0 0 0 0 1 1 1 0 0 0 0 0 0 0 0        0 0 0 0 0 0 0 0 1 0 0 1 1 1 0 0 0 0 0 0 0
0 0 0 0 0 0 0 1 0 0 0 1 1 0 0 0 1 0 0        0 0 0 0 0 0 0 0 0 0 0 0 1 1 1 0 0 0 0 0 0
0 0 0 1 0 0 0 0 0 0 1 0 0 1 1 0 0 0 0        0 0 0 0 0 0 0 0 0 0 0 0 0 0 1 1 1 0 0 0 0
0 0 0 0 0 0 0 0 0 0 0 0 1 1 1 0 0 0        0 0 0 0 0 0 0 0 0 0 0 0 0 0 0 1 1 1 0 0 0
0 0 0 0 0 0 0 0 0 0 0 0 0 0 1 1 0 0 0        0 0 0 0 0 0 0 0 0 0 0 0 0 0 0 0 1 1 1 0 0
0 0 0 0 0 0 0 1 0 0 0 0 1 0 0 0 1 1 0        0 0 0 0 0 0 0 0 0 0 0 0 0 0 0 0 0 1 1 1 0
0 0 0 0 0 0 0 0 0 0 0 0 0 0 0 0 1 1 1        0 0 0 0 0 0 0 0 0 0 0 0 0 0 0 0 0 0 1 1 1
0 0 0 0 0 0 0 0 0 0 0 0 0 0 0 0 0 1 1        0 0 0 0 0 0 0 0 0 0 0 0 0 0 0 0 0 0 0 1 1
```

Figure 2.8: **Neighborhood matrices before and after Hines ordering -** (Left) The neighborhood matrix of the neuron in Fig. 2.7 with all compartments in random order. The main diagonal is indicated by blue '1'. (Right) The neighborhood matrix after the Hines ordering algorithm was employed. In the lower triangular portion non-zero elements only occur in rows of node compartments any more. Each of these far-off nonzero elements can now be eliminated in one single step, therefore the complexity of the Hines algorithm is still $O(n)$.

After this ordering process the neighborhood matrix is almost tridiagonal except for nonzero elements in rows of node compartments which is displayed in Fig. 2.8.

Following this procedure, all branches are numbered and ordered correctly and a two step procedure can be used to solve the equation $M * V_{t+dt} = B$ with M being the Hines matrix, V_{t+dt} the voltage vector at time $t + dt$ and B the right hand side of equation 2.27. Each branch that is not a twig or the trunk is called a node branch. In a first step called forward sweep, the sequence of branches is 1) twigs, 2) node branches 3) trunk whereas during backsubstitution the order is inverted to 1) trunk, 2) node branches 3) twigs.

The pseudo code for solving the governing equation for V_{t+dt} now reads:

Forward sweep:

for i = second compartment of branch : last compartment of branch

$$M_{i,i} = M_{i,i} - M_{i,i-1} * \left(\frac{M_{i,i-1}}{M_{i-1,i-1}}\right)$$

$$B_i = B_i - B_{i-1} * \left(\frac{M_{i,i-1}}{M_{i-1,i-1}}\right)$$

if last segment j is connected to a node k

$$M_{k,k} = M_{k,k} - M_{j,k} * \left(\frac{M_{k,j}}{M_{j,j}}\right)$$

$$B_k = B_k - B_j * \left(\frac{M_{k,j}}{M_{j,j}}\right)$$

end

end

Backsubstitution:

if last segment j is connected to a node k

$$V_j = \frac{B_j - V_k * M_{j,k}}{M_{j,j}}$$

else

$$V_j = \frac{B_j}{M_{j,j}}$$

end

for i = next to the last compartment of branch : first compartment of branch

$$V_j = \frac{V_{i-1} * M_{i,i-1}}{M_{i,i}}$$

end

2.5   Neuron morphologies

This section provides all necessary information about the geometrical properties of the used model neurons. First, the used file format to store morphologies will be described. Subsequently, retinal bipolar cell and ganglion cell morphologies are presented.

Three-dimensional representations of neurons are highly important in order to compute accurate computational results since the geometrical properties of a neuron strongly influence its response to electrical stimulation. Therefore, in this thesis simplified model neurons, actual traced neurons from an online database (`www.neuromorpho.org`, (Ascoli *et al.* (2007))) and reconstructed neurons from available publications were used. For testing of accuracy and performance simple stick models were employed.

SWC file format

Storage of the geometry of a neuron as well as its connectivity can be done in several formats. The presented model employs .swc files as inputs to specify neuronal morphologies. This format is widely used in the neuroscience community because of its simple layout and the fact that many online databases store their data in .swc files. Generally, .swc files store each compartment of a cell geometry in single line except for the soma which can consist of 2 or more compartments:

ID	TYPE	X	Y	Z	RADIUS	PARENT
1	1	0	0	-10	10	-1
2	1	0	0	10	10	1
3	2	0	0	20	1	2
4	3	0	0	-20	3	1

$$\vdots$$

with ID being an index incrementing from line to line and TYPE being a specifier for the compartment origin within the cell (soma, dendrite, axon etc.). X, Y and Z are the three-dimensional coordinates of the compartment endpoint, RADIUS is the compartment radius and PARENT stores the ID of the connected parent compartment (and therefore its start coordinate). The cells soma always acts as the starting point of a neuron, therefore, the parent of the first soma compartment (ID '1') is indicated by '-1'.
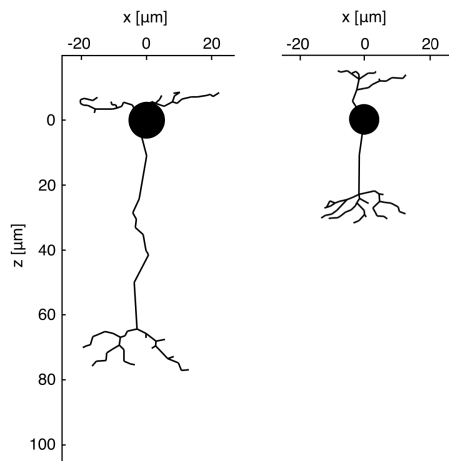
Figure 2.9: **ON and OFF BC morphologies reconstructed by Benav (2012) from Euler and Waessle (1995) -** Both morphologies were already used in various publications (Encke *et al.* (2013); Werginz *et al.* (2013, 2015)). (Left) A type 9 ON BC with a total length (z-dimension) of about 90µm. (Right) The type 2 OFF BC is shorter (length approximately 50µm) than the ON BC. Soma diameters of both cells are 10.96µm (ON) and 9.94µm (OFF), respectively. Varying compartment diameters are not shown.

BC morphologies

In order to simulate the response of BCs two previously published morpholgies were used (Encke *et al.* (2013); Werginz *et al.* (2013, 2015)). A rat type 9 ON and a type 2 OFF BC show considerable differences in their geometry. Whereas the ON BC is longer and stratifies in the inner portion of the IPL the OFF BC connects to its following neurons (GCs and ACs) in the very outer segment of the IPL (Fig. 2.9). Compartment length was below 5µm in both BCs and except for the spherical soma all compartments (ON=107, OFF=86) were modeled as cylinders.

GC morphologies

In various online databases a large number of traced GC morphologies can be found. However, many neuronal mechanisms can also be examined by using simplified model neurons without the need to compute the response of thousands of compartments which is computationally expensive. Therefore, a simplified model GC was used mostly in
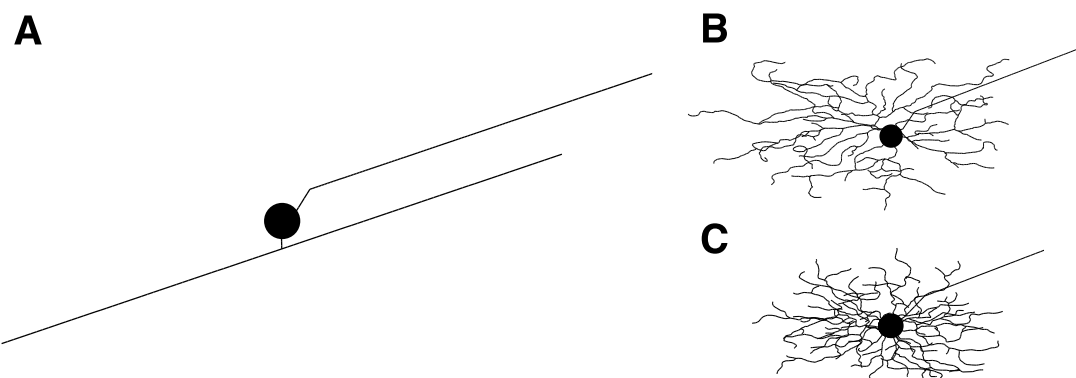
Figure 2.10: **GC morphologies used in this study -** (A) The mostly used model neuron with a detailed axonal geometry and a simplified dendritic tree. (B & C) Traced GC morphologies also used for some simulations. Varying compartment diameters are not shown.

this study (Fig. 2.10A, see also Rattay (2014)). The dendritic tree consisted of a short vertical part 10µm in length (diameter 4µm) and a horizontal part 500µm long (diameter 2µm). The spherical soma consisted of one compartment and had a diameter of 20µm. The axon hillock, 30µm long, had a diameter of 3µm. The AIS (40µm in length) diameter was tapered from 3-0.8µm followed by a 90µm long thin segment (diameter 0.8µm). The unmyelinated axon was extended for at least 800µm and had a diameter of 1µm. Compartment length was between 5 and 6µm and all >310 compartments except the spherical soma were modeled as cylinders.

Aside from the simplified model neuron also traced GC morphologies as shown in Fig. 2.10B & C were used in some simulations. These morphologies were either obtained from `www.neuromorpho.org` or from a previous publication by Guo and coworkers (2013).

2.6 BC model

The presented BC membrane dynamics are simplified to a minimum. A thorough previous study by Benav (2012) revealed a large number of different ion channels that are located in BCs. However, these channels did not have a significant influence on the membrane potential in terminal compartments and therefore most of them are neglected in this study.

Except for the synaptic terminals only a leak current is incorporated into the model. In order to compute the intracellular calcium concentration close to synaptic ribbons a L-type calcium channel built into terminal compartments. The channel has the activation kinetics taken from Sikora and coworkers (2005) which were actually fitted to tiger salamander data from older studies (Maguire *et al.* (1989); Thoreson (2000)). The presented dynamics, however, also resemble rat data (Hu *et al.* (2009a)) quite closely. Thus, ionic currents in the BC model are computed by

$$i_{ion} = i_{Ca} + i_L \qquad with \qquad i_{Ca} = g_{Ca}c^3(V - E_{Ca}) \qquad i_L = g_L(V - E_L) \quad (2.28)$$

g_{Ca} and g_L again represent the ion channel conductance along the cells membrane (g_{Ca}=0 for non-terminal compartments). The activation gate variable c computes equally as describe previously and αs and βs are shown below.

$$\alpha_c = \frac{-0.3(V + 70)}{exp(-0.1(V + 70)) - 1} \qquad \beta_c = 10exp(-(V + 38)/9) \qquad (2.29)$$

The resting potential of both BCs and E_L were set to -50mV which is close to values used in the past (-60mV and -53mV in Oltedal & Hartveit (2010) and Benav (2012), respectively). E_{Ca} was set to a fixed value of 20mV which can be obtained from available I-V[1] curves (e.g. Hu *et al.* (2009a)). The change of the intracellular calcium concentration is computed by two processes: i) flow of calcium through ion channels (active) and ii) sequestering of calcium ions with a time constant τ (passive):

$$\frac{d[Ca^{++}]_i}{dt} = -\frac{Ai_{Ca}}{2VF} - \frac{[Ca^{++}]_i - [Ca^{++}]_{res}}{\tau_{Ca}} \qquad (2.30)$$

2.7 Synapse model

In order to compute the synaptic release from bipolar cell terminals a simple synaptic release model was established (Fig. 2.11). Generally, the filling of the four vesicle pools is determined by their current pool states and four rate constants for refill and release (dynamic modeling). Additionally, the intracellular calcium concentration in BC synaptic terminals is used as a parameter and therefore governs exocytosis.

---

[1]An I-V curve describes the current-voltage characteristic, i.e. elicited (inside or outside) currents are plotted against clamp voltages.

2. METHODS

The model is able to generate release with a fast transient component and a longer sustained component as determined in experiments (Singer & Diamond (2006), see section 3.4). Therefore, the model consists of four vesicle pools (Fig. 2.11): the cytoplasmatic pool (C) which acts as a source of free vesicle which can bind to the release sites; a pool of vesicles tethered to the synaptic ribbon - the releasable pool (RP); a pool containing vesicles which are located close to the fusion site and which are already primed for release - the readily releasable pool (RRP); and the pool of all vesicles which have undergone exocytosis - the exocytosis pool (E).

The refill rates for the RP and the RRP are modeled by

$$\rho_{RP} = \overline{\rho_{RP}}\frac{RP_0 - RP_t}{C_0} \quad and \quad \rho_{RRP} = \overline{\rho_{RRP}}\frac{RRP_0 - RRP_t}{C_0} \tag{2.31}$$

with C_0, RP_0 and RRP_0 being the initial fillings of the three pools C, RP and RRP, respectively. RP_t and RRP_t denote the current pool state at time t. $\overline{\rho_{RP}}$ and $\overline{\rho_{RRP}}$ are the refill rate constants of the two release pools and are set to 0.25s^{-1} in agreement with a previous experimental study (Singer & Diamond (2006)).

Release of vesicles from the RP and RRP to the exocytosis pool is modeled by a Poisson process. The exocytosis rate constants are further dependent on the current intracellular calcium concentration near the ribbon and the current pool state of the release pools. If the conditional expressions

$$rand \leqslant rate_{RP} \quad and \quad rand \leqslant rate_{RRP} \tag{2.32}$$

with $rand$ being Gaussian (0,1) and

$$rate_{RP} = 1 - exp^{-\alpha_{RP}*[Ca^{++}]_i*RP*dt} \quad and \quad rate_{RRP} = 1 - exp^{-\alpha_{RRP}*[Ca^{++}]_i*RRP*dt}$$
$$\tag{2.33}$$

are true a vesicle is released either from the RP or the RRP. Thereby, α_{RP} and α_{RRP} are the release rate constants of the RP and RRP, respectively, and $[Ca^{++}]_i$ denotes the intracellular calcium concentration in the synaptic terminal. Again, RP and RRP are the current pool states. dt stands for the simulation time step.

Initial pool sizes were fixed in all simulations and all pools were totally filled at the beginning of all simulations except otherwise stated. The fast pool had a capacity 6 vesicles (Singer & Diamond (2006)), the slow pool was 5 times larger (30 vesicles as
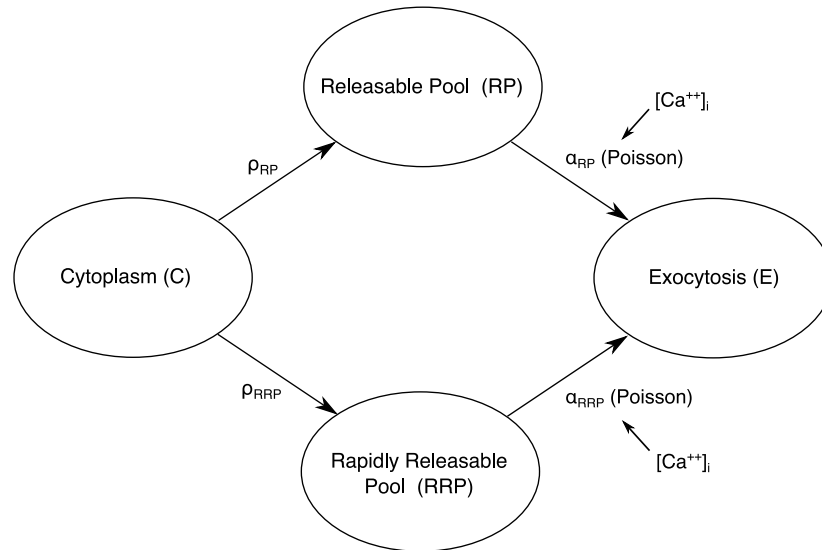
Figure 2.11: **Schematic diagram of the synapse model -** Four pools are modeled to mimic experimentally determined results from rat bipolar cells (Singer & Diamond (2006)). From the cytoplasmatic pool C vesicles can be refilled to the two release pools RP and RRP with the two refill rate constants ρ_{RP} and ρ_{RRP}. The RP characterizes vesicles located in the upper rows of the ribbon which have to undergo multiple binding steps (not modeled) until release. Thus, the RP releases vesicles slow but in a sustained manner. The RRP, on the other hand, is responsible for a fast and transient release of vesicles into the synaptic cleft. The vesicles in the RRP are tethered at the ribbon close to the actual fusion site and are already primed for release. Release from the RP and RRP is realized by a Poisson process and is mainly determined by the the intracellular calcium concentration $[\text{Ca}^{++}]_i$ and the release constants α_{RP} and α_{RRP}. Finally, both release pools release their vesicles into the exocytosis pool E.

determined in mouse, rat and goldfish; Oltedal & Hartveit (2010); Singer & Diamond (2006); Sterling & Matthews (2005); Wan *et al.* (2008); Zhou *et al.* (2006)) and the cytosplasmatic pool had a size of 360 vesicles. This factor was derived from the fact that in goldfish this pool has a size of 1000 vesicles per tethered vesicle but is suggested to be more than 100 fold smaller in mouse bipolar cells (Logiudice *et al.* (2009); von Gersdorff *et al.* (1996); Wan *et al.* (2010), reviewed in Wan & Heidelberger (2011))

In order to keep the model simple and because only short time periods were investigated no mechanism for endocytosis - re-uptake of released vesicles from the exocytosis pool into the cytoplasmatic pool - was incorporated. Furthermore, binding and unbinding of calcium ions as suggested by other models (Duncan *et al.* (2010); Heidelberger *et al.* (1994); Heinemann *et al.* (1994)) was neglected.

2.8 GC model

The standard GC model neuron is equipped with four different ion channel types and is mainly based on a model by Rattay and Wenger (2010) which, again, based on Hu *et al.* (2009b). Two sodium currents, namely a high threshold $Na_v1.2$ ($i_{Na_v1.2}$) and a low threshold $Na_v1.6$ ($i_{Na_v1.2}$) current, a non-inactivating potassium current i_K and a leak current i_L are incorporated into the model. Van Wart and coworkers (2007) reported that the two presented sodium channels are strictly separated along the AIS of rodents. A smaller portion of approximately one third of the AIS is occupied by $Na_v1.2$ channels whereas the distal portion is equipped with $Na_v1.6$ channels. Therefore, sodium channels were asymmetrically distributed along the neuron. Dendrites, soma, axon hillock, the AIS and the unmyelinated axon were equipped with $Na_v1.2$ sodium channels whereas the $Na_v1.6$ channels were only present in the AIS region. Potassium channel density was set to one fourth of the total ($Na_v1.2+Na_v1.6$) sodium channel density throughout the whole neuron. Leak current density was set to $0.033mS/cm^2$ in all computations.

$$i_{ion} = i_{Na_v1.2} + i_{Na_v1.6} + i_K + i_L \; (+noise) \tag{2.34}$$

$$i_{Na_v1.2} = g_{Na_v1.2} * m^3 * h * (V - E_{Na_v1.2}) \tag{2.35}$$

$$i_{Na_v1.6} = g_{Na_v1.6} * m^3 * h * (V - E_{Na_v1.6}) \tag{2.36}$$

$$i_K = g_K * n * (V - E_K) \tag{2.37}$$

$$i_L = g_L * (V - E_L) \tag{2.38}$$

Alphas and betas of the active channels were modeled in the following form:

$$\alpha = \frac{A(V - V_{1/2})}{1 - exp(-(V - V_{1/2})/k)} \tag{2.39}$$

$$\beta = \frac{-A(V - V_{1/2})}{1 - exp((V - V_{1/2})/k)} \tag{2.40}$$

Sodium inactivation was modeled with independent functions for h_∞ and τ_h. τ_h was described as τ_m but h_∞ was given by

$$h_\infty = \frac{1}{1 + exp((V - V_{1/2})/k)} \tag{2.41}$$

Current	Variable	Function	A	$V_{1/2}$	k
$I_{Na_v1.2}$	m	α	0.182	-28	7
		β	0.124	-28	7
	h	α	0.024	-35	5
		β	0.0091	-60	5
		∞	0.182	-57	6.2
$I_{Na_v1.6}$	m	α	0.182	-41	6
		β	0.124	-41	6
	h	α	0.024	-41	5
		β	0.0091	-73	5
		∞	0.182	-70	6.2
I_K	n	α	0.02	25	9
		β	0.002	25	9

Table 2.1: **Parameters for the equations describing Na and K currents -** More information on the equations can be found in Mainen *et al.* (1995).

All parameters are shown in table 2.1. For more information on modeling alphas and betas see Mainen *et al.* (1995). In order to simulate results at 37° Celsius alphas and betas have to be multiplied by a temperature coefficient of 3.209 (Q_{10}=2.3, Rattay & Wenger (2010)).

Random fluctuations (noise)

In order to compute more realistic responses of GCs a noise term was added in some simulations (equation 2.42). This term was presented previously (Rattay *et al.* (2001)) and the noise was assumed to be directly proportional to the sodium channel density (gNa$_v$1.2 and gNa$_v$1.6) at each compartment. I_{noise} changed its value every 0.01ms and k_{noise} was varied between 0.001 and $0.05\mu A/\sqrt{mS}$.

$$I_{noise,n} = rand * k_{noise} * \sqrt{(g_{Na_v1.2,n} + g_{Na_v1.6,n}) * A_n} \tag{2.42}$$

where $rand$ is Gaussian (0,1).

2.9 Implementation

All simulations and results in this thesis were generally controlled and executed by MATLAB. However, in order to generate an efficient framework also **MEX** (**MATLAB EX**ecutable) files were employed. MEX files provide MATLAB users an interface to directly execute C, C++ or FORTRAN code. In the created C files also high performance libraries such as **LAPACK** (**L**inear **A**lgebra **PACK**age, Anderson *et al.* (1999)) were employed.

Furthermore, the finite element computations were conducted in COMSOL Multiphysics 4.4 (`https://www.comsol.com`). These results were saved and loaded by MATLAB during the simulations. The flow diagram in Fig. 2.12 depicts the workflow of all simulations.

In order to the compute desired results the user must specify all parameters necessary for the virtual experiment (Fig. 2.12 right). After this, the simulation comprises the Hines ordering procedure, calculation of external potentials (only in extracellular mode), geometric and electric parameters. This is followed by obtaining the numerical solution and plotting of the results.

A more detailed description of the whole framework can be found in appendix A.
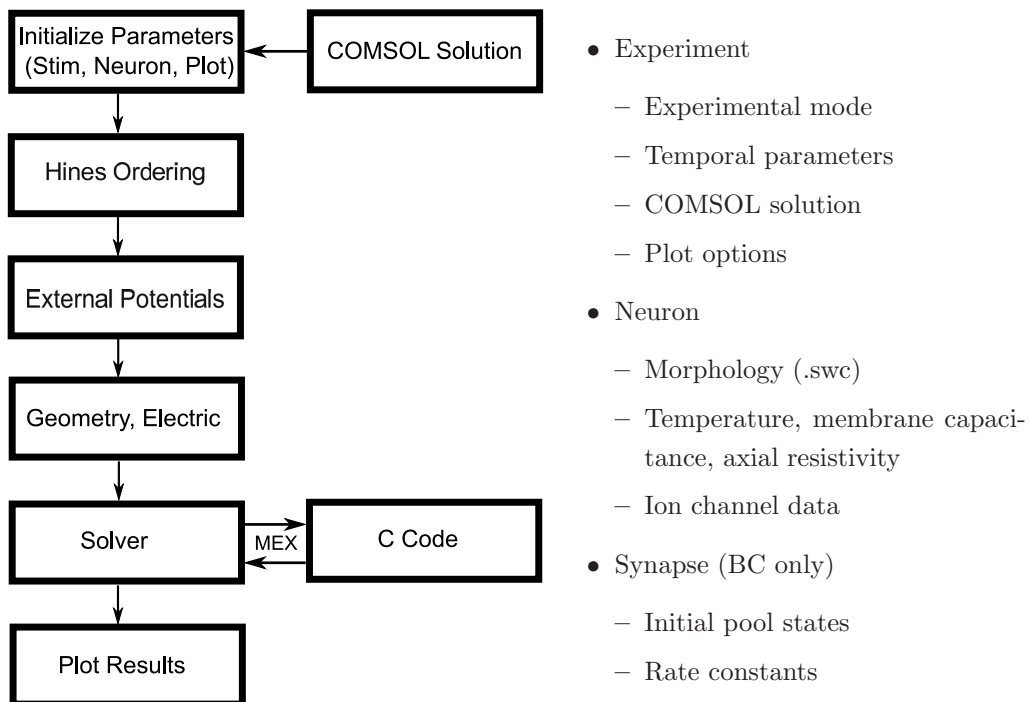
Figure 2.12: **Flow chart and input parameters of the framework -** (Left) A flow diagram depicts all steps necessary to compute the response of one or multiple model neurons. If external potentials are calculated numerically by COMSOL Multiphysics this solution has to be obtained and stored prior to the simulation. The solver uses MATLABs MEX interface to directly execute C code. (Right) Multiple parameters can be specified by the user. First, the experimental procedure is chosen, then all parameters (BC, GC) are specified. See appendix A for a more detailed description.

2.10   Testing

In this section the previously presented framework is compared to the most frequently used software employed to model artificial neurons - NEURON (Carnevale & Hines (2006)).

Accuracy

The two most crucial parameters for accurate computation of neuronal response are the used time-step, i.e. the temporal discretization, and the compartment length, i.e. the spatial discretization, of the model. Each compartment is represented by an electric circuit exactly at the center of the compartment. Taylor series expansion can be used to proof that this approximation leads to errors proportional to the square of the compartment length (Hines & Carnevale (1997)). Although in most models the compartment length is not uniform the approximate solution still is second order accurate which was also proofed by simulations (also Hines & Carnevale (1997)).

Nevertheless, with a decreasing compartment length and a corresponding larger number of compartments the computation time increases. If compartment length is smaller than a quarter of its space constant λ the numerical accuracy deviates by only approximately one percent compared to the solution of the continuous cable equation (Rattay (1999)).

$$\lambda = \sqrt{\frac{d}{4\rho_i g_m}} \tag{2.43}$$

ρ_i stands for the intracellular resistivity in Ωcm and g_m denotes the membrane conductivity in mS/cm^2. Maximum compartment length in all simulations was $\leqslant$10µm which is far below the critical length.

First order accuracy in time is achieved by the backward Euler solver presented previously. Nevertheless, it was chosen because of its stability for large time-steps and simple implementation. Fig. 2.13A shows the results of the presented framework compared to results computed in NEURON. The experimental setup is shown at the bottom, a straight fiber 10mm in length was current clamped at its centered soma. Recording electrodes were positioned at the soma itself as well as at both fiber ends. No significant differences can be determined in all membrane voltage traces - time
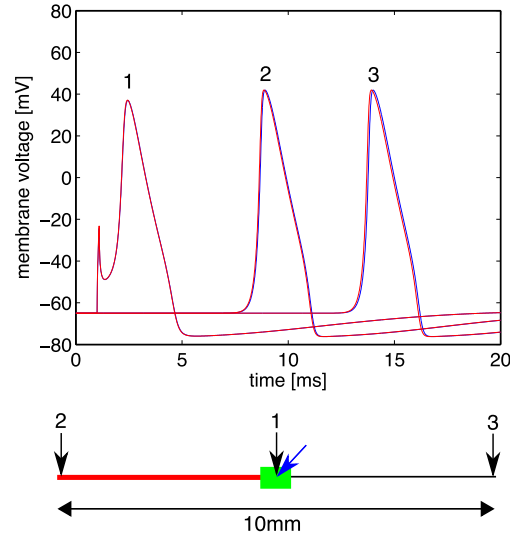
Figure 2.13: **Accuracy testing of the framework -** (Bottom) Current clamp experiment in a uniform fiber, the current was injected into the cylindrical soma in the center of the simulated fiber (blue arrow). Black arrows (1,2,3) denote recording electrodes at the soma and the two end-compartments. (Top) The time courses computed by NEURON and the presented framework do not show significant differences. The first arising action potential (1) belongs to the soma compartment (location of stimulus), (2) denotes the dendritic end-compartment which spikes prior than the axonal end (3) because of its larger diameter (6µm vs. 2µm). The whole fiber was equipped with the original HH model at 6.3°C. Compartment length was 10µm and the time-step was set to 0.00625ms.

course, spike amplitude and shape of all three action potentials match the results from NEURON. In all simulations in this thesis a time-step $\leqslant$0.01ms was used.

Performance

The framework was also tested in terms of computation time. Fig. 2.14 plots number of compartments against the computation time. Four different approaches were used to compute the solution of a matrix equation A*b=c (also see equations 2.27) and compared to NEURONs performance. All of these methods produce the exactly same result. All simulations were performed on a standard laptop computer (Apple MacBookPro7,1, 2.4GHz, 6GB RAM).

As shown in Fig. 2.14 MATLABs build-in function to compute the inverse of a matrix (inv(A)∗b or A\b) performs poorly in contrast to all other methods which show
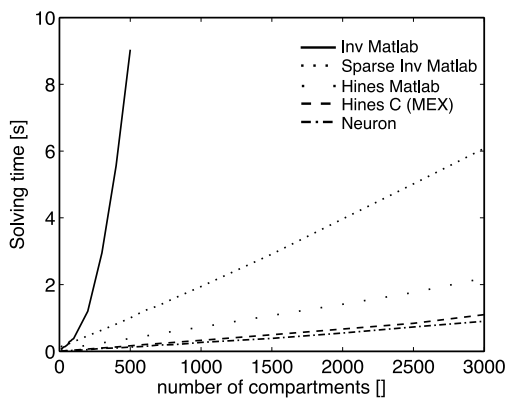
Figure 2.14: **Performance testing of the framework -** Solving equation 2.27 using different approaches results in computation times differing by several orders of magnitude. Computation time for MATLABs inv(A) increases approximately quadratically with more compartments whereas the sparse matrix function accomplishes linear runtime. Employment of the Hines method in MATLAB results in yet lower computation time, direct implementation in C using MEX files has a runtime comparable to NEURON.

quasi-linear performance. Because of only few non-zero elements compared to zero elements in the neighborhood matrix MATLABs sparse matrix function produces quite fast results. However, the approach described by Hines still minimizes computations time by almost a factor of three. Implementation in C code again increases the performance to a level which is comparable to NEURON.

Chapter 3

Part I: Bipolar cell stimulation

The purpose of this chapter was to analyze the response of BCs to electrical stimulation from the subretinal space. Time course of the membrane potentials as well as intracellular calcium concentration in terminal compartments were examined. Furthermore, synaptic release from ribbon synapses at BC terminals was computed.

Some results of this chapter have been originally published in Werginz *et al.* (2015). Additionally, results of this chapter are currently in review (Werginz P., Rattay F., *The impact of calcium current reversal on neurotransmitter release in the electrically stimulated retina*).

3.1   Cell-polarization during subretinal stimulation

BCs stimulated from the subretinal space are aligned perpendicular to the electrode and therefore are depolarized at their terminals and hyperpolarized at their dendrites when an anodic pulse is applied (Fig. 3.1B). Cathodic pulses, on the other hand, increase membrane potential at the dendritic end of the neuron and hyperpolarize the axonal and terminal compartments (Fig. 3.1C). This behavior was also predicted by a simple model presented by Eickenscheidt and Zeck (2012). The stimulus was applied via a point source electrode located 30µm distant to the end of the dendritic tree in the subretinal space (Fig. 3.1A).
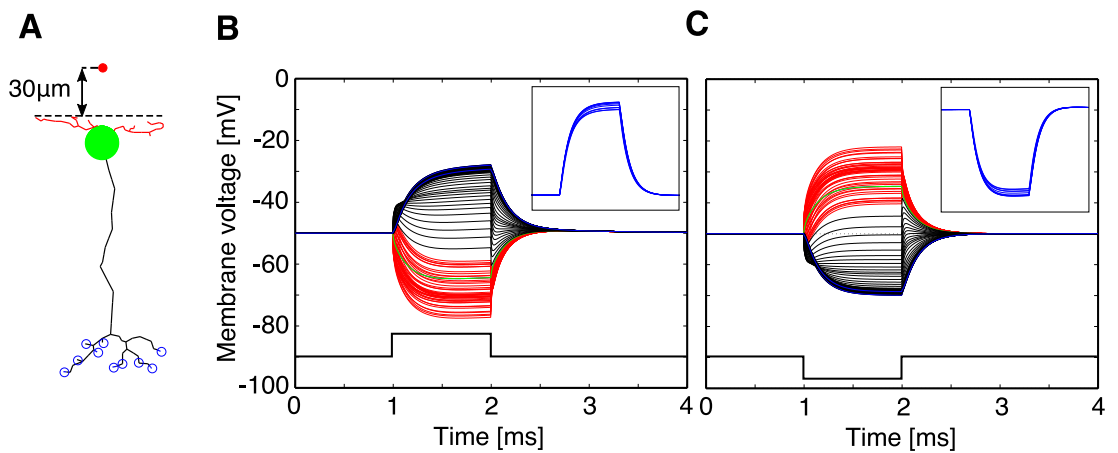
Figure 3.1: **BC stimulation with different pulse polarities -** (A) The point source electrode was located 30µm above the horizontal edge of the dendritic tree. Synaptic (terminal) compartments are indicated by blue circles. (B) Membrane voltage over time for all compartments of the ON BC. During anodic stimulation the dendritic parts of the neuron (red) are hyperpolarized whereas axonal (black) and terminal (blue, inset) compartments are depolarized. (C) Same computation for a cathodic pulse. Now the cells dendritic tree is depolarized and axon and terminals are hyperpolarized. The insets in (A) and (B) highlight small variation in membrane voltages of the 10 terminal compartments. The 3µA stimulus is shown at the bottom in (B) and (C). Colors are used for the compartments and their responses in (A), (B) and (C).

A

B
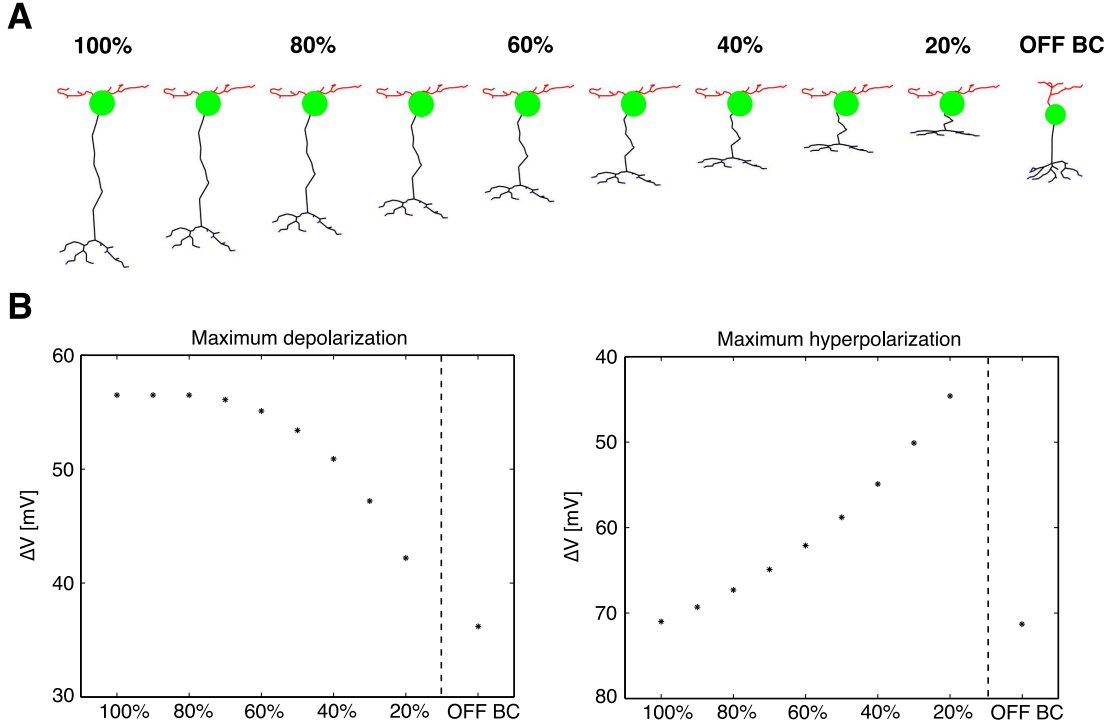
Figure 3.2: **Maximum de- and hyperpolarization of the ON BC with different axonal length -** If the axon of the ON BC is shortened, the maximum depolarization (A) and hyperpolarization (B) become weaker. If the ON BC has the same length as the OFF BC ($\sim$50%) the de- and hyperpolarization characteristics are totally different in both geometries. The electrode was located centered above the BC soma and the dendritic tree was 30µm distant (Fig. 3.1). Stimulus amplitude was 7.5µA.

3.2   Geometric influence

In the next step the ON BC axon was clinched in axial (z-dimension) direction in increments of 10% from 100% (original ON type geometry) to 20% of the original axial length (Fig. 3.2A). 50% of the original axon length results in a morphology which is comparable in length with the OFF BC geometry, however, it shows totally different de- and hyperpolarization characteristics (Fig. 3.2B). The shortened ON type geometry depolarizes more than the OFF type geometry ($\Delta V_{ON,50\%}$=55mV, ΔV_{OFF}=36mV) and hyperpolarizes less ($\Delta V_{ON,50\%}$=58 mV, ΔV_{OFF}=71mV). The stimulation configuration was the same as in Fig. 3.1, stimulus amplitude was set to 7.5µA.

3.3 Intracellular calcium concentration in synaptic terminals

Next, it was investigated how the intracellular calcium concentration in BC terminals changes during subretinal stimulation. Intracellular calcium is known to be the crucial parameter for exocytosis at ribbon synapses and therefore for the functional outcome during electrical stimulation.

Using the presented dynamics (Eq. 2.30, Fohlmeister *et al.* (1990)) in the terminals is determined by several parameters and two major physiologic mechanisms: a) influx and outflow of calcium ions through calcium channels embedded into the cell membrane and b) removal of calcium ions from the terminals via a passive sequestering process.

Influx of calcium into terminals

The opening of calcium channels followed by an influx or outflow of calcium ions is mainly determined by the cell's membrane potential and the time constant (τ_c) of the channel state variable c. Displaying steady state current densities at different clamp voltages results in an I-V curve which is depicted for the presented L-type calcium channel in Fig. 3.3A. At membrane voltages close to the resting potential of -50mV almost all calcium channels are closed. When the membrane is depolarized from its resting state calcium channels open and lead to an influx of calcium ions into the intracellular space. The minimum (i.e. the negative peak of the I-V curve) is located at approximately -15 to -20mV and denotes the membrane voltages at which most calcium channels are open in steady state conditions (i.e. the channel time constant can be neglected). If this peak potential is exceeded the inward-directed (negative) calcium current is first weakened and further even changed into an outward current. This implies that stronger depolarization does not necessarily lead to a higher calcium concentration. As soon as the calcium reversal potential is exceeded (vertical dashed line in Fig. 3.3A) the unwanted effect of outflowing calcium occurs.

Available activation kinetics taken from the literature generally exhibit rather small time constants of the activation variable which is in agreement with experimental studies in rat and cat showing rather fast activation and deactivation dynamics (Benison *et al.* (2001); Protti & Llano (1998)). One recent study, however, shows a voltage clamp experiment which generates slower activating calcium currents than all former studies

(Oltedal & Hartveit (2010)). Therefore, a similar voltage clamp experiment (-50mV to +50mV for 10ms) as presented in Fig. 9C in Oltedal & Hartveit (2010) was simulated in two configurations: a) with the channel time constant from the previously presented channel dynamics (Eq. 3) and b) with an increased time constant by a factor of 100. This factor was chosen to approximate the calcium current measured by Oltedal and Hartveit (Oltedal & Hartveit (2010)). The resulting ionic currents and intracellular calcium concentration are displayed in Fig. 3.3B and C, respectively. The configuration with the standard time constant leads to a calcium current (thin) that almost immediately follows the voltage signal (bottom) whereas a larger time constant leads to smoother activation and deactivation of the channel (thick). Similar to experimental results also currents during repolarization of the cell membrane have larger amplitudes than outward currents at high clamp voltages (Fig. 3.3B, compare to Fig. 9C in Oltedal & Hartveit (2010)). This is a consequence of larger time constants at higher membrane voltages (Fig. 3.4A). The channel time constant has its peak at -26mV and decreases to more de- and hyperpolarized membrane potentials. Because τ_c is lower at the resting potential than at the clamp potential of +50mV it takes the state variable c longer to fall back to its resting state from the clamp voltage than to rise from the resting state to the clamp voltage (Fig. 3.4B). This consequently leads to a larger current peak after pulse offset than during the pulse. Note that for both time constants the corresponding I-V curves are identical as they represent steady state currents.

The rate of activation and deactivation of calcium channels cause different effects on $[Ca^{++}]_i$ (Fig. 3.3C). Whereas the fast activation and deactivation with the standard configuration hardly influence the intracellular calcium level (thin) the prolonged onset after pulse offset at higher time constants results in a longer calcium influx and therefore in an elevated calcium concentration (thick). The prolonged high-level of intracellular calcium is likely to trigger vesicle release and therefore synaptic activity.
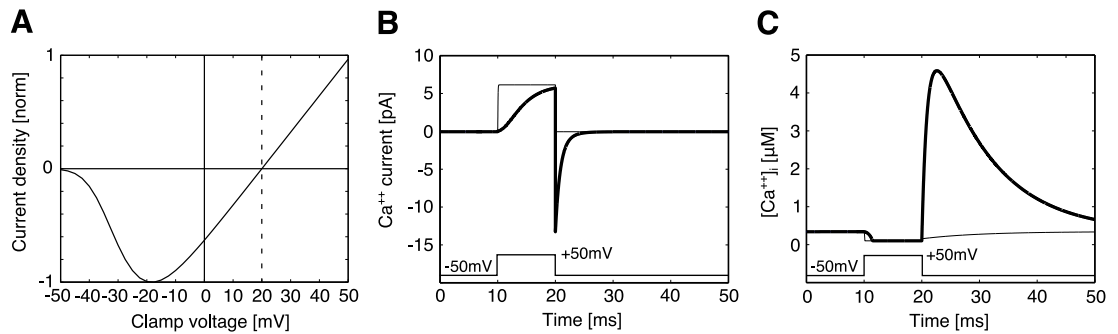
Figure 3.3: **Ca^{++} channel dynamics and considerations on channel time constant -** (A) The presented calcium channels exhibits peak inward currents at approximately -18mV. When a calcium reversal potential of 20mV (dashed vertical line) is exceeded the calcium channel is reversed resulting in outflow of calcium ions. Furthermore, hyperpolarization (V<-50mV) does not activate the calcium channel at all and therefore cannot elevate [Ca^{++}]$_i$ in terminal compartments. The simulated current-voltage (I-V) relationship resembles data from L-type channels in rat provided by two former experimental studies quite closely (Hu *et al.* (2009a); Protti & Llano (1998)). (B) The influence of the time constant c was examined during voltage clamp experiments. The evoked Ca^{++} current in the standard configuration follows the voltage clamp without any visible delay (thin). A larger time constant smoothens activation and deactivation resulting in a better fit to recently published observations (thick, Oltedal & Hartveit (2010)). (C) A prolonged opening of ion channels during the repolarization to the holding potentials changes intracellular calcium concentration significantly. A fast activation does not lead to an increased [Ca^{++}]$_i$ during the voltage clamp from -50 to +50mV (thin). The large time constant, on the other hand, makes the calcium influx during repolarization more sustained and therefore elevates [Ca^{++}]$_i$ (thick).
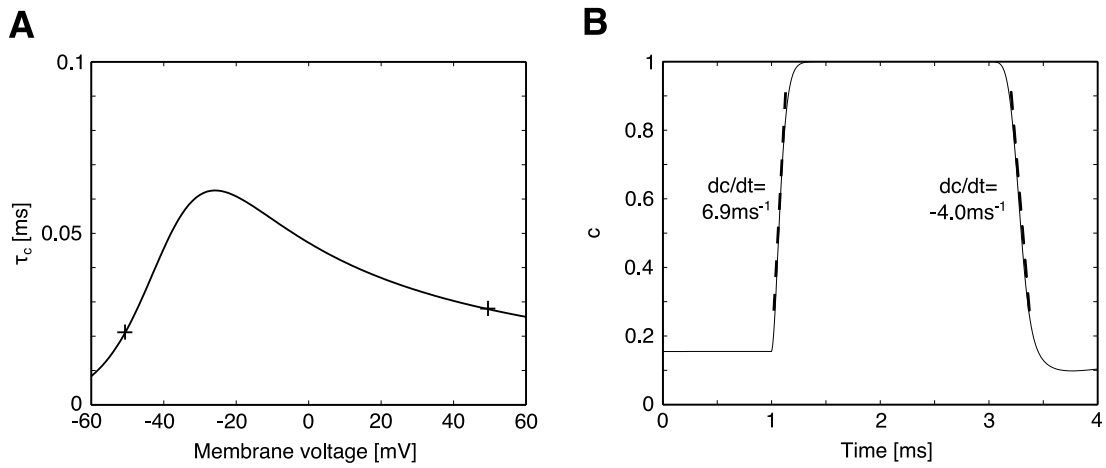
Figure 3.4: **Channel time constant during de- and repolarization -** (A) τ_c is dependent on the current membrane potential and has its peak at -26mV. At resting potential (-50mV, left +) the time constant is smaller than at the clamp voltage of +50mV (right +). This leads to de- and repolarization at different velocities. (B) Time course of c during the clamp experiment. The instantaneous depolarization leads to an increase of c with a half-activation slope of 6.9ms^{-1}. After the pulse is switched off the repolarization takes longer because τ_c is larger at high membrane voltages than at resting potential. The slope during the fall of c is approximately -4ms^{-1}.

3. PART I: BIPOLAR CELL STIMULATION

Effect of calcium reversal potential

The following example of subretinal BC stimulation demonstrates the effect of reversed calcium current for stronger stimulation in one of its synaptic terminals. A BC was stimulated as in Fig. 3.1A with 1ms pulses of 6 and 15µA, respectively. As expected, the 15µA pulse leads to stronger depolarization (thick) compared to the weak stimulus (thin) (Fig. 3.5A, upper curves). Whereas the weaker pulse causes only inward calcium current shown as negative current (Fig. 3.5A, lower curves, thin), the current resulting from the strong pulse changes polarity as soon as the reversal potential is reached (thick, shaded regions). During repolarization the membrane potential traverses from the right (depolarized) to the left (resting potential) of the I-V curve and therefore also crosses through the minimum of the I-V curve. This opens a maximum number of calcium channels and generates the minima of the two current traces. Larger channel time constants thereby shift these minima further to the right because of the slower deactivation during repolarization (not shown).

Consequently, the resulting intracellular calcium concentration is higher for the weak pulse (Fig. 3.5B). The 6µA pulse leads to an almost linear increase of calcium concentration during the pulse (thin). The strong pulse (thick) results in a dip in the calcium trace that arises from the weaker and further reversed calcium current (Fig. 3.5B). Therefore, stronger pulses do not necessarily lead to higher intracellular calcium concentrations. A summary of this characteristic is shown in Fig. 3.5C. A linear increase of depolarization (thick) is coupled with a non-linear relationship of intracellular calcium ion concentration (thin). After a peak at ∼6µA higher amplitudes weaken the efficacy of stimulation. Pulses with amplitudes higher than 15µA do not elevate intracellular calcium significantly and are therefore not suitable to activate synaptic exocytosis.
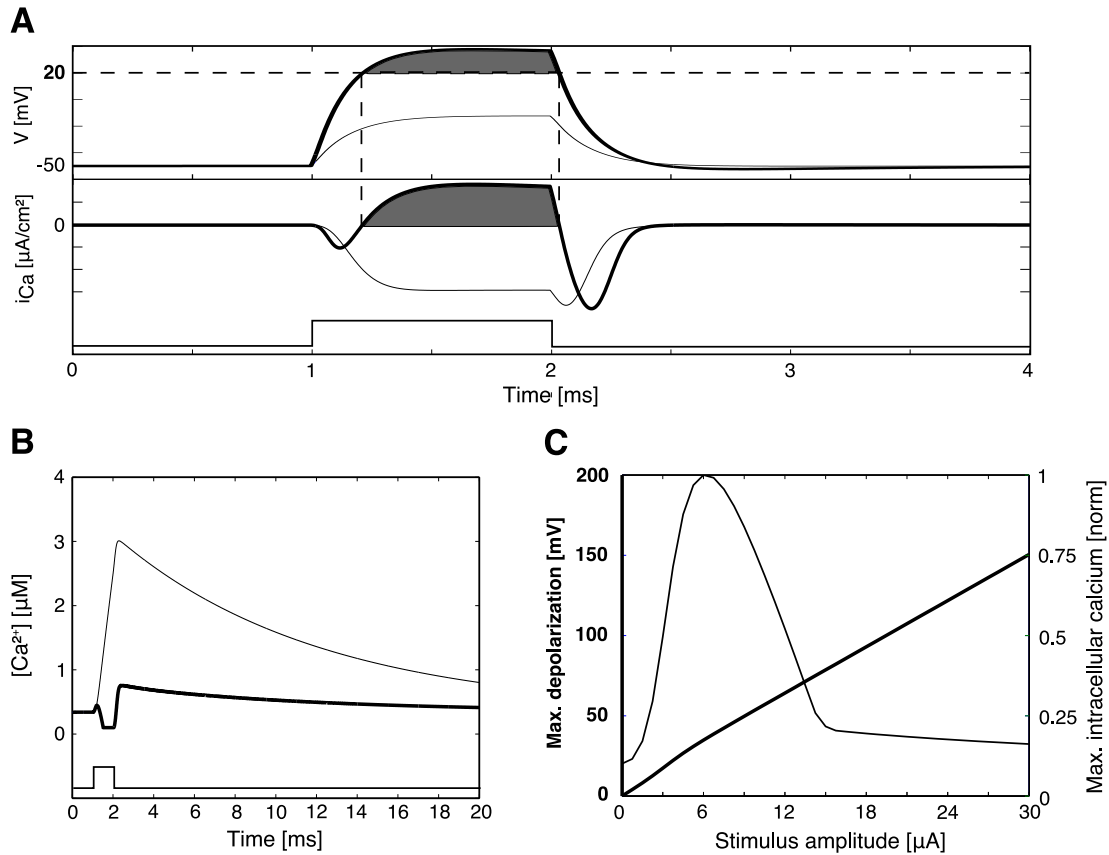
Figure 3.5: **Membrane depolarization is not a good predictor for intracellular calcium** - (A) Top: One synaptic terminal compartments of a BC is less depolarized during a 6µA pulse (thin) than during a 15µA pulse (thick) when stimulated accordingly to Fig. 3.1A. (A) Bottom: Whereas the 6µA stimulus leads to a constant calcium influx (thin) the stronger pulse (thick) reverses current flow during and also still shortly after the pulse (shaded regions). The minima of the two current traces slightly after pulse offset arise because of the delayed channel kinetics (see text). (B) Intracellular calcium concentration rises during the pulse and falls slowly back to its resting state after pulse offset (Note the different time scale than in (A)). The bend down to the residual level in the thick trace within the pulse results from the reversed current at high membrane voltages. (C) When the stimulus amplitude is increased consequently from 0 up to 30µA the maximum synaptic membrane depolarization (i.e. the average of the maximum depolarization of all 10 terminal compartments) increases linearly (thick). Intracellular calcium ion concentration (thin), however, peaks at 6µA and decreases at higher amplitudes.

3.4   Synaptic release

The impact of intracellular calcium concentration on discrete synaptic vesicle release
was simulated with a four pool model (Fig. 2.11). A cytoplasmatic Pool C fills the
rapidly releasable or fast pool RRP and the releasable or slow pool RP. These two pools
release their tethered vesicles into the synaptic cleft (exocytosis pool E). The presented
model does not incorporate any mechanism for endocytosis and calcium binding and
unbinding. Only short-term simulations were performed and therefore no need for refill
of the cytoplasmatic pool was needed.

Singer and Diamond (2006) conducted an experimental study on vesicle depletion
and synaptic depression in synapses between rod bipolar cells and postsynaptic AII
amacrine cells in *in-vitro* rat preparations. Presynaptic voltage clamps led to sustained
vesicle release with a large transient and a small sustained component of the postsy-
naptic EPSC (see also Singer & Diamond (2003); Snellman *et al.* (2009); Trexler *et al.*
(2005). Furthermore, voltage clamps for 100ms resulted in prolonged calcium currents
as expected from the non-inactivating L-type calcium current located in synaptic bou-
tons. With seven vesicles they estimated the size of the fast pool.

To confirm the physiologic behavior of the presented synapse model the voltage
clamp experiments by Singer and Diamond were mimicked (Fig. 3.6, Fig. 1C in Singer
& Diamond (2006)). The ON BC model neuron was clamped from its resting potential
of -50mV to -20mV for a period of 100ms (Fig. 3.6A). In this configuration no axial
currents between neighbored compartments are evoked and therefore all compartments
are in a virtual mono-compartment mode. During the clamp a constant calcium current
in the range of measured currents (tens of pA) was evoked (not shown). Intracellular
calcium concentration was elevated to a maximum of 30µM and dropped back to its
resting state after the clamp was removed (Fig. 3.6B). Also synaptic release fits ex-
perimental results properly (Fig. 3.6C). Total exocytosis is in the range of 100 vesicles
during the 100ms clamp (thick). The fast pool empties all vesicles within the first
20ms (middle). The slow pool (thin) continuously releases vesicles during higher levels
of Ca^{++} with a rate of approximately 0.5 vesicles/ms (dashed lines in Fig. 3.6C) as
determined by Singer and Diamond (2006). Thus, the presented simulation exhibits
the same major kinetic characteristics as measured results in *in-vitro* preparations.
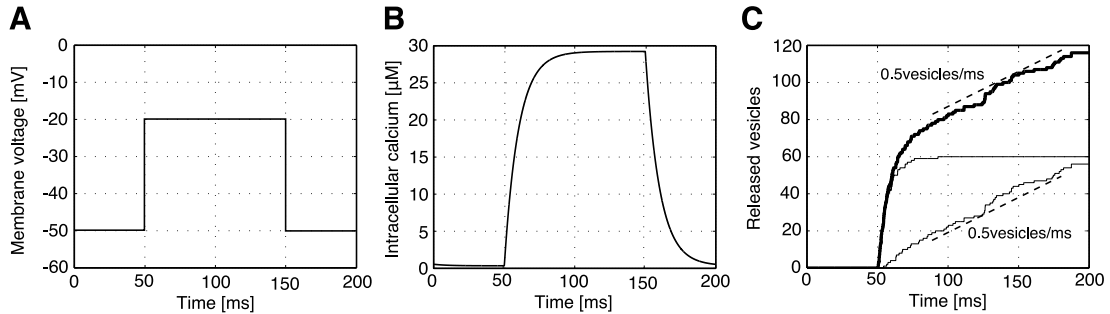
Figure 3.6: **Synaptic release from 10 ribbon synapses under voltage clamp condition -** A comparison to experimentally obtained data was conducted. 10 synaptic ribbons (as expected to connect a rod bipolar terminal and an AII amacrine cell, Singer *et al.* (2004)) each with a fast and slow pool size of 6 and 30 vesicles, respectively, were simulated. (A) Time course of the membrane voltage of one terminal (and all other) compartment(s). The ON BC was clamped from its resting potential (-50mV) to -20mV similar to the experimental procedure described by Singer and Diamond (2006). (B) Corresponding intracellular calcium concentration in synaptic terminals. (C) Synaptic release elicited by the voltage clamp. The thick trace depicts the total exocytosis from all 10 ribbon synapses (i.e. sum over each pool E of all ribbons). Thin traces denote the individual releases from the RP and RRP. The fast pool is emptied within the first 20ms of the clamp whereas the slow pool is able to release vesicles with a constant rate of approximately 0.5 vesicles/ms (dashed lines) similar as measured data from experiments.

3.5 Implications on subretinal stimulation

Release and stimulus amplitude

The impact of stimulus amplitude on synaptic release was simulated for extracellular point source stimulation according to Fig. 3.1A for 2ms pulses. Similar to intracellular calcium concentration (see Fig. 3.5) also synaptic release does not increase monotonically at higher amplitudes (Fig. 3.7). At each stimulus amplitude (0.75µA steps) 10 simulation runs were performed and the total release of 10 ribbons (=360 vesicles tethered in total), each in one terminal compartment, at the end was monitored (asterisks). Simulation time was set to 30ms to also monitor vesicle release after pulse offset due to sustained higher levels of $[Ca^{++}]_i$. The mean release of all 10 runs is depicted by the solid line. Below a stimulus strength of 1.5µA no release is triggered. Maximum release is evoked at an electrode current of approximately 6µA and release is switched off when amplitudes exceed 12µA.

In order to determine robustness of the computed results pulse width and config-
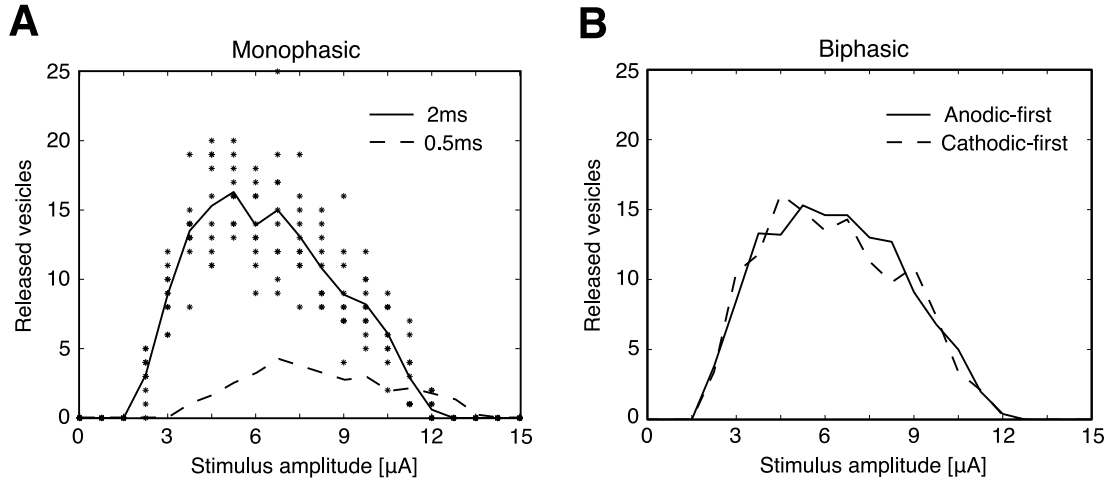
57

Figure 3.7: **Strong stimuli switch off synaptic release -** One BC terminal releases vesicles only within a range of stimulus amplitudes. (A) The release of 10 synaptic ribbons (6+30 vesicles docked each) of 10 repetitive runs at each amplitude (asterisks) and the mean release (solid line) are shown. Maximum release occurs at ∼6µA when also the peak of intracellular calcium concentration is reached (compare to Fig. 3.5). Pulse length 2ms. The same investigation was conducted with a pulse length of 0.5ms (dashed line). Similar release characteristics were found, however, total release is decreased. (B) Symmetric charge balanced pulses (2ms each phase, no gap between phases) did not affect synaptic release substantially. As a result, comparable release characteristics and total number of released vesicles were observed. All simulations were run for 30ms in order to include release after pulse offset.

uration was varied. First, shorter pulse durations in the range as applied in clinical applications (0.5-1ms, e.g. Stingl *et al.* (2013)) and *in-vitro* experiments (0.1ms, e.g. Jensen & Rizzo (2006)) were used. As shown in Fig. 3.7A a pulse duration of 0.5ms (dashed) leads to the same release characteristics (lower and upper limit for exocytosis), however, the total number of release is decreased strongly. Single pulses <0.5ms were not able to elicit synaptic release.

Charge balanced biphasic pulses (cathodic- and anodic-first) as used in clinical applications were also tested (Fig. 3.7B). No significant difference to monophasic stimulation was observed. The cathodic pulse in biphasic configuration did not influence calcium currents essentially because it only accelerated re- (and hyper)-polarization of the membrane without influencing intracellular $[Ca^{++}]_i$ distinctly. Consequently, synaptic release was not substantially affected.

Center-surround effect

An important implication of the relationship between synaptic release and stimulus amplitude is the artificial generation of an unexpected center-surround effect for stronger stimuli. Whereas during natural excitation a depolarization level close and above the reversal potential of the calcium channel will not be reached this might happen during electrical stimulation with subretinal implants.

In order to examine how release is influenced by cell location relative to a stimulating electrode 1681 ON BC positions were aligned on a 41x41-5µm grid in x-y plane (z-distance 30µm, Fig. 3.8). Two stimulus amplitudes were applied 10 times and the mean response (i.e. overall released vesicles) of all 1681 BCs was monitored. The first chosen amplitude was 6µA which caused the strongest possible release for the cell closest to the electrode. Increased BC distance from the electrode resulted in weaker synaptic responses and BCs far away (>60µm) from the electrode were not depolarized strong enough to initiate synaptic release (Fig. 3.8A).

Stronger pulses were shown to decrease synaptic activity because of a hyper--depolarization of the calcium channel. The outcome of this fact during stimulation of multiple BCs is a pronounced ring-shaped exocytosis pattern (center-off, surround-on), e.g. for 15µA (Fig. 3.8B). Thereby, BCs closest to the stimulation electrode are not responding at all (no synaptic release) but BCs in a mid-range between approximately 20 and 90µm release vesicles. Far distantly located BCs (>90µm) again do not respond because of the decreased influence of the applied electric field.

Figure 3.9 summarizes the center-surround mechanism for a wide range of amplitudes. The mean number of released vesicles from all 1681 cells is plotted against stimulus amplitude (3.9A). The total number of initially tethered vesicles is 1681x10x(30+6) = 605160. Higher amplitudes lead to more neurotransmitter release and therefore are likely to generate stronger network activity, however, at locations which are not close to the electrode center. Release maps for the range of applied amplitudes show the transition from an increasing spot of exocytosis to a ring-shaped release pattern (3.9B).
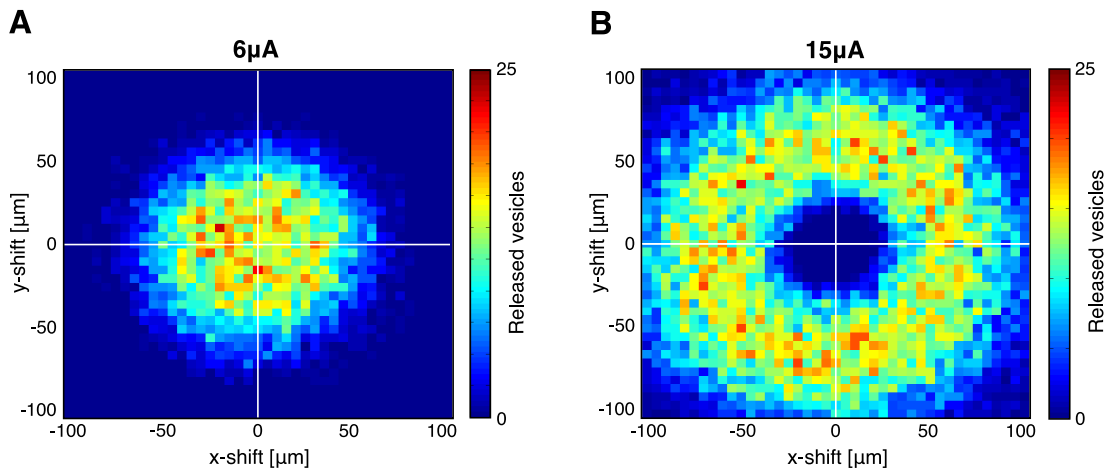
Figure 3.8: **Calcium channel dynamics generate a center-surround effect** - Activation and consequent synaptic release from 1681 ON BCs located in a x-y plane were computed. The modeled BCs were positioned on a 5µm grid from -100µm to 100µm in x- and y-direction. The electrode was located at 0/0. (A) An amplitude of 6µA leads to vesicle release in cells located close and directly below the electrode whereas BCs located far off the electrode do not increase their terminal Ca^{++} concentration and thus no synaptic release is initiated. (B) Increasing stimulus amplitude to 15µA results to a center-off surround-on mechanism. Cells closest to the electrode (distance approximately 0-25µm) are depolarized strongly and therefore the calcium in their synaptic terminals reversed calcium influx into an outflow of calcium ions. Depolarization level for cells located in a mid-range (25-90µm) afar the electrode is in the range which elevates intracellular calcium sufficiently in order to release vesicles. Cells positioned more than ∼90µm away are not depolarized sufficiently and are therefore not able to initiate substantial vesicle release. Pulse duration was 2ms, geometry as in Fig. 3.1A.
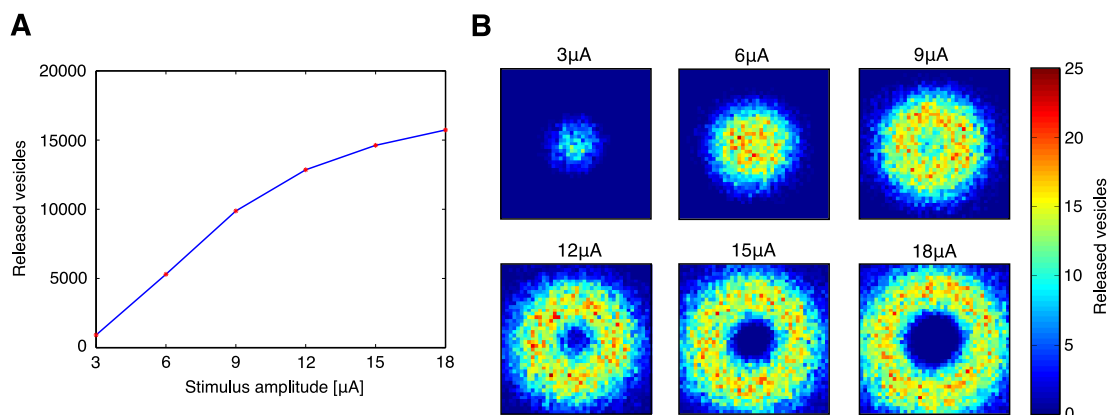
Figure 3.9: **Released vesicles and center-surround effect -** (A) Discrete release events from all 1681 cells are plotted against stimulus amplitude. From 605160 total tethered vesicles less than 3% are released during the strongest 2ms pulse (18µA). Higher amplitudes lead to more release, however, at locations not directly below the electrode. (B) Release maps resulting from increased stimulus amplitudes. Whereas at low amplitudes cells close to the electrode show strong release higher amplitudes shut down release from these cells. The transition between the two states occurs continuously in the range of 9-12µA. Color map and geometry as in Fig. 3.8.

Stimulation with disc electrodes

In order to get closer insights on synaptic release caused by retinal implants point source simulations were repeated with subretinal disc electrodes according to Fig. 3.10A. In the first example stimulus amplitude was set to be most effective for BCs just below the electrode, i.e. to evoke maximum release. Three electrode diameters (50, 100 and 200µm) were investigated. Synaptic release for BCs located along one axis through the middle of the electrode was computed (Fig. 3.10B). Stimulation with disc electrodes leads to release which peaks above the surface of the electrode and gradually drops towards zero outside of the edge of the electrode.

In a second series of simulations, the impact of stimulus strength on the center-surround effect was examined for the 50µm diameter electrode. Qualitatively, the current reversal mechanism led to the same release patterns as demonstrated before by a point source. The almost constant release for BCs located inside the edge of the electrode, however, led to more abrupt (i.e. evoked by only small changes in stimulus amplitude) change between vesicle release in BCs close to the electrode and the ring-shaped exocytosis pattern (Fig. 3.10C). The center-off region typically had approximately the size of the electrode at amplitudes little above the reversal potential.
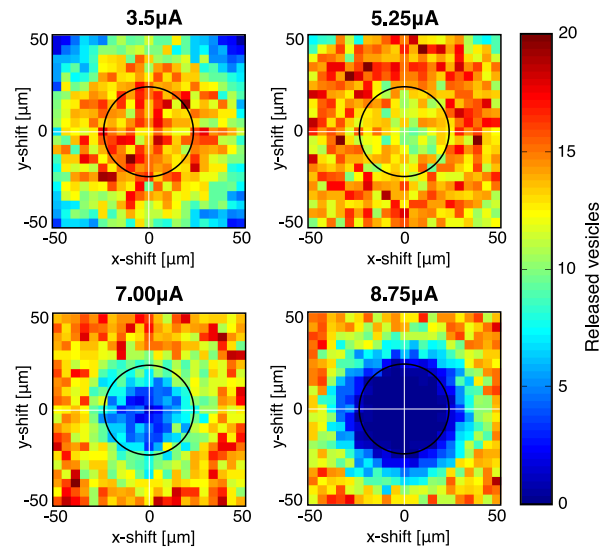
A
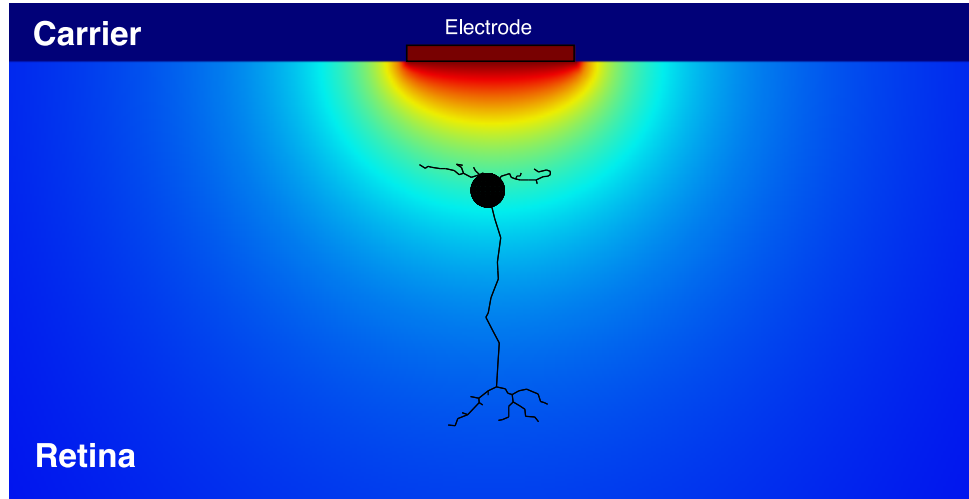
B
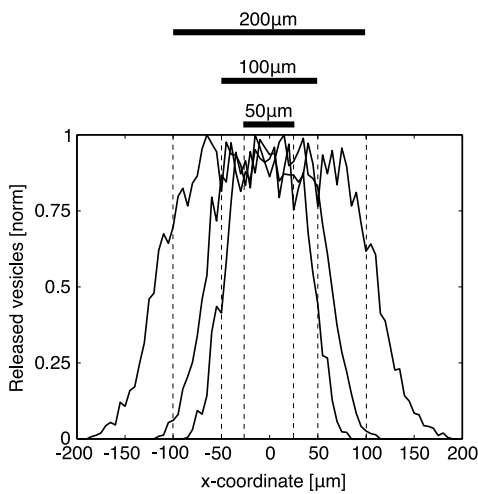
C

Figure 3.10: **Stimulation with disc electrodes and center-surround effect -** (A) A single BC depicted close to a 50µm diameter disc electrode. (B) Release from BCs aligned along the main axis of the electrodes (50, 100 and 200µm in diameter) was monitored. Regions below the electrode surface show constant release which gradually decreases outside of the electrode edges as long as calcium current reversal is avoided. (C) Stimulation at sub- and supra-reversal amplitudes for a 50µm electrode (black circle). Like for point source electrodes a center-surround pattern arises at strong stimuli. Because of the release pattern depicted in (B), however, the size of the center-off region has approximately the size of the electrode (bottom right panel).

3.6 Discussion

The key finding of this work is that a computational model supports the hypothesis that subretinal stimulation strongly influences calcium channel dynamics and synaptic release in BC terminals. In consequence, surprising and unwanted effects might occur during stimulation with subretinal implants. Whereas too low stimulus amplitudes will not sufficiently activate calcium channels in BC terminals also high amplitudes prevent synaptic signal transmission due to reversed calcium currents.

Upper threshold for spikes and synaptic release

Current-voltage relationship as well as evoked current traces during voltage clamp experiments allows deriving mathematical descriptions of many types of ion channels. Some of the resulting implications which can be made from these kinetics, however, were not elucidated thoroughly in the past. The consequences of current reversal is investigated only in a few studies and resulted in divergent conclusions (Boinagrov *et al.* (2010, 2012); Buitenweg *et al.* (2002)). Therefore, it is not clear yet if current reversal phenomena can be evoked during extracellular stimulation (i) at all, (ii) in exceptional cases, or (iii) regularly and estimated by simple rules.

Whereas the previously mentioned studies used neurons which transduce information via all-or-nothing spikes to our knowledge no former work was conducted about implications of reversed currents on synaptic transmission. Stimulating strategies used in current neural prostheses which aim to trigger synaptic release in a controlled way, do not consider the current reversal phenomenon. As suggested by the presented results, however, synaptic release at BC terminals is strongly influenced by reversed calcium currents during stimulation with high amplitudes. Thus, the upper threshold for calcium current inflow and the presented center-surround mechanism is expected to have implications on the generated phosphenes in patients when stimulated subretinally.

Cathodic vs. anodic stimulation

The presented biophysical model (Fig. 3.1) explains why anodic polarity is capable of eliciting synaptic release in BCs when stimulated from the subretinal space: Synaptic release is triggered by an increase of intracellular calcium which can only be initiated if terminal compartments are depolarized (Figs. 3.3 & 3.5). Cathodic stimulation,

however, hyperpolarizes terminal compartments and thus does not lead to an influx of calcium ions. In two *in-vitro* and *in-vivo* studies the better efficacy of anodic stimulation to activate the retinal network was also shown (Boinagrov *et al.* (2014); Lorach *et al.* (2015a)). The presented model only consists of BCs without getting inputs from ACs which modulate synaptic BC output (Euler *et al.* (2014)). From a modelers point of view indirect GC excitation without photoreceptor input during cathodic stimulation is (as shown in experimental studies, e.g. Jensen & Rizzo (2009)) possible through at least two mechanisms: i) activation of AII amacrine cells connecting to cone ON BCs via gap junctions (excitation via rod pathway, ON GCs activated only) and ii) activation of BCs due to more parallel oriented BC terminal regions.

Pulse parameters

This study uses a default monophasic pulse with a duration of 2ms to present first insights into current reversal during electrical stimulation. Shorter pulses were tested too and resulted in decreased synaptic release. This resulted from a shorter period of inflowing calcium ions into the intracellular space and therefore to a lower level of $[Ca^{++}]_i$. Current subretinal implants use pulse lengths in the range of 1ms (Stingl *et al.* (2013)) which is on the long side of pulse durations in electrical neurostimulators. Another recent clinical study with an epiretinal implant also reports that longer pulses elicit the network stronger (Weitz *et al.* (2015)). In sum, the presented model supports these findings that longer pulses are generally more suitable to generate synaptic (network) activity.

Calcium channel dynamics and vesicle release

Aside from the current reversal phenomenon also other dynamics of the L-type calcium channel determine the synaptic release during electrical stimulation. Whereas the current reversal is fully determined by the calcium reversal potential the temporal behavior (i.e. how fast a gating variable responds to changes in membrane voltage) of activation and deactivation of the channel are specified by the channel's time constant τ_c.

The presented results suggest that the time constant can be responsible for synaptic release despite stimulation in the current reversal regime (supra-reversal stimulation). If the current reversal occurs calcium flows out of the intracellular space and drops quickly

to the residual level during the pulse. This happens for a wide range of time constants and does not lead to vesicular release. When the pulse is switched off, however, the time constant starts to play an important role. For small time constants the state variable c almost immediately drops back to its state at the holding potential (fast deactivation). This does not activate a calcium current sufficient to elevate $[\mathrm{Ca}^{++}]_i$ necessary for synaptic release. Larger time constants, on the other hand, lead to a slow progression of the state variable towards its resting state (slow deactivation) and therefore activate a sustained inward calcium current. This current increases $[\mathrm{Ca}^{++}]_i$ and thus might be able to trigger transmitter release. In an experimental validation (see *Procedures to experimentally determine current reversal*) this fact can be observed by a larger delay until release starts because whereas during sub-reversal stimulation release will begin during the pulse supra-reversal stimulation will initiate vesicle release after pulse offset (also see Fig. 2C in Singer *et al.* (2004)). This mechanism is further supported by stronger inward currents at stimulus offset than outward currents during the pulse. Again, the channel time constant influences this behavior because τ_c is larger at membrane voltages exceeding the calcium reversal potential (>20mV) than at the resting potential of BCs (-50mV, Fig. 3.4A).

Artificially evoked synaptic release and fading percepts

A clinical study reported that 8 out of 9 tested subjects experienced fading percepts during a stimulation of 10 seconds with an epiretinal prosthesis (Fornos *et al.* (2012)). At stimulus onset all patients reported well-localized and bright sensations which faded away in a very short period of time. The authors concluded an activation of the retinal network to be the reason for this fading phenomenon. The presented calcium channel dynamics might be another explanation for fading sensations during prolonged electrical stimulation. If long and or repetitive strong pulses keep terminal membrane voltage at a constant high level close to the inward current peak of the calcium channel (-20 to -10mV) the intracellular calcium concentration reaches a constant high level. This constant high level of $[\mathrm{Ca}^{++}]_i$ further leads to a fast but also sustained release of vesicles which can almost deplete both the RP and RRP within a short period of time, i.e. in the range of seconds. Vesicle depletion caused by too strong stimuli therefore can be one reason for fading percepts during electrical stimulation. This assumption is further supported by the fact that rectangular pulses lead to an unnatural depolarization

process. By applying strong stimuli the membrane voltage almost immediately (<5ms, Fig. 3.3) follows the time course of the pulse and therefore gets clamped from its resting potential to a certain voltage until the pulse is switched off. This artificial clamp condition has two important implications: (i) the intracellular calcium concentration will rise rapidly and (ii) therefore release (and consequently the ganglion cell EPSC) will have a large transient component. In natural vision, on the other hand, the response of the membrane voltage to light inputs can take up to 100ms (Euler & Masland (2000)) and therefore also shows quite different release kinetics (Snellman *et al.* (2009)). In sum, artificially evoked responses of the retinal network by electrically driven implants do not reflect natural excitation and therefore limitations in clinical outcome such as temporal fading of percepts might occur. Thus, the ion channel time constant, pulse shape, stimulus amplitude and frequency seem to be crucial parameters which should be systematically investigated in the future.

BC morphology and current reversal

This study investigated the response of a rat type 9 ON BC (Euler & Wässle (1995)) to electrical stimulation from the subretinal space. BCs, however, can be classified by their morphology into multiple (∼10) subtypes in rat (Euler & Wässle (1995)) and mouse (Ghosh *et al.* (2004)). Whereas ON BCs stratify in layers closer to the inner retinal border OFF BCs have shorter axonal processes and therefore their stratification layers are closer to the outer retinal border. It was shown that the stratification level (i.e. the length of BCs), aside from other factors such as soma size and location and geometry of synaptic terminals, is the most dominant factor for cell depolarization (Werginz *et al.* (2015)). ON BCs are stronger depolarized during anodal stimulation from the subretinal space than OFF BCs. Since depolarization of the membrane potential determines the calcium current reversal, stimulation for ON and OFF BCs significantly different patterns of synaptic release are expected. Because of their different depolarization characteristics the calcium current reversal will occur at lower stimulating amplitudes in ON than in OFF BCs.

Moreover, since the exact distance between the implant and its target neurons (BCs) is not the same for each electrode small differences in this distance can lead to large differences in depolarization of BCs. Furthermore, electric properties of the

surrounding tissue are highly anisotropic and therefore a certain amplitude pulse might have different impact on different BCs.

Amacrine cell activation

Amacrine cells (ACs) are a diverse group (>25 subtypes) of laterally working second-neurons in the retina (Masland (2012b)). ACs connect to ganglion cells but also make inhibitory synapses on BC axons. Therefore, the responses of ACs during electrical stimulation of the retina also seem to be of high importance on clinical outcome. In a simplified picture, ACs are aligned in parallel to the stimulating element and therefore their activation can be estimated by the activating function (i.e. the curvature of the electric potentials along the neuron (Rattay (1986)) and the electric field at the terminals (Rattay (1999))). Their synaptic activity during electrical stimulation is therefore also strongly influenced by the geometric alignment of synaptic terminals. Current depictions of ACs in the literature, however, mostly only show the general layout of ACs without examining terminal regions closely. Therefore, without more detailed knowledge of AC morphology, especially the alignment of the synaptic terminals, it is not possible to make general assertions on the activation of ACs during subretinal stimulation. Due to their larger distance ($\sim$50-100µm, depending on stratification level in the inner plexiform layer and electrode placement) from the stimulating electrode, however, it is likely that ACs will not be activated strongly at amplitudes sufficient to activate synaptic release in BCs. Thus, the influence of ACs on artificially generated visual percepts may be rather small during subretinal stimulation.

Direct ganglion cell activation and current reversal

An experimental study investigated the suitability of direct activation of retinal ganglion cells (RGCs) from the subretinal space (Tsai *et al.* (2009)). In their results Tsai and coworkers, however, stated that direct stimulation of RGCs was accompanied with unpredictable long-latency activity of the network. In order to compare our finding of the center-surround mechanism with these results spiking threshold for subretinal anodic stimulation of a model RGC was determined (50µm disc electrode, 2ms pulse, data not shown). Activation thresholds varied between 3 and up to 11µA (depending on electrode location) which is in a similar range as amplitudes that can evoke the

current reversal phenomenon (see Fig. 3.10). Therefore, it is likely that direct stimulation of RGCs from the subretinal space will correlate with supra-reversal stimulation of BCs and thus, because of the surround-on behavior at high amplitudes, might generate visual sensations of low spatial and temporal accuracy.

Procedures to experimentally determine current reversal

Future experimental studies should evaluate the predicted calcium current reversal phenomena during subretinal stimulation. Oltedal and Hartveit previously showed the effect of current reversal in one of their figures, however, did not further investigate the underlying mechanisms (Oltedal & Hartveit (2010)). Therefore, systematic investigations should clarify unknowns and further explore effects on synaptic release. By placing either a single stimulating electrode or a microelectrode-array in the space between retinal pigment epithelium and the outer plexiform layer and consequent stimulation of BCs the theoretically described mechanism can be elucidated. In order to determine the occurrence and effect of calcium reversal several experimental methods can be used: i) measuring of calcium currents in synaptic terminals of BCs close to the stimulating element (e.g. Oltedal & Hartveit (2010)); ii) observation of change in terminal intracellular calcium concentration with fluorescence calcium imaging (e.g. Protti & Llano (1998)); iii) quantification of terminal $[Ca^{++}]_i$ with two-photon Ca^{++} imaging (e.g. Baden *et al.* (2013a)); and iv) determination of synaptic release by measuring changes in cell membrane capacitance (e.g. Oltedal & Hartveit (2010)).

Implications on other chemical synapses and neuroprosthetic devices

The calcium current reversal phenomenon is not limited to ribbon synapses in the retina but according to this study it is expected to occur in general at synapses in the close vicinity of microelectrodes when they are used to stimulate neural tissue extracellularly. Recently it was reported that intracortical microstimulation activates layer 5 pyramidal neurons mainly transsynaptically (Hussin *et al.* (2015)). This observation seems to be in conflict with the generally accepted assumption that the axon and especially the axon initial segment and nodes of Ranvier are the most excitable parts of a neuron (Fried *et al.* (2009); Nowak & Bullier (1998); Rattay & Wenger (2010); Rattay *et al.* (2012); Werginz *et al.* (2014)). However, finding the most excitable region of a neuron is based on experiments where a microelectrode scans threshold current in constant distance,

e.g. 50µm, along the surface of a neuron. The threshold current for a 100µs pulse from a microelectrode 50µm above the axon initial segment of a pyramidal cell is about 17µA (Rattay *et al.* (2012)). During subthreshold stimulation of this target cell with a 15µA pulse the same microelectrode can excite many tiny axons and dendrites which are densely packed around the tip of the electrode. Whereas a small number of single pulses may result in a lack of temporal summation of excitatory and inhibitory postsynaptic potentials, repetitive stimulation trains has been shown to promote transsynaptic neural activation (Asanuma & Rosén (1973); Tolias *et al.* (2005)). The reduced excitation by calcium current reversal is therefore of high interest for such pulse trains where the synaptic excitation is expected in animal experiments or via neuroprostheses in medical applications.

Additional aspects / limitations

Synapse model

In order to keep the presented synapse model simple and because only short time periods were investigated no mechanism for endocytosis - re-uptake of released vesicles into the cytoplasmatic pool - was incorporated. Furthermore, binding and unbinding of calcium ions as suggested by other models (Duncan *et al.* (2010); Heidelberger *et al.* (1994); Heinemann *et al.* (1994)) was neglected. The refill process of the fast pool is generally faster than of the slow pool, however, works in the range of several seconds for both pools (time constants between 4s (RRP) and 8s (RP) in rat (Singer & Diamond (2006)) and goldfish (Heidelberger *et al.* (2002); Hull *et al.* (2006); Mennerick & Matthews (1996))) and therefore has only small influence on the presented results. In different species an accelerated refill process was examined during prolonged calcium influx which was not included into the presented model (e.g. Sakaba *et al.* (1997); Singer & Diamond (2006); Wan *et al.* (2008)).

Synaptic calcium concentration

The amount of free calcium in the intracellular space of synaptic terminals governs exocytosis in chemical synapses (Heidelberger (2001); Neher & Sakaba (2008)). Therefore, in the presented model $[Ca^{++}]_i$ is the most crucial parameter when simulating synaptic

release. Several complex models were proposed in the past in order to estimate intracellular calcium concentrations in different cell types (DiFrancesco & Noble (1985); Forti *et al.* (1989); Usui *et al.* (1996)). These models also incorporate detailed descriptions of multiple subsections within a compartment, low- and high-affinity buffers, Na-Ca exchangers and the Ca^{++} ATPase in order to describe calcium homeostasis. However, in order to reduce complexity and parameter space the simple approach proposed by Fohlmeister and coworkers (Fohlmeister *et al.* (1990)) was used in this work. Additionally, a former study (Benav (2012)) stated that the complex model by Usui and the simple model by Fohlmeister result in similar calcium concentrations and time-courses.

Aside from the influx of calcium into the cell the other important process determining $[Ca^{++}]_i$ is the simple passive extrusion mechanism which is governed by only one time constant τ_{Ca} and the calcium residual level. For a prolonged release of neurotransmitter from the ribbon synapse a sustained calcium level in the close proximity of the vesicles has to be maintained. In the case of pulses that short as applied in retinal implants (e.g. 1ms) $[Ca^{++}]_i$ will be elevated during the pulse and will fall back to its resting level after pulse offset. Therefore, the τ_{Ca} for removing calcium above the residual level from the intracellular space has strong implications on synaptic transmitter release during repetitive stimulation.

Action potentials in BCs

Recent studies changed the view on BCs and their signal transmission via graded potentials. In multiple animal models also transient membrane fluctuations resembling action potentials were found (e.g. Cui & Pan (2008); Dreosti *et al.* (2011); Walston *et al.* (2015)). These spikes are generated by either calcium or sodium channels and differ strongly in amplitude and shape. The arrival of a spike at the synaptic terminal is supposed to trigger an instantaneous release of all docked vesicles. This induced transient release is further followed by a short time of depression (Baden *et al.* (2013b)). These new findings are of high importance not only from an electrophysiological point of view but also will strongly influence the functional outcome during electrical stimulation using retinal implants.

T-type calcium channels in mammalian BC terminals

Also T-type calcium channels were found in the mammalian retina (Hu *et al.* (2009a); Pan (2000); Pan *et al.* (2001)). These channels are activated at lower membrane voltages and show transient and smaller sustained components (Pan (2000); Pan *et al.* (2001); Singer & Diamond (2003)). The role of T-type Ca^{++} channels in controlling and regulating synaptic release is still unclear and needs further investigation. Due to their stronger inactivation (in contrast to L-type channels) and subsequent more transient kinetics they are thought act as an initial booster for synaptic transmission (Singer & Diamond (2003)). Furthermore, as discussed previously (*Artificially evoked synaptic release and fading percepts*), the temporal kinetics of calcium influx also play an important role in synaptic release and therefore T-type channels might be responsible for the transmission of fine temporal details.

Chapter 4

Part II: Ganglion cell stimulation

The general idea of the presented results is to obtain more insights into the mechanisms that underlie spike generation in GCs. Special emphasis was put on the electrophysiological and geometric properties of the AIS region.

Some results of this chapter are in preparation for publication (Werginz P., Hadjinicolaou A., Fried S.I., Rattay F. and Hadjinicolaou A., Werginz P., Rattay F., Fried S.I.).

4.1   Electrophysiology

Electrophysiological cell-attached voltage-clamp recordings from explanted rabbit retina were used to generate high-resolution maps of GC sensitivity to electrical stimulation (e.g. Fried *et al.* (2009)). Low-frequency (10Hz) current pulse trains (Multi Channel Systems) were delivered by way of an 1MΩ stimulating electrode (Microprobes) placed 5µm above the inner limiting membrane. Activation threshold was defined as the stimulus amplitude at which 50% of all pulses elicited at least one spike. After recording, the GC was filled via whole-cell patch clamp with the Alexa 488 fluorescent dye (Invitrogen) to reveal the axon.

A threshold map recorded from a brisk-transient (BT) GC is shown in Fig. 4.1. A minimum-weight path of activation threshold (Fig. 4.1A, green dots) was found to be coextensive with the proximal axon (data not shown), and appears to correspond with a specialized portion of the inner segment that contains a high density of two types of voltage-gated sodium channel known as the sodium channel band (Boiko *et al.* (2003);
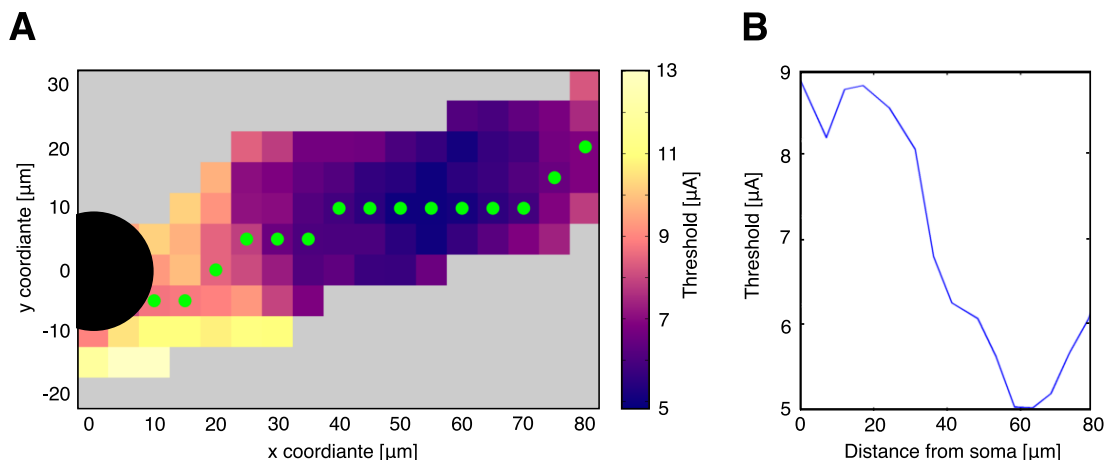
Figure 4.1: **Experimentally determined high-resolution threshold map for a GC -** (A) A similar procedure as described in Fried *et al.* (2009) was used to draw two-dimensional threshold maps. An OFF BT rabbit GC was examined for threshold during electrical stimulation with a micro-electrode. Lowest thresholds were measured in a region approximately 60µm distant to the soma (d=10µm, filled black circle). Green dots indicate the approximate location of the axon determined by a measured thresholds. (B) Threshold along the proximal axon. The stimulus was a biphasic cathodic-first pulse with a length of 0.1ms. Shown results were obtained by Alex Hadjinicolaou at Massachusetts General Hospital and will be submitted for publication shortly.

Van Wart *et al.* (2007), also Hadjinicolaou A., Werginz P., Rattay F., Fried S.I., in preparation). The location and length of the sodium channel band varies with GC type; for BT cells, the median length and distance-from-soma are ∼41µm and ∼27µm, respectively (Fried *et al.* (2009)).

4.2 Effects of two different sodium channel subtypes

In order to test the influence of the two sodium channel types on activation threshold a simple stick model containing either $Na_v1.2$ or $Na_v1.6$ channels was set up. Experimental results actually reported that $Na_v1.1$ and $Na_v1.6$ channels are distributed along the AIS (Van Wart *et al.* (2007)). Since no or only limited descriptions of $Na_v1.1$ dynamics are currently available in the literature the well described $Na_v1.2$ subtype was used in this study. $Na_v1.2$ and $Na_v1.1$ are supposed to be similar in their dynamics and therefore no significant qualitative differences are expected due to this interchange of ion channel subtypes.
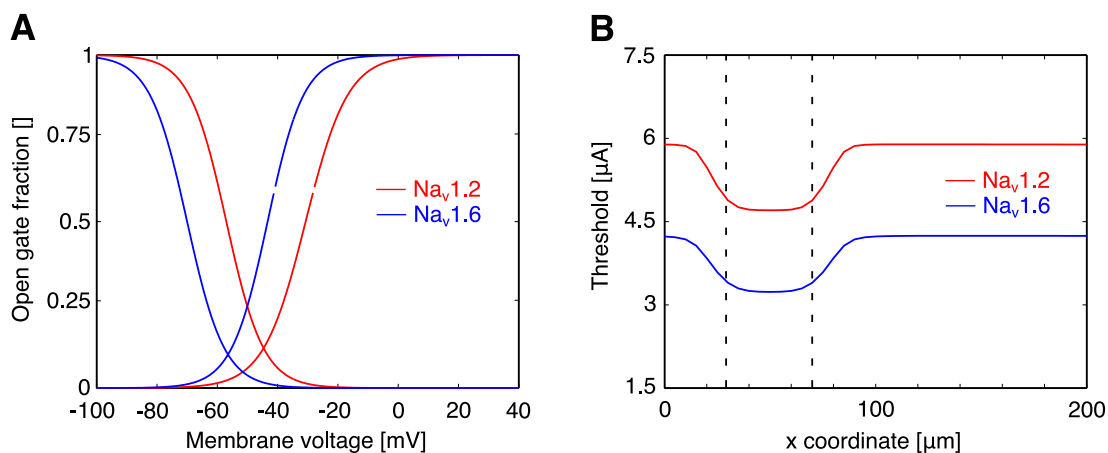
Figure 4.2: **High- and low-threshold sodium channels strongly influence activation thresholds -** (A) Activating and inactivating gates m and h for both sodium channels. The shown values are theoretically approached when the membrane voltage is fixed infinitely long. Modeled as sigmoid function the major difference between the curves is the parameter $V_{1/2}$ which is smaller (i.e. curves are shifted to the left) for $Na_v1.6$ than for $Na_v1.2$. Therefore, thresholds for a fiber equipped with $Na_v1.6$ channels are lower than for $Na_v1.2$ channels (B). Approximately 28% and 31% less current is needed when the stimulating electrode is located over the axon (x<10µm and x>90µm) and the location resulting in lowest threshold (50µm), respectively. The region of the AIS was 40µm long and is indicated by the two black dashed vertical lines in (B). Model properties: *Morphology:* stick (d=1µm); *Channels:* $Na_v1.2$ or $Na_v1.6$, K, L; *Temp:* 37°; *Pulse:* monophasic 0.1ms; *Potentials:* analytical (ρ_e=0.1S/m).

The different kinetics of the two sodium channels lead to activation and inactivation of the $Na_v1.6$ channel at lower membrane voltages than for its $Na_v1.2$ counterpart (Fig. 4.2A, compare to Hu et al (2009b, supplementary Fig. 3). The stick model was equipped with either $Na_v1.2$ or $Na_v1.6$ (gNa=50mS/cm^2) channels and potassium (gK=12.5mS/cm^2) channels as well as a leak current (gL=0.033mS/cm^2). A 40µm segment containing a five-fold higher sodium channel density was modeled in order to mimic the AIS region (vertical dashed lines in Fig. 4.2B). Resulting axonal thresholds, i.e. more than 20µm outside of the AIS region, are about 28% lower when $Na_v1.6$ was incorporated. In the fiber center, i.e. the electrode location that results in lowest thresholds, approximately 31% less current was needed to activate the neuron in the fiber equipped with $Na_v1.6$ channels.

4.3 Effects of axonal geometry and sodium channel distribution

Whereas $Na_v1.2$ channels are presumably located in the proximal region of the AIS $Na_v1.6$ channels are distributed along the distal section of the AIS (Fig. 4.3C middle). Furthermore, $Na_v1.2$ channels occupy approximately the proximal 1/3 of the AIS and $Na_v1.6$ channels the distal 2/3 of the AIS. When the two channels are incorporated into the model neuron and a point source electrode is shifted along its x-axis (Fig. 4.3A) compartments closest to the electrode show the largest (or smallest, depending on pulse polarity) values of V_e (Fig. 4.3B). Red regions indicate larger absolute values and blue regions indicate portions of the neuron which are not affected strongly by the applied extracellular field. Thresholds for the model neuron having various diameters along its axonal compartments (Fig. 4.3C, bottom) are lowest (2.6µA) in the distal portion of the AIS region which was also confirmed by a previous modeling study (Jeng *et al.* (2011)). Starting with high thresholds when the electrode is located close to the soma a decrease along the first 70µm in axial direction can be examined (Fig. 4.3C, top). Thresholds increase along the thin segment of the fiber because, although still influenced by the lowest threshold region proximal to it, of the higher activation threshold of $Na_v1.2$ channels in the unmyelinated axon. Approximately 200-300µm downstream the axon the steady state axonal threshold of about 6µA is reached. Thresholds are approximately one order of magnitude smaller in the AIS when the sodium channel density is increased by a factor of five.

The standard model neuron (*simplified* in all figure captions) incorporates an axonal geometry having a 30µm long hillock, a 40µm long AIS and a thin axonal segment 90µm in length. As a starting point for further simulations the lengths of the AIS and hillock were varied. Thereby, changes of the lowest threshold and the location where this lowest-threshold electrode position is located were analyzed. Minimum thresholds decrease with a larger distance between the soma and the AIS. Also increasing AIS length results in lower thresholds (Fig. 4.4A). Length variation was in the range of experimentally determined hillock and AIS lengths (Fried *et al.* (2009)). The comparison of the shortest AIS (20µm) located closest to the soma (hillock length=20µm) results in a lowest threshold of approximately 3.05µA (Fig. 4.4A, blue filled circle). Maximum hillock and AIS lengths lead to a threshold of 2.55µA (red filled circle). Simulated
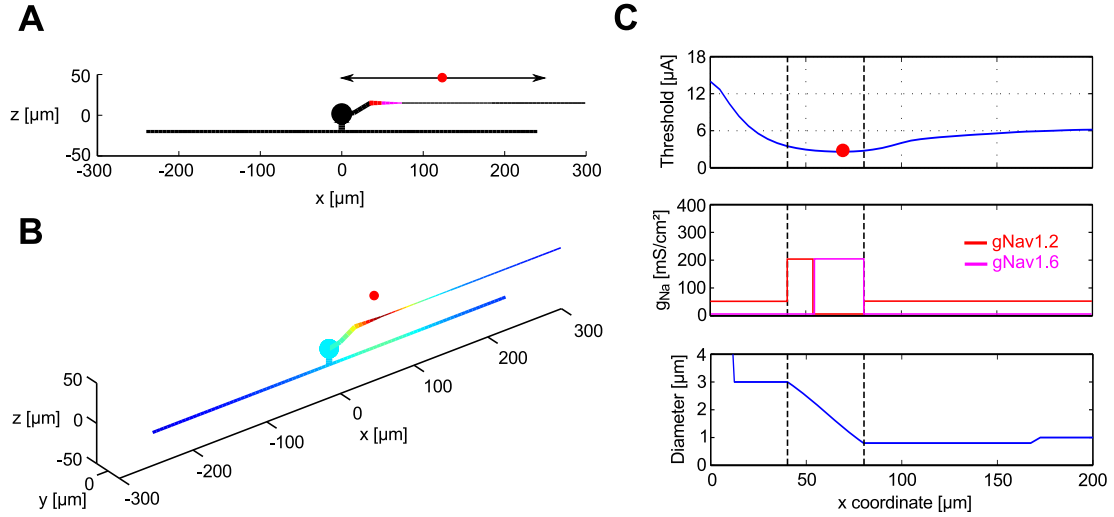
Figure 4.3: **Model neuron and its thresholds for cathodic stimulation -** (A) Schematic depiction of the model neuron. The electrode (point source, red dot) was shifted along the black line in a constant z-distance of 30µm to the AIS (proximal part in red, distal part in purple). (B) 3-dimensional view of the model neuron and external potential at compartment centers. The electrode is positioned above the AIS. Highest absolute values of V_e are color-coded in red. (C) Top: Threshold for electrical stimulation shows its minimum (red dot) in the distal part of the AIS which is located within the two dashed vertical lines (40µm-80µm). Threshold at the soma is approximately 4-5 times higher than in the AIS. Middle: The two different sodium channel types were strictly separated along the neuron. $Na_v1.2$ channels were located in the dendritic parts, the soma, the hillock, the AIS and the unmyelinated axon whereas $Na_v1.6$ channels were located only in the AIS. Sodium channel conductance was increased by a factor of 5 in the AIS (50mS/cm^2 and 250mS/cm^2, respectively). Bottom: Compartment diameter along the axonal parts of the fiber. Dendritic diameters were set to 4µm in the short vertical section connected to the soma and 2µm in the horizontal main dendrite (not shown). Model properties: *Morphology:* simplified; *Channels:* $Na_v1.2$, $Na_v1.6$, K, L; *Temp:* 37°; *Pulse:* monophasic 0.1ms; *Potentials:* analytical (ρ_e=0.1S/m).
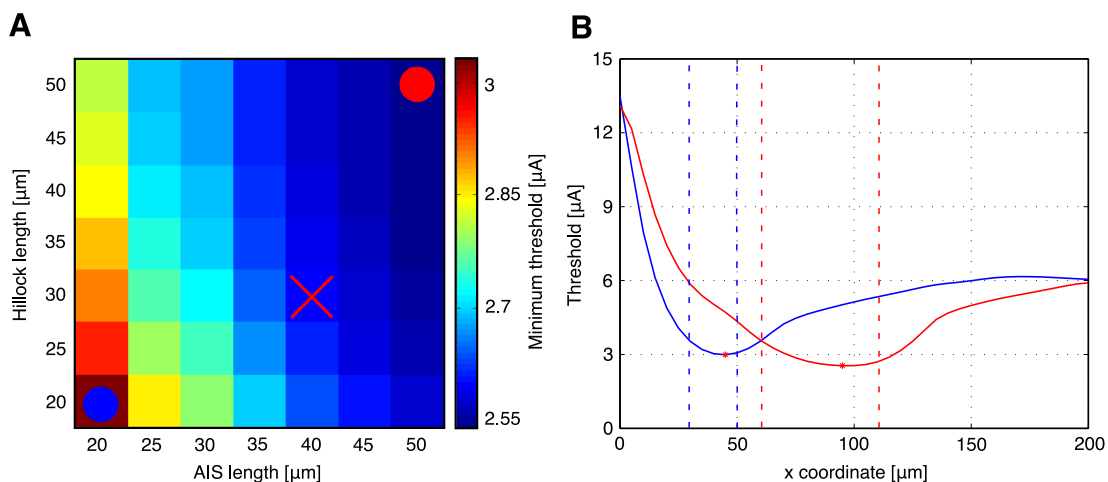
Figure 4.4: **Impact of AIS and hillock length on threshold -** (A) Minimum thresholds along the model neuron for different length parameters of AIS and hillock. Minimum and maximum AIS and hillock length was set to 20µm and 50µm, respectively (**Fried** *et al.* (2009)). Lowest thresholds occur at maximum AIS and hillock lengths. The blue and red circles correspond to the threshold curves in (B). The red 'X' indicates the standard configuration. (B) Threshold maps along the x-axis of the model neuron for parameter sets depicted by circles in (A). The two AIS regions are indicated by the vertical dashed lines. Stimuli were applied in the same configuration as in Fig. 4.3C (Point source, 0.1ms, 30µm above the AIS). Model properties: *Morphology:* simplified; *Channels:* $Na_v1.2$, $Na_v1.6$, K, L; *Temp:* 37°; *Pulse:* monophasic 0.1ms; *Potentials:* analytical (ρ_e=0.1S/m).

thresholds when the electrode is shifted along the neurons x-axis are depicted in Fig. 4.4B. All minimum thresholds measured in (A) occurred in the last quarter of the AIS, i.e. the distal end of the AIS is the location of lowest threshold independent of the length parameters.

4.4 Influence of dendritic morphology

Since far-reaching model simplifications have been made the influence of four different complex dendritic morphologies on thresholds in the AIS region was examined (Fig. 4.5). In these simulations the axonal parts of the model neurons were modeled identically: A 30µm axon hillock (diameter=3µm), the AIS spanning 40µm (tapered diameter from 3µm to 0.8µm), a thin section 90µm in length (diameter 0.8µm) and approximately 800µm of the distal axon (diameter 1µm). Ion channel expression along the axon was set like in Fig. 4.3. The dendritic region was equipped with $Na_v1.2$ and potassium

channels (maximum conductance: $50mS/cm^2$ and $12.5mS/cm^2$, respectively).

As presented in Fig. 4.5A (a) the simplest model geometry only consists of a straight dendritic morphology which was connected to the axonal part without an intermediate somatic compartment. The diameter of the dendrite was set to 1µm. Lowest threshold was located 70µm along the axon at approximately 3.1µA. Adding a 20µm soma to the simple geometry (Fig. 4.5A, (b)) results in a slightly changed threshold trace (Fig. 4.5B). Thresholds close to the soma increased heavily which can be explained by its large surface and volume. Therefore, the soma acts as a current sink which needs to be stimulated strongly in order to reach threshold. Again, the region of lowest threshold was located in the distal AIS comparable with the threshold arising from morphology (a). Morphology (c), the model neuron mainly used in this study, results in quite similar results as (a) and (b). Because the dendritic parts of the neuron are located deeper, i.e. they are located further away of the electrode than the axon, they do not have a large influence on thresholds in the AIS region. Using an actually traced dendritic morphology also results in the almost identical thresholds as when using the simplified model neuron. The complex morphology, however, consists of more than 1500 compartments whereas the model neuron only consists of 201 compartments which decreases computation time strongly.
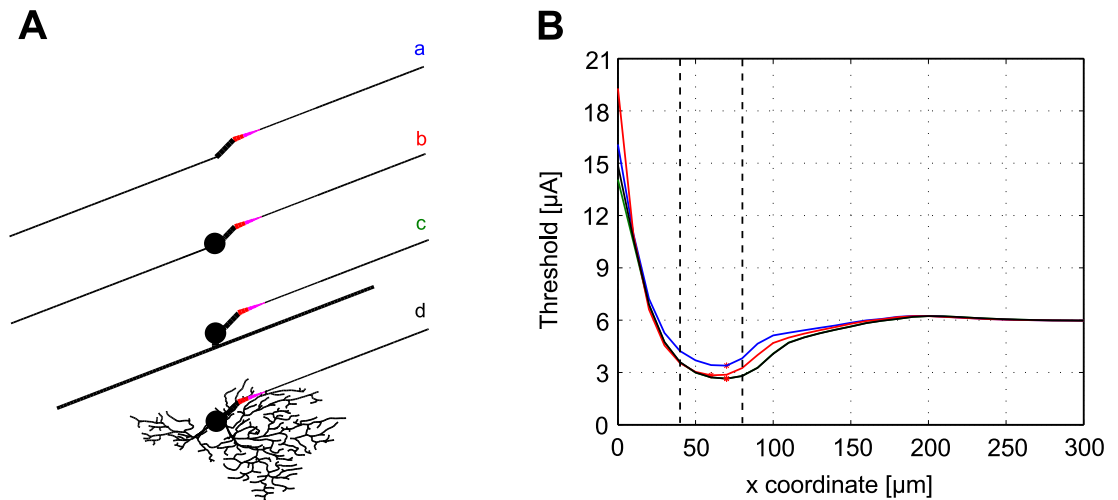
Figure 4.5: **Effect of dendrites and soma on AIS thresholds -** (A) Four different model neurons were tested to investigate if dendritic geometry has an influence on the previously presented results. Only the somatic and dendritic geometry was varied, axonal portion were modeled as in Fig. 4.3. A simple dendritic geometry lacking a soma (a), the same fiber with a 20µm spherical soma (b), the standard model neuron (c) and a GC containing a dendritic tree of an actual traced mouse OFF-P GC (Guo *et al.* (2013)) (d) (B) Thresholds when the stimulating electrode is shifted along the fibers x-direction (z distance 30µm (soma) and 45µm (axon), respectively). 0µm indicates the location of the soma. Colors correspond to the lowercase letters in (A). For all model neurons the lowest threshold is located in the AIS region and thresholds increase strongly when the electrode is shifted towards to the soma. Model properties: *Morphology:* simplified; *Channels:* $Na_v1.2$, $Na_v1.6$, K, L; *Temp:* 37°; *Pulse:* monophasic 0.1ms; *Potentials:* analytical (ρ_e=0.1S/m).

4.5   Simulations with noise

Since neuronal activity includes many random processes a noise term was added to the ionic currents in order to simulate noisy baseline activity. This noise led to variable results in repetitive simulations even when the same input parameters was used. However, recruitment curves of neuronal responses could be computed by introducing a probability for spiking at distinct amplitudes. Recruitment curves could be drawn by steadily increasing stimulus amplitude and repeat the same experiment multiple times. Thereby the probability for spiking was found. Fig. 4.6A shows a spike train at the 50% spiking probability of the model neuron. Twenty 0.1ms stimulus pulses were applied to the model neuron with an inter-stimulus interval (ISI) of 39.9ms (25Hz). Baseline noise can be seen in the voltage trace throughout the whole simulation. When an AP was initiated the membrane voltage trace becomes smoother because currents during a spike are immense higher than the small noisy currents. In the depicted time course of the membrane voltage twenty stimuli led to ten APs which results in a spike probability of $10/20 = 50\%$.

Running this simulation for different amplitudes resulted in recruitment curves as shown in Fig. 4.6B. When the stimulus amplitude was increased stepwise (0.5µA) spike probability increased from 0-100%. Fig. 4.6B shows a recruitment curve for the electrode positioned directly above the location of the lowest threshold (70µm distal of the soma). Each stimulus was presented twenty times. Until a stimulus amplitude of approximately 60% of threshold current no spikes were observed and amplitudes above 140% threshold current led to spikes all the time. A sigmoid function (Boltzmann equation, as used in Tsai *et al.* (2009)) of the form

$$SpikeProbability_{(I)} = \frac{100}{1 + exp(-(I - a)/b)}$$

was fitted to the computed data and is shown as solid red line. In this equation a and b are the parameters that determine the shape of the sigmoid and I denotes the stimulus amplitude in percentage of the threshold current. a describes the stimulus amplitude of the inflection point of the curve which is close to the 50% spiking probability whereas b characterizes the slope of the sigmoid. 50% threshold probability was determined at
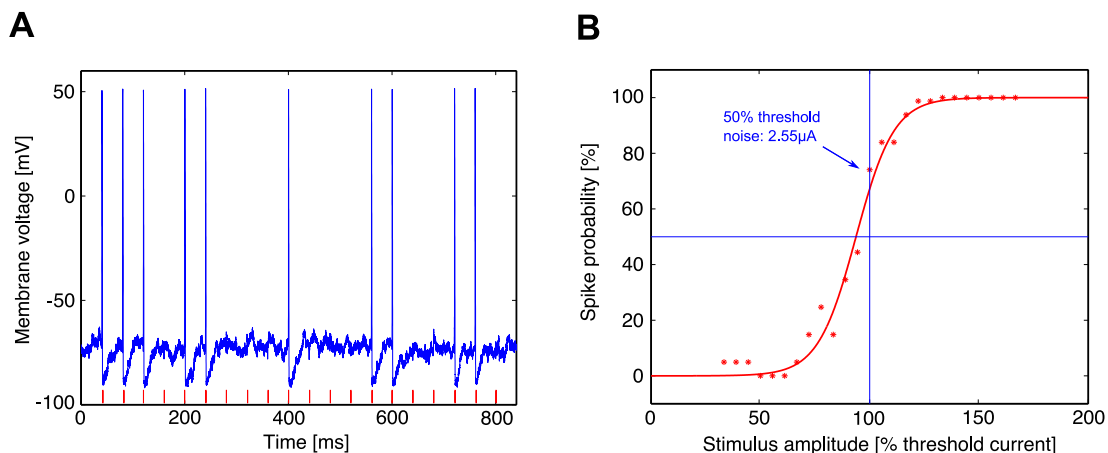
Figure 4.6: **Recruitment curve for stimulation above the AIS -** (A) Response of the model neuron to 20 pulses (indicated in red) at 2.55µA. 10 spikes are initiated which corresponds to a 50% spike probability. The electrode was positioned at the location showing the minimum threshold 70µm from the soma in the AIS region (see Fig. 4.3). (B) Recruitment curve for the same electrode location. The continuous red trace denotes a fitted sigmoid function. Threshold amplitude was determined at 2.55µA which led to more than 50% spike probability. Model properties: *Morphology:* simplified; *Channels:* $Na_v1.2$, $Na_v1.6$, K, L, noise ($k=0.02µA/\sqrt{mS}$); *Temp:* 37°; *Pulse:* monophasic 0.1ms; *Potentials:* analytical ($\rho_e=0.1S/m$).

2.55µA (Fig. 4.6B). which is comparable to the absolute (fully determined) threshold when the noise current was turned off (2.65µA).

By varying the noise factor k it was possible to change the shape of the resulting sigmoid functions (Fig. 4.7A). Low values of k ($<0.01µA/\sqrt{mS}$) resulted in sigmoids with a steepness which is not in the range of experimental determined results (see data in table 4.1 and Fried *et al.* (2009); Sekirnjak *et al.* (2008); Tsai *et al.* (2009)). Values from 0.01 and $0.02µA/\sqrt{mS}$ led to fitted response curves with a comparable steepness to measured data.

In order to examine the influence of the fluctuations of the membrane currents on spontaneous spike activity was computed. Noise influence was monitored over a period of 2s and the spontaneous spiking rate was plotted against increasing k (Fig. 4.7). No stimulus was applied during the simulation. First spontaneous spikes could be observed when k is increased to $0.025µA/\sqrt{mS}$. Further increase of k led to a quasi linear increase of spike frequency. Approximately 50 spikes per second occurred when k is set to $0.05µA/\sqrt{mS}$. In sum, values for k which resulted in comparable recruitment

Cell Type	a	b	R^2	RMSE
EXP, ON	98.0 (96.8, 99,2)	5.6 (4.2, 6.9)	94.5%	8.6
EXP, OFF	93.7 (90.7, 96.6)	9.6 (6.1, 13.0)	98.5%	12.2
EXP, ON-OFF	96.1 (90.6, 101.6)	16.2 (9.5, 22.9)	93.9%	8.9
SIM, k=0.01	99.9 (99.4, 100.4)	4.7 (4.2, 5.2)	99.8%	2.0
SIM, k=0.015	97.8 (96.4, 99.2)	7.1 (5.8, 8.4)	99.1%	4.6
SIM, k=0.02	93.8 (92.2, 95.4)	8.7 (7.3, 10.1)	99.0%	4.5

Table 4.1: **Parameters for fitted Boltzmann equations in experiments and simulations - ** Experimental determined parameters for ON, OFF and ON-OFF GCs result in differently shaped sigmoid curves (Fig. 4.7A). The same can be shown in simulations by varying the noise factor k. R^2=goodness of fit, RMSE=root mean squared error. Experimental data from Tsai *et al.* (2009).
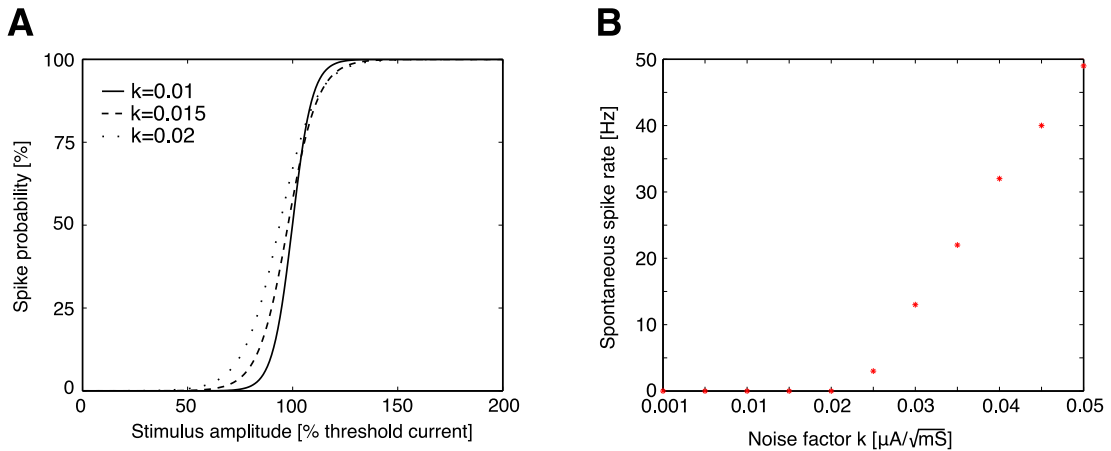

Figure 4.7: **Shape of recruitment curves is determined by noise factor k - ** (A) Recruitment curves for stimulation at the AIS for three different values of k. Whereas small values of k led to steep sigmoids higher values led to a broadening of the curve. Data for the three traces is given in table 4.1. (B) At low values of k no spontaneous spiking occurs. Starting at $k=0.025\mu A/\sqrt{mS}$ spontaneous activity increases linearly. Simulation duration was 2s and no stimulus was applied. Model properties: *Morphology:* simplified; *Channels:* $Na_v1.2$, $Na_v1.6$, K, L, noise (k=variable); *Temp:* 37°; *Pulse:* monophasic 0.1ms or none; *Potentials:* analytical (ρ_e=0.1S/m).

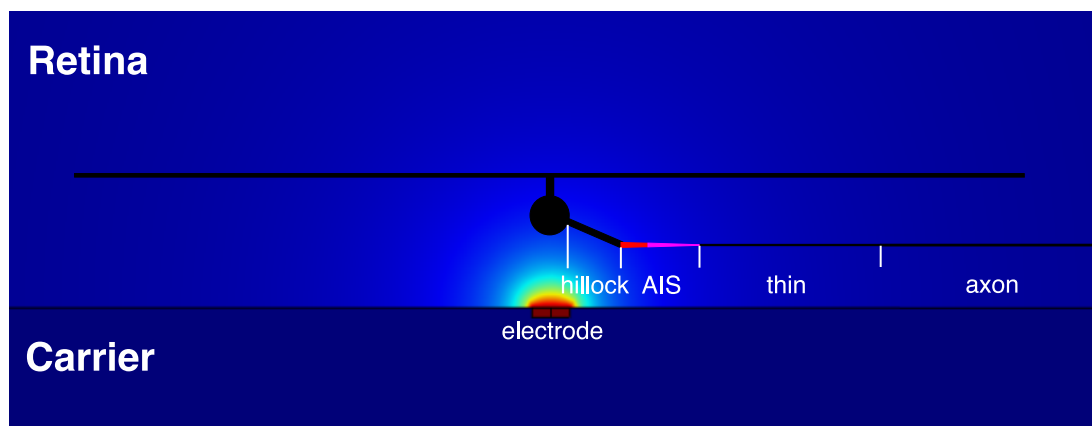Figure 4.8: **Extracellular potentials generated by a disc electrode -** The model neuron is placed 30µm (axon) and 45µm (soma) distant below the electrode. Generated potentials decrease in concentric circles with increasing distance from the electrode.

curves as presented in previous studies were not able to generate spontaneous activity in the model neuron.

4.6 Focal stimulation of GCs

The focal activation of GCs is one of the major aims of retinal prostheses. Precisely initiated spikes in closely packed GCs without activating GCs located far distant is the basis for artificial phosphenes without blurring. This often observed blurring effect arises because of the co-activation of passing axon fibers. Therefore, it was examined if, and if yes in which extend, focal activation can be achieved by exploiting the low threshold region related to the AIS. The following simulations are all conducted using the finite element model in order to compute the extracellular potentials generated by a 20µm disc electrode (Fig. 4.8).

The axonal threshold, i.e. the threshold when the stimulating electrode is located afar of the AIS, of the presented model neuron is approximately 3.18µA and therefore higher than the threshold of multiple GCs that are located close to the electrode (Fig. 4.9). In this simulations noise fluctuations were turned off. Lowest threshold again can be observed if the electrode is located close to the AIS region, however, also electrode locations closer to the soma and further distant in y-direction have lower thresholds than the unmyelinated axon. As depicted in Fig. 4.9, 18 GCs (indicated in red) have
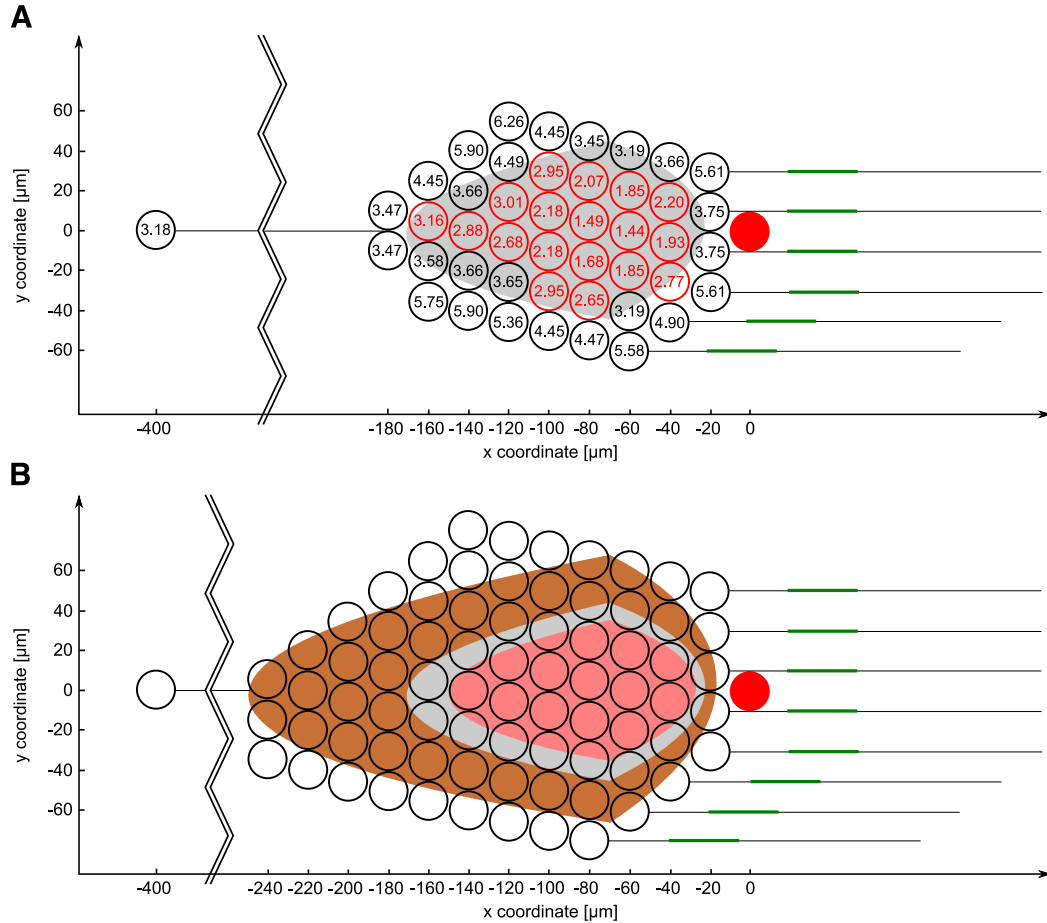
Figure 4.9: **Focal activation of GCs -** Multiple densely packed RGCs are activated at different thresholds by a disc electrode (diameter 20µm, filled red circle). The spacing between the cells was 20µm in x-direction and RGC columns were shifted in 5µm steps vertically (y-direction). (A) Activation threshold for each RGC location is marked in the somas of the RGCs. One passing axon with its soma 400µm distant to the electrode has a spiking threshold of approximately 3.18µA. 18 RGCs (marked red) have lower thresholds than the passing axon and can therefore be focally activated. The grey shaded region indicates RGC locations with thresholds lower than of the passing axon. The AIS region (green bar, only shown for the most right RGCs) is 30µm distal of the cell body and has a length of 40µm. (B) Depending on the diameter of the passing axon the region that can be activated focally in- or decreases. Doubling the axonal diameter of the passing axon decreases axonal threshold and therefore decreases the size of the shaded region (red). A reduction of the fiber diameter by a factor of 2 enlarges the region where focal activation might be possible (brown). The grey shaded region indicates the same domain as in (A). Model properties: *Morphology:* simplified; *Channels:* $Na_v1.2$, $Na_v1.6$, K, L; *Temp:* 37°; *Pulse:* monophasic 0.1ms; *Potentials:* FEM (ρ_e=0.1S/m).

lower thresholds than the passing axon. The grey shaded region depicts a boundary for focal stimulation. RGCs inside this region have smaller thresholds than the passing axon and therefore can be activated focally.

The diameter of the passing axon also influences the possibility of focal RGC activation. Thicker fibers have lower thresholds than thin fibers and therefore the shaded regions in Fig. 4.9B change their sizes. When the axonal diameter is doubled only RGCs within the red shaded region have lower thresholds than the passing fiber. Decreasing the fiber diameter of the passing axon to 0.5µm (1/2 of the standard diameter) results in an enlarged region indicated in brown.

4.7 Electrode size and safety limits for electrical stimulation

Current retinal implants use stimulating elements with diameters in the range of 50 up to hundreds of micrometers. Therefore, the electrode in the finite element model was varied and various thresholds such as current (density) and charge (density) were computed (Fig. 4.10). As reported previously, larger sized electrodes lead to higher currents necessary for fiber activation. A rather small electrode, only 5µm in diameter has a threshold of about 1.35µA whereas a 25µm electrode results in a threshold about 10% higher (Fig. 4.10A). Also the applied charge increases monotonically (4.10B). Current density and charge density, however, are decreasing when electrode size is increased (Fig. 4.10C & D). This fact is important for safe electrical stimulation since an exceeding of the agreeable charge limit can lead to severe tissue and/or electrode damage. For commonly used platinum-(iridium) electrodes this charge limit is stated to be around 100-350µC/cm^2 (Brummer & Turner (1977); Rose & Robblee (1990), yellow region in Fig. 4.10D). In the presented simulations only electrodes having diameters smaller than 15µm led to charge densities in the critical region. Stimulation at threshold with the standard 20µm electrode led to a charge density almost one order of magnitude smaller than the proposed lower bound for safe stimulation. Fig. 4.10 shows results in close agreement with data of an electrophysiological study by Sekirnjak and coworkers (Sekirnjak *et al.* (2006)).
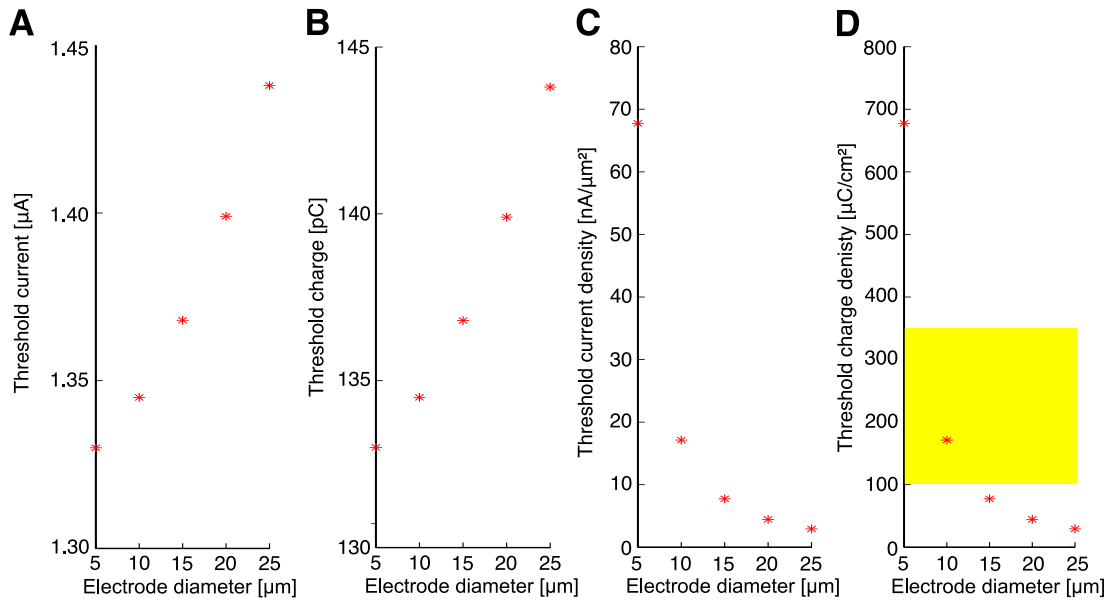
Figure 4.10: **Impact of electrode diameter on threshold parameters -** (A) Thresholds were determined for electrodes having diameter between 5 and 25µm. Smallest thresholds were found for the smallest electrode as reported previously. (B) Threshold charge is also monotonically increasing when electrodes become larger. (C & D) Threshold current density and threshold charge density decrease when the disc electrodes have larger diameters. The yellow region in (D) denotes lower and upper bounds for safe stimulation. The shown figure resembles measured results presented by Sekirnjak and coworkers quite closely (Sekirnjak *et al.* (2006). Model properties: *Morphology:* simplified; *Channels:* $Na_v1.2$, $Na_v1.6$, K, L; *Temp:* 37°; *Pulse:* monophasic 0.1ms; *Potentials:* FEM (ρ_e=0.1S/m).

4.8   Electrode size and site of spike initiation

The location within a nerve fiber where an AP occurs is often of interest for neuro-prostheses. Knowledge about site of spike initiation (SSI) can make stimulation more predictable and therefore more precise and focal. To examine the effects of electrode diameter on the SSI a simple stick model containing only sodium ($Na_v 1.2$), potassium and leak currents was established. The diameter was set to a constant value of 1µm and length was 2000µm. Stimulation was applied in the center region of the fiber and no edge effects were examined during stimulation.

As known from previous work (Rattay (1988)) the activating function for electrodes with diameters of several tens of micrometers looks quite different than the activating function of a perfect point source. The *classic* activating function for point source electrodes has either a maximum (cathodic) or a minimum (anodic) directly below the electrode (Fig. 4.11, Rattay (1986), see also 2.3). Furthermore, two positive (anodic) or negative (cathodic) shoulders arise to the left and the right of the maximum/minimum of the activating function. The zero crossings of the activating function are located in a 70 degrees angle from the point source. Therefore, electrode-to-fiber distance is a highly important parameter for investigation of SSI.

Because compartments at the end of a fiber, e.g. dendritic end compartments, are only connected to one additional compartment their activating function is not proportional to the second derivative of the applied voltage but to its first derivative. This change of the activating function and the consequent larger (positive or negative) values of activating function increase the chance of spike initiation at fiber edges (Fig. 2.6).

For disc electrodes, however, the shape of the activating function changes strongly. Two peaks at approximately the edges of the electrode have maximum (cathodic) or minimum (anodic) values whereas directly below electrode center the activating function almost drops to zero for large diameters (Fig. 4.11, see also Rattay (1988)).

The fact of a totally different shape of the activating for disc electrodes results in interesting changes in the SSI. Whereas stimulation with a point source always leads to spikes to be generated either directly under the electrode (cathodic) or at the two shoulders having positive activating function values when anodic stimulation is applied. Cathodic stimulation with a 50µm disc electrode at threshold led again to
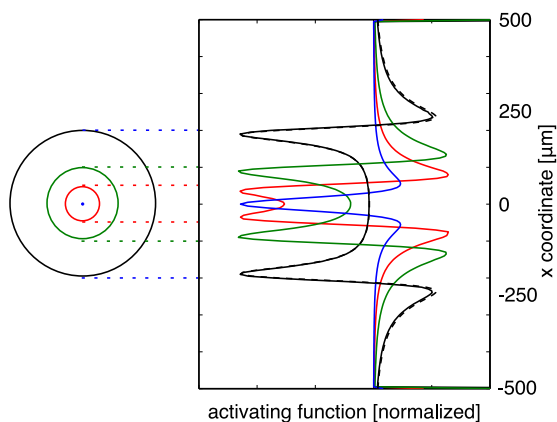
89

Figure 4.11: **Activating function shape changes from point source to disc electrode** - Activating functions for a cathodically stimulated fiber, 30µm below the electrode, are shown for a point source (blue) and 3 disc electrodes (d=100, 200, 400µm). Whereas the peak of the activating generated by the point source had its maximum exactly below the electrode the activating functions for disc electrodes had their maxima nearby of the electrode edges. A comparison between the activating function computed from extracellular potential generated by the FEM model (black) and by an analytical solution in homogeneous medium (Wiley & Webster (1982), dashed) showed no significant differences. (Left) Corresponding size of the electrodes, colors correspond to the right panel.

an AP that occurred at the fiber center and propagated in both directions sideways (Fig. 4.12A, top). Stimulation at supra-threshold (110% threshold) changed the picture of activation. Compartments directly under the edges of the electrode were the first compartments to spike (Fig. 4.12A, bottom, red lines). The generated APs traveled from both of these points sideways. The two spikes subsequently met at the center of the fiber annihilated each other whereas the other two spikes traveled sideways in both directions. Also spike latency decreased by almost 1ms. An electrode having a diameter of 200µm led to similar results except that even a small increase of the stimulus amplitude (1%) changed the SSI (Fig. 4.12B). Again, at threshold one AP in the middle of the fiber was generated (Fig. 4.12B, top, blue line) whereas slightly higher amplitude resulted in two spikes below the electrode edges (Fig. 4.12B, bottom, red lines).

The explanation for these surprising activation characteristics is the axial flow of currents along the fiber. This electrotonic current flows sideways from both electrode edges and therefore activation is largest in compartments at the midpoint of the elec-

trode where axial currents from both sides depolarize the cell membrane most. These compartments consequently are the SSI, however, just at threshold and little (depending on fiber thickness and intracellular resisitivity) above. By applying suprathreshold stimulation activation at compartments below electrode edges are depolarized sufficiently to initiate a spike. With larger electrodes the increase of amplitude to achieve this type of activation gets smaller (1 vs. 10%) because of a larger distance between the two electrode edges. Subsequently, electrotonic currents have to bridge this larger distance which favors activation at compartments below the electrode edges, even at amplitudes just above threshold.
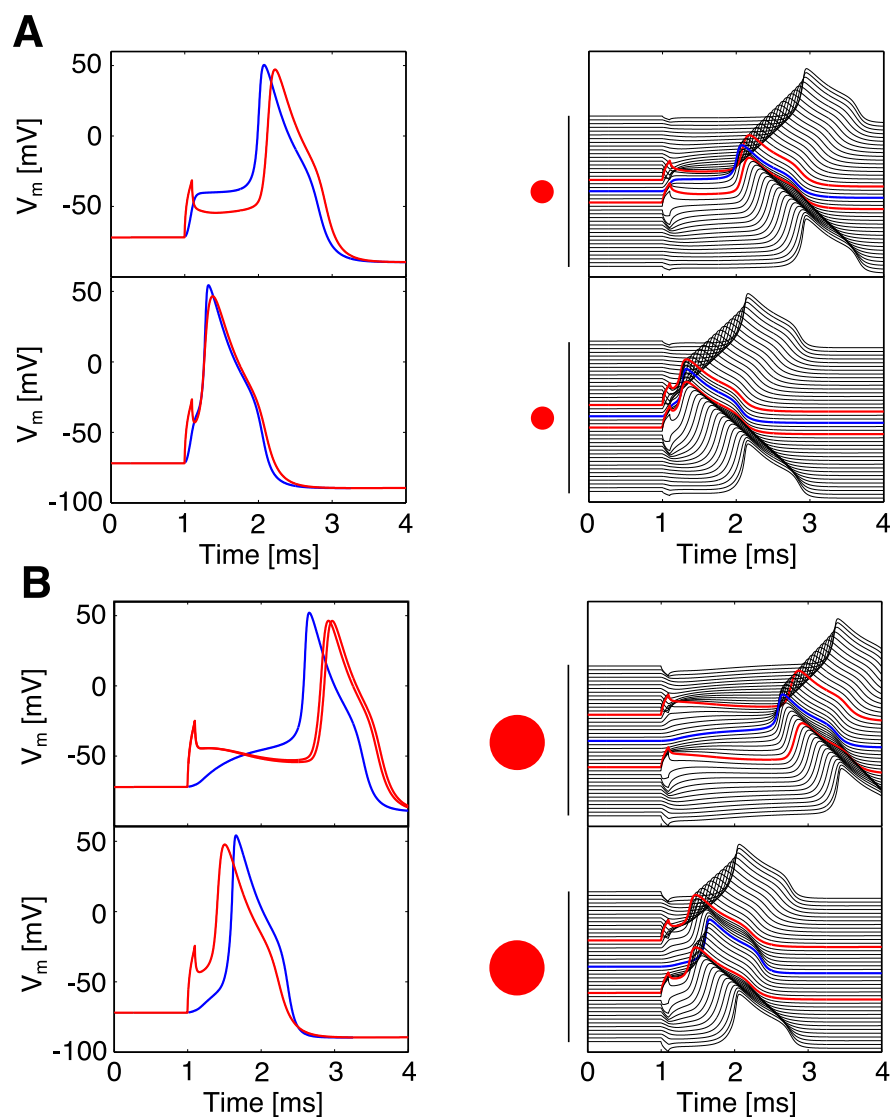
Figure 4.12: **Supra-threshold stimulation changes the SSI -** A simple stick model was cathodically stimulated with disc electrodes different in size. (A) Stimulation at threshold with a 50µm electrode resulted in a single spike in the middle of the fiber (top). Strong excitation at the electrode edges was transferred axially along the axon. At threshold the AP was generated at the midpoint of the fiber. A stimulus with 110% of the threshold amplitude led to two APs below the electrode edges (bottom). (B) Stimulation with a larger electrode (200µm in diameter) showed the same cAPharacteristics. Stimulus amplitude, however, had only to be increased by 1% to generate two spikes at the edges. In both cases (A & B) spike latency was decreased strongly when supra-threshold stimulation was applied. The electrode position and size above the fiber (black vertical line) is indicated by filled red circles. Model properties: *Morphology:* stick (d=1µm); *Channels:* $Na_v1.2$, K, L; *Temp:* 37°; *Pulse:* monophasic 0.1ms; *Potentials:* FEM (ρ_e=0.1S/m).

4.9   Pulse polarity and site of spike initiation

In a next step the influence of cathodic and anodic pulses on threshold and the SSI
were examined. Generally, in the peripheral nervous system with its long uniform axon
fibers cathodic pulses are known to result in lower thresholds than anodic stimuli which
can also be explained by the activating function. Complex geometries and non-uniform
ion-channel distributions, however, may result in unknown activation patterns.

Thresholds along the axon were plotted to visualize the influence of the electrode-to-
fiber distance (Fig. 4.13A). The electrode was shifted along the neuron in 30µm, 45µm
and 60µm distance, respectively. During cathodic stimulation lowest thresholds occured
in the AIS region in all three cases (Fig. 4.13A, left). Anodic stimulation, however, re-
sulted in differently shaped threshold maps (Fig. 4.13A, right). Lowest thresholds were
determined when the electrode was located close to the soma. An apparent arbitrary
in- and decrease of thresholds with sharp changes of the trace could be examined for
all three tested electrode-to-fiber distances. Encouraged by these arbitrary threshold
traces the underlying activation mechanisms and SSI were examined.

For the case of cathodic stimulation a quite simple activation pattern arised. Whereas
the AIS was the SSI for locations close to the soma ($\leqslant$100µm, blue shaded region) elec-
trode locations further down the axon resulted in axonal spiking ($\geqslant$100µm, red shaded
region, Fig. 4.13B, left). A strict border between AIS-spiking and axonal spiking,
however, could not be made because both region were located just next to each other
and thus a flowing transition arose.

During anodic stimulation, on the other hand, surprisingly also activation of den-
dritic compartments at certain electrode locations occurred (4.13B, right). Similar to
cathodic stimulation the AIS was also the SSI when the electrode was positioned above
the soma and the parts of the hillock ($\leqslant$30µm, blue shaded region). In a region of
approximately 120µm the SSI changed to either the left or the right edge compartment
of the dendritic tree (30-150µm, brown shaded region). Beyond this region axonal spik-
ing started to emerge, however, without a constant threshold ($\geqslant$150µm, red shaded
region). Until a beginning threshold decrease at $\sim$220µm spiking was generated in
compartments which were located below the right positive shoulder of the activating
function. At the onset of the last dip in the threshold trace compartments close to the

left shoulder of the activating function became the SSI which was associated with a pronounced local minimum at 250µm. An almost constant axonal threshold was reached when the electrode was shifted more than 400µm down the axon.
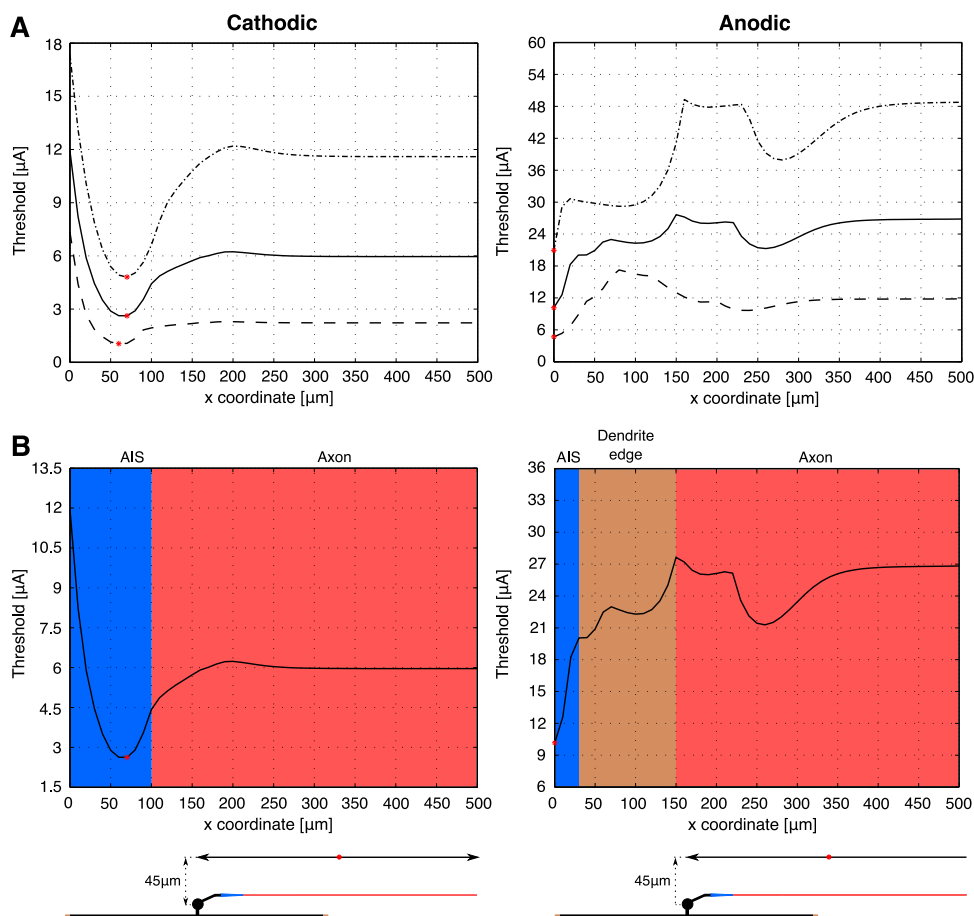
Figure 4.13: **Pulse polarity and SSI -** (A) Activation threshold for three electrode-to-fiber distances (30µm (dashed), 45µm (solid), 60µm (dashed-dotted)). Cathodic pulses (left) led to the typical shape of the threshold maps as shown before. The minimum was reached when the electrode was positioned in the distal part of the AIS. Thresholds for anodic stimulation (right) did not follow such a simple pattern. The threshold minimum occurred when the electrode was located close to the soma and steadily increased for at least 80µm, depending on electrode-to-fiber distance. (B) Site of spike initiation for the 45µm threshold maps from (A). For electrode locations from the soma to approximately the middle of the thin segment ($\leqslant$100µm) the AIS was the SSI during cathodic stimulation (blue shaded). Shifting the electrode further distal resulted in spiking in the distal axon as predicted by the activating function (red shaded). Anodic stimulation on the other hand could also lead to dendritic spikes for certain electrode locations. In a region between 30µm and 150µm one of the two edge compartments of the dendrite was the SSI (brown shaded). Similar to cathodic stimulation electrode locations close to the soma ($\leqslant$30µm) resulted in AIS spikes (blue shaded). Axonal compartments initiated APs when the electrode was shifted more than 150µm along the axon (red shaded). Model properties: *Morphology:* simplified; *Channels:* $Na_v1.2$, $Na_v1.6$, K, L; *Temp:* 37°; *Pulse:* monophasic 0.1ms; *Potentials:* analytical (ρ_e=0.1S/m).

4. PART II: GANGLION CELL STIMULATION

Latency plots

So far, simple visual inspection of membrane voltage over time was used in order to determine SSI. Spike latency, i.e. the delay until an elicited AP arrives at a certain position in the neuron, can also be used to determine a change in SSI. In this examination spike latency was measured as the delay between the onset of the stimulus and a measured spike (membrane voltage crosses 0mV) at the soma which is related to an experimental recording in the soma. Stimulus amplitude was set to 101% of threshold in order to eliminate shifts in timing arising from the threshold determination procedure.

In the cathodic case, as mentioned before, it was not straightforward to draw a solid border between AIS-spiking and spiking in the distal axon. By plotting spike latency versus electrode location, however, two distinct spike timing regions could be determined (4.14A). When the electrode was shifted along the first 100µm latency first decreased to a minimum which approximately corresponded with the threshold minimum (about 50-70µm) and further started to increase when the electrode was shifted beyond the AIS. This pattern arised since for electrode locations close to the soma the SSI was located within the AIS and therefore an AP had to propagate back to the soma which was associated with a larger spike latency. The same mechanisms explained the increase of latency after the electrode was shifted beyond the AIS. Somewhere between an electrode shift of 100-110µm spike latency increased noticeably which apparently was an indicator for a change in SSI. From this point a shift towards the distal portion of the electrode corresponded with an almost linear increase of spike latency. This linear increase again could be explained by a linear increase of the distance between SSI and the soma.

The latency vs. electrode shift plot for anodic stimulation revealed five distinct regions with changing SSI (4.14B). At first sight, this is in opposition to the results from Fig. 4.13B (right), however, a closer inspection clarified and explained the detailed spike initiation mechanisms. Two of the originally three distinct regions from Fig. 4.13B (right) could now be even further divided. Only the region with spikes generated in the AIS ($\leqslant$20µm) was clearly associated with minimum spike latency similar to the cathodic case. The two remaining regions could be further subdivided. Thresholds for electrode locations where the SSI was located in the dendritic part of the neuron showed two local minima in Fig. 4.13B (right). These two regions nicely corresponded to the two

distinct regions in the latency plot. Both regions were similar in shape since the distance between SSI, i.e. either the left or the right dendritic edge compartment, and the soma are the same in the model neuron. As determined in Fig. 4.13B (right) beyond an electrode shift of 150µm the axon became the SSI. However, this region could be divided into two separate subsections by inspection of the latency plot. Electrode locations just beyond a 150µm shift corresponded to a SSI in compartments below the right positive shoulder of the activating function, that is, compartments which are located right of the location of the electrode spiked first. By further shifting the electrode to more distal locations the SSI changed ($\sim$220µm) to axonal compartments left to the electrode location and was further associated with smaller latency because these compartments were closer to the soma (recording). This happened because at these locations the AIS region started to facilitate spike generation in these compartments. This was also visualized in Fig. 4.13B (right) with a dip in the threshold map corresponding to support from the AIS.

Spike initiation plots

Figures 4.15 and 4.16 give closer insights into spike generation during stimulation with cathodic and anodic stimuli. Thereby, two totally different activation patterns could be observed for both polarities. The depiction of membrane voltage for all compartments at different points in time was plotted twice for both paths along the neuron: i) from the left dendritic portion and ii) from the right dendritic portion via the soma along the axon.

Fig. 4.15 shows the spike initiation and propagation for cathodic stimulation at three different locations along the fiber. Stimulation above the soma (A) and at the location resulting in lowest threshold (70µm, B) led to spikes within the AIS. Stimulation at 0µm naturally activated the soma and its surrounding most but axial currents along the axon led to spike generation in the AIS. When the electrode was shifted to 250µm an AP was generated directly below the electrode in the distal axon (C). Thresholds more distal from this location did not vary any more which indicated pure axonal spiking (i.e. without support of the AIS).
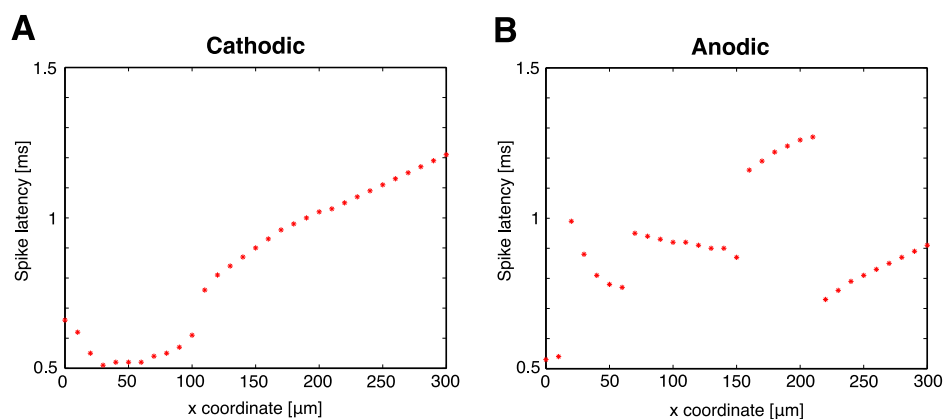
Figure 4.14: **Spike latency visualizes SSI -** Spike latency could also be used to determine a change in SSI. Spike latency was defined as the time between stimulus onset and the recording of an AP at the soma. An AP was recorded when membrane voltage crossed 0mV and latency was further determined at 101% threshold. (A) During cathodic stimulation spike latency for different electrode locations could easily be interpreted. Spikes were initiated within the AIS for electrode locations $\leqslant$100µm. When APs were initiated within axonal compartments latency started to increase linearly because of a larger distance between SSI and soma. Simulated results are also in good qualitative agreement with an experimental study (Eickenscheidt & Zeck (2014)). (B) Monitoring latency for anodic stimulation revealed five distinct regions of SSI. According to Fig. 4.13B (right) spikes were initiated either in the AIS ($\leqslant$20µm), the left (20-60µm) or right (70-150µm) dendritic edge compartment and below either the right (160-210µm) or left ($\geqslant$220µm) positive shoulder of the activating function. During bot, anodic and cathodic stimulation latency for electrode locations within the proximal axon ($\leqslant$ 150µm) was between 0.5 and 1ms which is in the range of experimentally determined latencies (Alex Hadjinicolaou, personal communication).
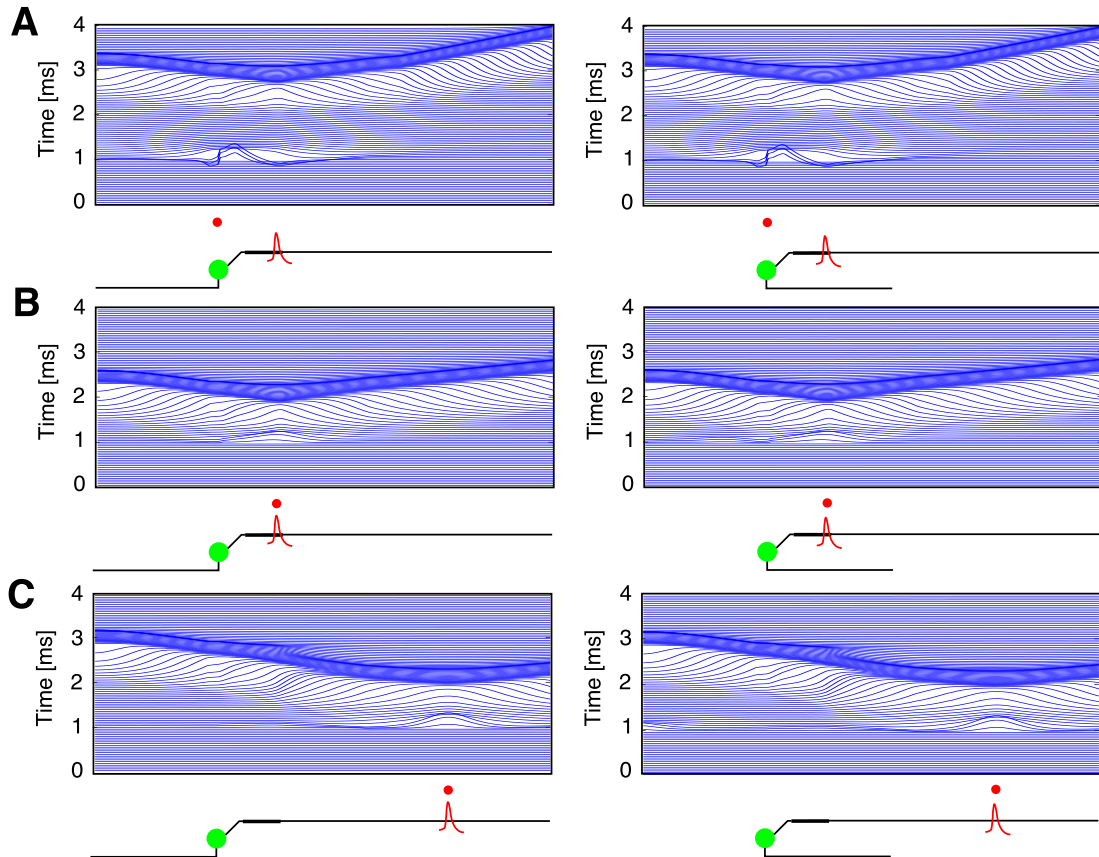
Figure 4.15: **Activation characteristics during cathodic stimulation -** In order to investigate spike generation membrane voltage of each compartment was plotted at multiple points in time. Stimulus amplitude was set 1% above threshold. Electrode location was set to 0µm (soma, A) 70µm (minimum of cathodic thresholds, B) and 250µm (C). For each electrode locations two separate panels are shown which depict the propagation of the AP along two pathways: i) from the left dendritic part across the soma along the AIS and axon (left) and ii) from the right dendritic portion along the neuron (right). Except for regions from the soma to the distal part of the AIS (A) the SSI was located directly below the electrode (B & C). Since APs were always initiated in the axonal portion of the neuron and the model neuron had a symmetric dendritic tree left and right panels are almost identically except during the duration of the pulse. Electrode location (red dot) and SSI (red AP) are shown in each panel.

4. PART II: GANGLION CELL STIMULATION

Interpretation of anodic stimulation is more complicated than for cathodic stimulation. The correlation between location of the stimulation electrode and the region of a fiber which is likely to generate a spike was not intuitive anymore. The two positive shoulders around the negative center region together with certain geometric properties and unevenly distributed ion channels led to astonishing activation mechanisms. Not only that threshold was lowest at electrode locations close to the soma but also that the SSI was transferred from the axon to the dendritic tree. Lowest thresholds at the soma could be explained with the fact that at these locations one positive shoulder of the activating function is close to the AIS (Fig. 4.16A). Of course, electrode-to-fiber distance is a crucial parameter for this finding since the activating function broadens for larger distances (70 degrees rule, Rattay (1986)). When the electrode was shifted 40µm along the axon the SSI was located within the left dendritic part of the fiber (Fig. 4.16B). Activation of the left fiber edge was triggered by a strong activation of the primary neurite (i.e. the thick vertical portion of the model dendrite). Whereas the left part of the dendrite got depolarized along all of its compartments the right portion was hyperpolarized between the soma and the fiber edge. This prevented the right edge of the dendrite to become SSI. By shifting the electrode slightly further to 110µm a spike was triggered in the right edge compartment of the dendrite (Fig. 4.16C). Again, some compartments in the right portion of the dendrite were hyperpolarized, however, the driving force at the edge compartment was strong enough to initiate an AP which is able to traverse through the whole neuron. At 200µm the right positive shoulder of the activating function triggered an AP in the distal axon right to the electrode location (4.16D). By further shifting the electrode to 250µm (4.16E) the SSI changed to the left positive shoulder of the activating function. The support of the AIS could be seen in the dip of the threshold map in Fig. 4.13B.
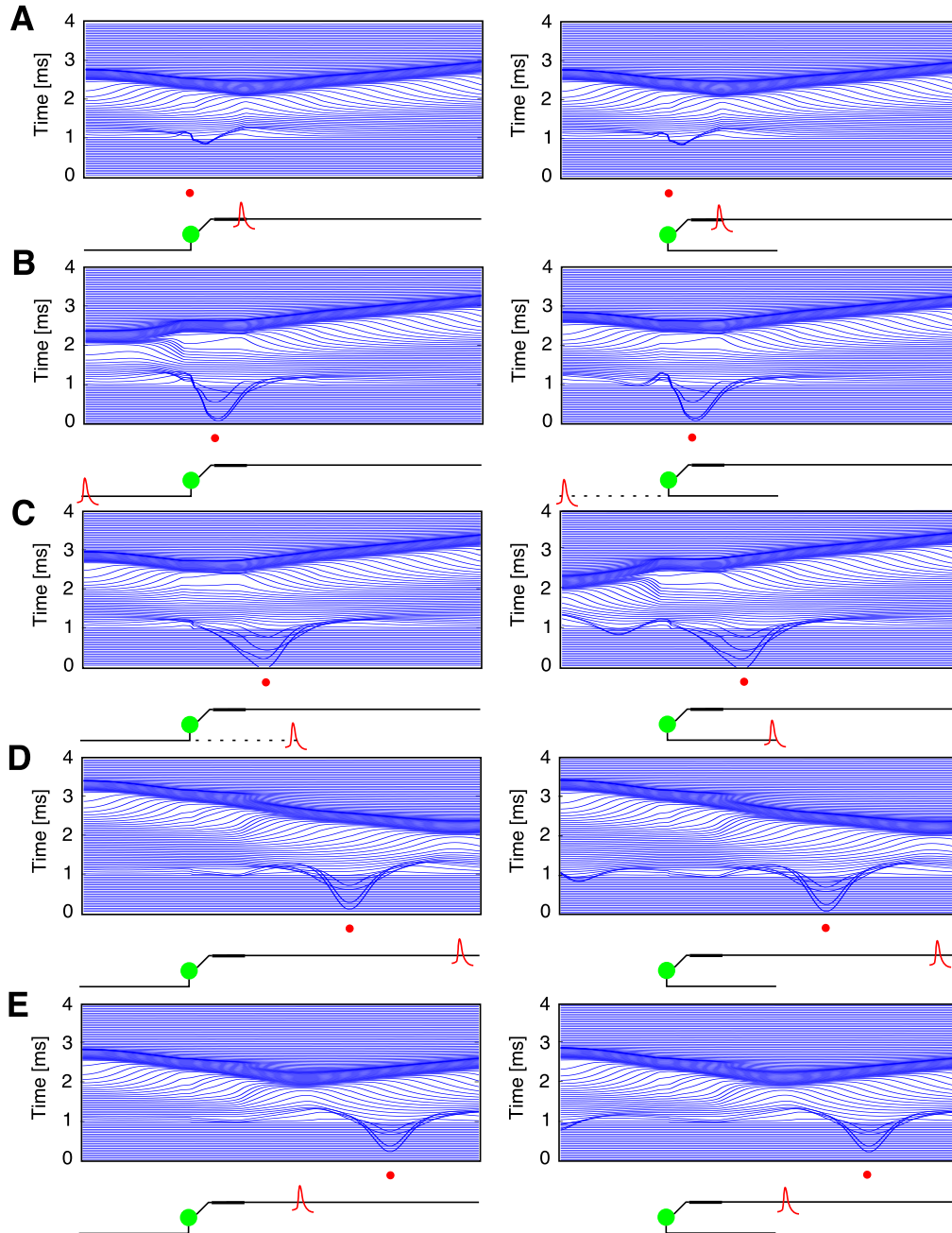
Figure 4.16: **Activation characteristics during anodic stimulation -** The same depiction as in Fig. 4.15 was used to examine how and why spikes are initiated in certain parts of a neuron. Electrode location was 0µm (A), 40µm (B), 70µm (C), 200µm (D) and 250µm (E).

101

4. PART II: GANGLION CELL STIMULATION

Dendritic spike initiation

Although it was already reported that fiber edges are likely to be the SSI (Rattay (1999)) the results from the previous section seemed to be somewhat surprising. Therefore, the fact that neither the AIS nor the axon but the dendritic edge compartment was the SSI for certain electrode locations led to further investigations. Several simulations were repeated i) at increased threshold amplitudes; ii) with a modified model neuron; iii) with modified membrane kinetics; and iv) with a traced GC dendritic morphology.

Threshold amplitude

Threshold level for the model neuron was always determined as the amplitude which was able to trigger an AP in the neuron. The generated AP was always measured at the soma. In actual electrophysiological experiments, however, spiking has not a distinct threshold but many random processes change threshold little for each experimental run. Therefore, experimental thresholds are mostly determined by the amplitude which elicits a certain number of APs during the stimulation protocol (see also section 4.5). Therefore, latency plots for different amplitude levels at threshold and above were compared. If stimulus amplitude was increased to 101% threshold the latency plot could be divided into five distinct regions (4.14B). By increasing stimulus amplitude to 105, 110 and 125% of threshold three of these five regions remained distinguishable (data not shown). Only the first two regions of AIS and dendritic spiking were not clearly differentiable any more at these amplitudes. Spike initiation sometimes changed from the dendritic edge into the middle part of the dendrite.

Modified model neuron

In order to examine how sensitive dendritic activation is to geometric modification of the model neuron the dendritic diameter (both, horizontal and vertical part) was decreased by a factor of 2 and 4, respectively. In this case, edge activation was not as dominant as in the original model neuron, however, also in these configurations the dendrite could be the SSI. For the thinnest tested case (horizontal dendrite 0.5µm and vertical dendrite 1µm) not the edge compartments were initiating APs but the primary neurite triggered spikes.

Fohlmeister model

Spike generation and propagation was also examined with changing the membrane ion channel equipment and channel densities to the Fohlmeister model (Fohlmeister *et al.* (2010)). The neuron was equipped with sodium, potassium, calcium, calcium activated potassium and leak channels. Temperature was set to 37.1° Celsius. Resulting threshold maps for cathodic and anodic stimulation are similar to the ones previously shown, however, thresholds are lower by approximately a factor of 2 (data not shown). With kinetics of the Fohlmeister model simulations sometimes resulted in spike initiation at the AIS but lacked back-propagation to the soma. In sum, also simulations with incorporated Fohlmeister dynamics supported the assumption that the dendritic tree contributes to spike initiation.

Traced GC morphologies

The final step in the investigation of dendritic influence on spike initiation the morphology of a traced mouse GC was used (available at `neuromorpho.org`, tracing performed by Kong *et al.* (2005). Dendritic diameter was not available for the used neuron and therefore a constant diameter of 0.5µm was set. The axonal part of the neuron was replaced by the standard axon as described previously. Threshold maps and latency plots were computed for four configurations of the realistic model neuron. Depth of the dendritic tree was varied and started at 0µm, i.e. the dendritic tree was located at the same depth as the soma (Fig. 4.17A). Three additional configurations with dendritic tree depths of 10, 20 and 30µm were also constructed.

All four resulting threshold maps were similar in shape and only varied within a short region between approximately 30-130µm (Fig. 4.17B, top). Whereas the small differences in threshold seemed to be unimportant the latency plot showed interesting details. Latency outside of the region of importance was the same for all four configurations, i.e. was mainly determined by axonal properties, within this region two major patterns could be discriminated. Latency for the two configurations with large dendritic depth was not differing (blue circle in Fig. 4.17B, bottom) and therefore the dendritic portion of the neuron did not (or equally in both configurations) influence spike generation. When the dendritic tree was located closer to the stimulating electrode, however, arbitrary latencies were monitored (red circle in Fig. 4.17B, bottom).

A

B
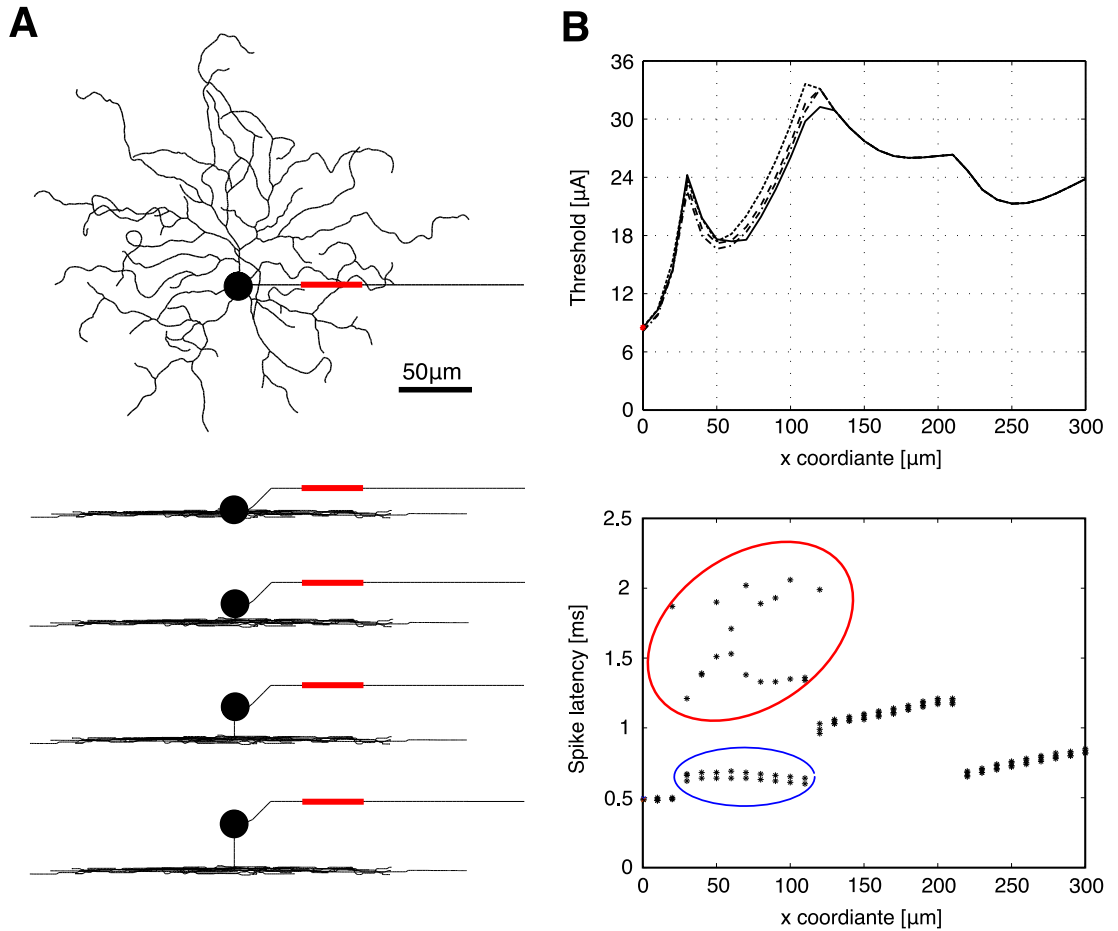
Figure 4.17: **Influence of depth of dendritic tree on SSI -** (A) Top and side view on the model neuron. Four configurations were established, each with a different depth of the dendritic tree. Dendritic morphology was obtained from `www.neuromorpho.org` (data from Kong *et al.* (2005), cell identifier 030501). Dendritic diameter was set to 0.5µm. The AIS is indicated in red. (B) Top: Threshold maps for all four neurons did not exhibit large differences. Only within a 100µm region in the proximal axon minor differences could be examined (30-130µm). Bottom: Spike latency revealed the influence of the dendritic tree on spike initiation. Whereas for the two neurons with dendritic trees closer to the stimulating element latency did not follow a regular pattern (red ellipse). If the primary neurite is longer and therefore the depth of the dendritic portion is increased latency did not change between both configurations (blue ellipse). Thus, a larger distance between electrode and dendritic tree reduced the influence of the dendritic portion on spike generation. Model properties: *Morphology:* traced; *Channels:* $Na_v1.2$, $Na_v1.6$, K, L; *Temp:* 37°; *Pulse:* monophasic 0.1ms; *Potentials:* analytical (ρ_e=0.1S/m).

4.10 Stimulation of dendrites

To examine how GCs respond to direct stimulation of their dendrites stimulation was delivered at five different locations on the previously presented model GC (Kong *et al.* (2005)). Stimulation was applied via a point source electrode at two different electrode-to-fiber distances. In a first investigation the electrode was positioned in close proximity to the neuron (10µm above the closest compartment). Secondly, the electrode was elevated to the default distance during epiretinal stimulation (45µm above the soma). Resulting electrode-to-fiber distance for the four dendritic locations was 55-60µm. Additionally to the four dendritic electrode locations the electrode was positioned at the sweet-spot of epiretinal cathodic stimulation in the distal portion of the AIS. Stimulation was always applied at 101% threshold.

Fig. 4.18A shows the five electrode locations (1-5) and the connections from these points to the soma in red. Distances from the soma were approximately 220, 175, 130, 200 and 85µm for locations 1-5, respectively. When stimulated cathodically spikes were always initiated in compartments directly below the electrode and therefore spike runtime to the soma could be monitored and compared (Fig. 4.18B, top). This comparison was made with two constant dendritic diameters of 0.5 (red) and 1µm (blue). Runtime was shorter for the thicker dendrite and shortest runtime was monitored for axonal spiking at location 5 with the smallest distance betweem site of stimulation and soma. In order to get a more meaningful measurement spike velocity was computed and is shown in Fig. 4.18B (bottom). Within the dendritic portion spike velocity was between 0.1 and 0.15m/s and was approximately constant for both diameters. Axonal spikes, due to higher sodium channel density and thicker fiber diameter (especially in the hillock), resulted in faster spike conduction with values approximately five times higher than in dendrites. Since the dendritic tree had only minor influence on spike generation when stimulation was applied at the AIS runtime was similar for different dendritic diameters. Due to the short distance between the AIS and the soma and coarse temporal resolution, however, spike velocity showed larger differences.
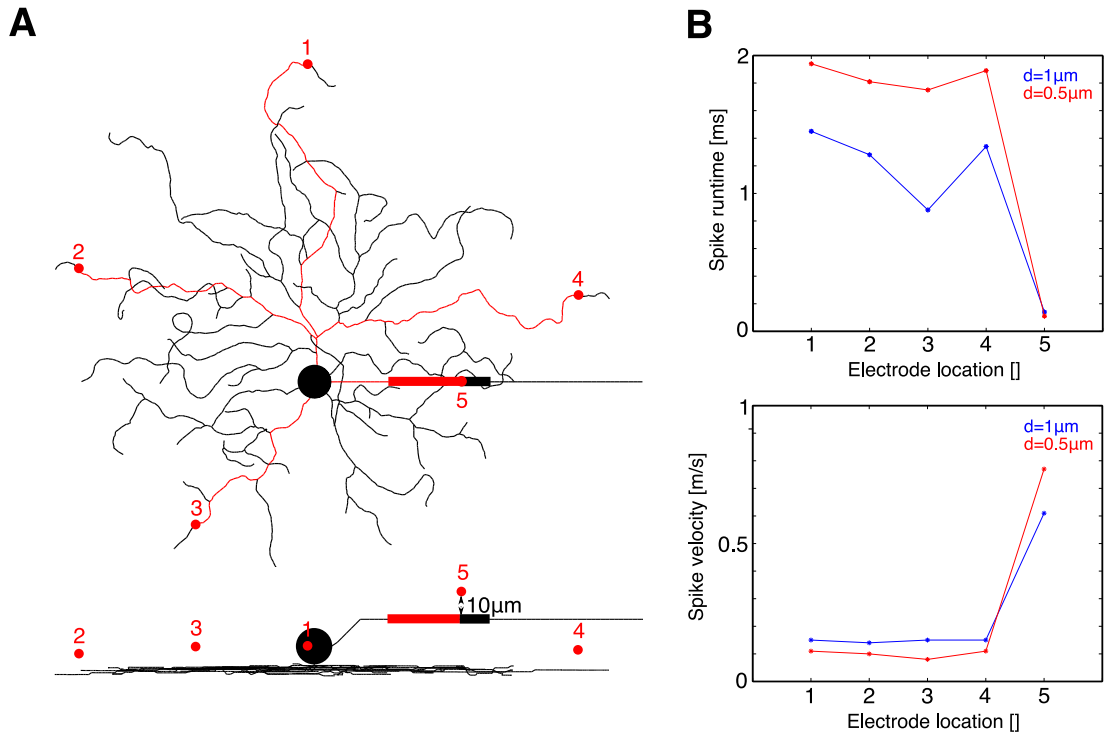
Figure 4.18: **Cathodic stimulation of the dendritic tree at close distance -** (A) A traced GC was stimulated with a point source electrode at five different locations (4x dendrite, 1x AIS). The electrode was positioned 10µm above the closest compartment (bottom). Spikes were always initiated directly below the electrode location. The diameter of the dendritic tree was set to constant values of either 0.5 or 1µm. (B) Spike runtime (top) was monitored and by computing the distance from the SSI to the soma (red traces in (A)) spike velocity (bottom) was calculated for both dendritic diameters. Compared to the larger diameter (blue) a thinner dendrite (red) resulted in longer runtime and slower spike conduction. The mean ratio of spike velocity between the two tested diameters of 1µm and 0.5µm was 1.5006 which is close to the theoretically derived value of 1.4142 ($\sqrt{2}$). Model properties: *Morphology:* traced; *Channels:* $Na_v1.2$, $Na_v1.6$, K, L; *Temp:* 37°; *Pulse:* monophasic 0.1ms; *Potentials:* analytical (ρ_e=0.1S/m).

Stimulation at larger electrode-to-fiber distance changed the excitation processes within the model neuron (Fig. 4.19A). The SSI ①,②,③,④,⑤ was not located directly below the stimulating electrode for all electrode locations any more. The 70 degrees rule of the activating function leads to a larger region which is influenced by stimulation when applied from larger distance. Thus, also neighbored regions within the dendrite were excited during stimulation which led to initiation of spikes at branching points within the dendrite far away from the actual stimulation site (① & ②). When stimulated from locations 3 & 4 AP initiation even changed from the dendrite to the axonal part of the neuron (③ & ④). Only electrode location 5 did not result in different activation characteristics.

Initiation of APs at branching points for locations 1 and 2 within the dendritic tree could be explained by following both paths from these branching points (blue traces in Fig. 4.19A). Site of spike initiation ① and ② was located at branching points which connect branches located close to the stimulating electrode. Regions close to the electrode were depolarized during cathodic stimulation and this depolarization was transferred to the soma via electrotonoc (=axial) currents. At branching points of two (or more) of these branches it is likely that (sub-threshold) depolarizations add up to depolarization levels which are capable to initiate an AP.

By monitoring thresholds for two different dendritic diameters this change in SSI could be observed for four out of five electrode locations (Fig. 4.19B). Whereas thresholds at locations which are influenced by the dendritic diameter (1 & 2) change for a thicker dendrite axonal spiking (4 & 5) did not or only slightly change. Stimulation from location 3, however, resulted in different thresholds for both dendritic diameters although spike initiation was located within the axon. This suggests that the dendritic tree still influenced spike initiation within the axon by axial currents from the dendrite via the soma into the AIS.

Stimulation from electrode location 4 resulted in axonal spiking because the axon was located closer to the stimulating electrode (z direction). Electrode to fiber distance was ∼58µm to location 4 and 55µm to the SSI ④. Thus, axonal compartments close to the SSI were depolarized more than compartments within the dendritic tree and consequently initiated an APs.
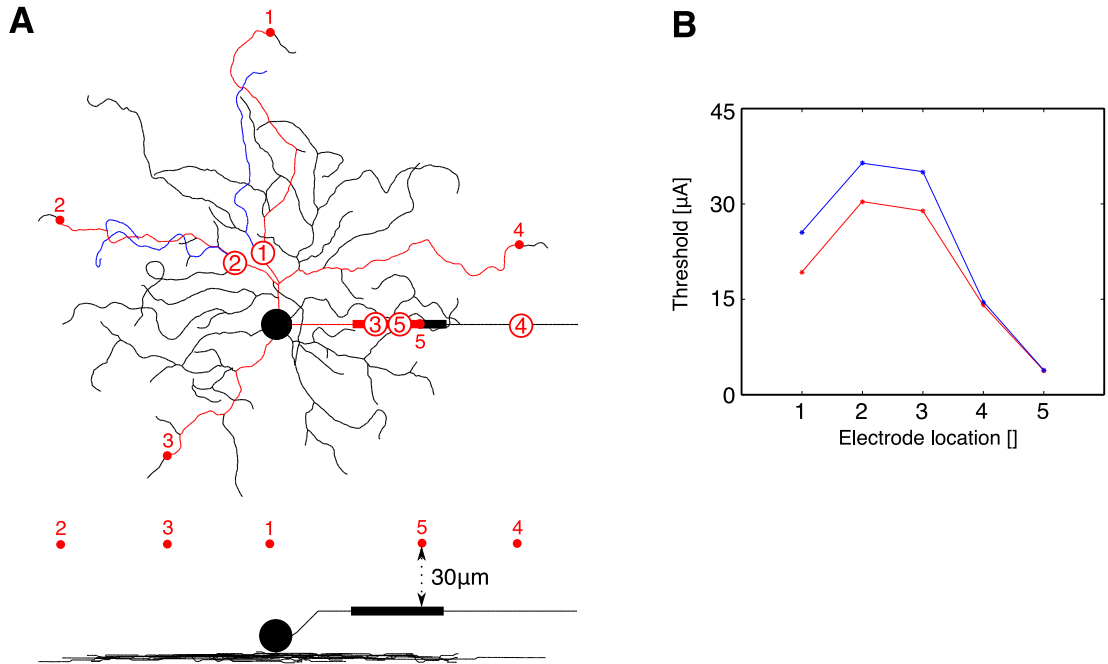
Figure 4.19: **Cathodic stimulation of the dendritic tree at large distance -** (A) Again, stimulation was applied at locations 1-5, however, the electrode was always located in the x-y plane 45µm above the soma (=standard configuration). Due to a larger extent of the activating function (70 degrees rule) larger parts of the dendritic tree were directly influenced by the pulse. Thus, SSI was not located directly below the electrode for all locations. Circles with numbers inside denote the SSI for the corresponding electrode locations. Stimulation from locations 1 and 2 resulted in spiking at branching points within the dendrite (① & ②). Axonal spiking was observed for locations 3-5 (③,④ & ⑤). (B) By monitoring thresholds for the two dendritic diameters the influence of the dendritic tree could also be revealed. Locations 1-3 resulted in different thresholds for thin and thick dendrite but location 4 and 5 showed no difference in threshold which is an indicator for pure axonal spiking. Location 3, however, showed different thresholds although spiking was initiated within the axon which was supported by electrotonic currents from the dendrite. Model properties: *Morphology:* traced; *Channels:* $Na_v1.2$, $Na_v1.6$, K, L; *Temp:* $37°$; *Pulse:* monophasic 0.1ms; *Potentials:* analytical (ρ_e=0.1S/m).

4.11 Biphasic stimulation

So far only monophasic cathodic or anodic pulses were investigated. In actual retinal implants or other neuroprosthetic devices, however, charge balanced pulses have to be applied which do not harm the electrode and the surrounding tissue. Electrochemical processes can lead to severe electrode destruction and more important, to damage of the surrounding nervous tissue. Aside from the necessity of charge balance another interesting fact comes into play. As presented in the previous sections anodic and cathodic pulses have quite different effects on a target fiber. Whereas cathodic pulses predominantly lead to lower thresholds some electrode locations show lower thresholds for anodic stimulation. Thus, the next step is to investigate how cathodic-first and anodic-first biphasic pulses influence threshold.

Interstimulus interval

The applied pulse was either an anodic-first or cathodic-first 0.1ms pulse with different interstimulus intervals (ISIs) ranging from 0-1ms (Fig. 4.20, bottom). Again, by shifting the electrode in a constant distance of 45µm along the x-direction of the axon one-dimensional threshold maps could be drawn (4.20A, B & C). Thresholds between anodic-first and cathodic-first stimulation with no break between the two pulses showed different characteristics than for monophasic stimulation (Fig. 4.20A). Whereas for monophasic cathodic stimulation always locations close to the soma resulted in highest thresholds during biphasic stimulation the transition region between the AIS and the distal axon (250µm) was the location of maximum threshold. With this pulse configuration cathodic-first stimulation had significant lower thresholds than anodic-first stimulation. When the ISI was increased to 0.5ms (Fig. 4.20B) and 1ms (Fig. 4.20C) these differences in thresholds vanished. Especially for a 1ms ISI both stimuli resulted in almost equal threshold traces. Therefore, combined with the similarity with monophasic cathodic threshold maps it turned out that, except for electrode locations close to the soma, the cathodic pulse phase was the dominant mode of fiber activation during biphasic stimulation. Again, also spike latency was examined for different pulses. With an ISI of 1ms it was evaluated that the anodic phase was the spike triggering phase only at location 0µm (soma) and spikes at all other locations along the axon were initiated by the cathodic phase (data not shown).
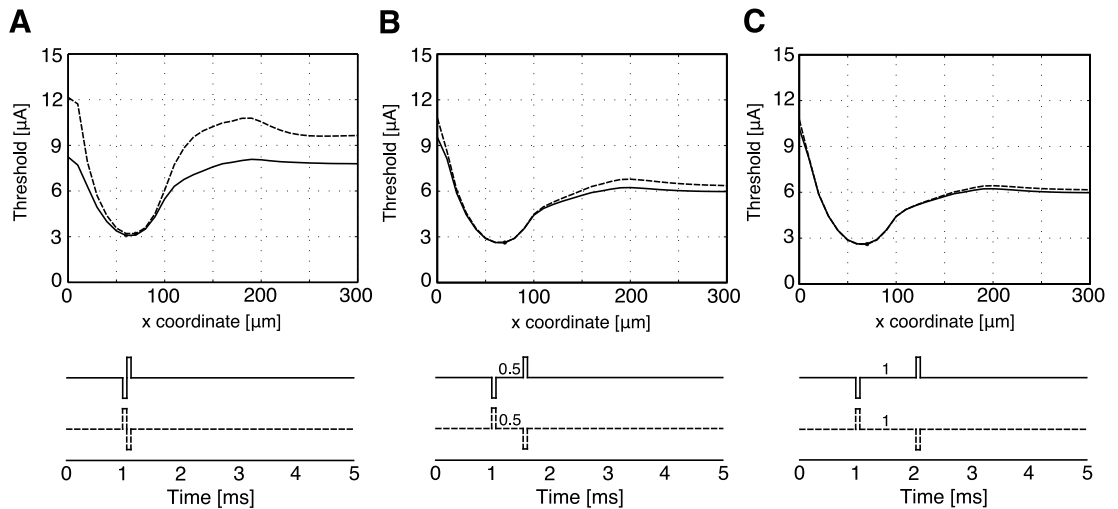
Figure 4.20: **Epiretinal biphasic stimulation with different ISIs -** Stimulus length for both polarities was set to 0.1ms. Solid and dashed traces indicate cathodic-first and anodic-first stimulation, respectively. The electrode was shifted in x direction on the epiretinal side 45µm distant to the soma center (z direction). (A) Both pulses were applied without any interstimulus break. Cathodic-first stimulation results in lower thresholds, however, in the AIS region thresholds are almost equal. Compared to monophasic stimulation the shape of the threshold maps were similar to cathodic stimulation except for lower thresholds for electrode locations close to the soma (compare to Fig. 4.13A). (B) An ISI of 0.5ms lowered thresholds for both stimulus forms. Within the AIS region thresholds were equal. (C) Cathodic-first and anodic-first stimulation resulted in comparable thresholds for an ISI of 1ms. No significant difference in threshold could be observed. The shape of the two threshold maps resembled thresholds from monophasic cathodic stimulation closely. Model properties: *Morphology:* simplified; *Channels:* $Na_v1.2$, $Na_v1.6$, K, L; *Temp:* 37°; *Pulse:* biphasic 0.1ms each phase, varying ISI; *Potentials:* analytical (ρ_e=0.1S/m).

A

B
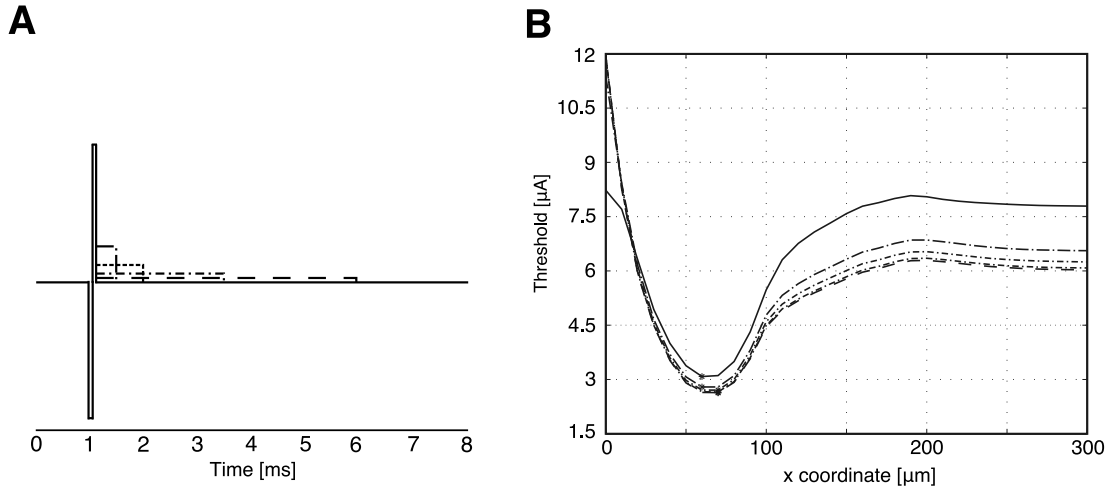
Figure 4.21: **Asymmetric charge balanced pulses and threshold -** (A) Following a 0.1ms cathodic phase balancing pulses with different length were tested. Shortest and longest anodic phase were 0.1 and 4.9ms, respectively. ISI was set to 0ms in all configurations. (B) Resulting threshold maps for pulse configurations in (A). Thresholds became lower for longer balancing pulses. The cathodic lead-phase was always the spike-triggering phase except for the 0.1ms anodic phase at locations close to the soma (see previous section). Model properties: *Morphology:* simplified; *Channels:* $Na_v1.2$, $Na_v1.6$, K, L; *Temp:* 37°; *Pulse:* biphasic 0.1ms cathodic, varying anodic, no ISI; *Potentials:* analytical (ρ_e=0.33S/m).

Asymmetric pulses

The obtained results that the cathodic phase is the dominant phase in spike initiation led to further investigations regarding the length of the anodic balancing pulse. Thus, a 0.1ms cathodic stimulus was followed by varying anodic pulses (Fig. 4.21A). The length of the anodic phase was varied from 0.1ms (standard configuration) up to 4.9ms and amplitude was adjusted in order to generate charge balanced pulses. Thresholds along the main axis of the model neuron were plotted for all pulse configurations (Fig. 4.21B). By extending the anodic phase thresholds decreased and the cathodic phase was triggering spikes also at locations close to the soma which resulted in higher thresholds in this region. The threshold map resulting from stimulation with the longest anodic phase (4.9ms) closely matched monophasic cathodic stimulation.

4.12   Subretinal stimulation

Subretinal stimulation was examined in order to determine if direct stimulation from the subretinal space is a feasible strategy for retinal implants. Again, one-dimensional threshold maps for both, cathodic and anodic stimulation were computed (Fig. 4.22). Additional plots of spike latency allowed to discriminate multiple sites of spike initiation. In contrast to epiretinal stimulation thresholds were higher by almost one order of magnitude. Furthermore, a simple interpretation of the cathodic threshold map as for epiretinal stimulation was not possible.

During cathodic stimulation close to the soma the AIS was the SSI and by further shifting the electrode towards the AIS it changed to compartments within the right trunk of the dendrite (Fig. 4.22.A) The absolute minimum occurred when the electrode was located below the end of the right dendritic portion ($\sim$250µm). Further distal electrode locations still generated spikes at the dendritic edge (constant latency) and axonal spiking was observed for electrode locations more than 410µm distant to the soma.

Higher thresholds were observed during anodic stimulation, especially in far distal regions of the axon. Spike initiation, again, was examined in all parts of the model neuron (AIS, dendrite, axon). Spike latency discriminated three main regions that corresponded to spike origin (Fig. 4.22B, bottom).

Safe stimulation

Threshold and applied charge were explored in order to find out if direct activation of GCs from the subretinal space can be achieved within the safety limits for electrical stimulation. Electrodes with diameters from 10 to 200µm were investigated and threshold current, charge, threshold current density and charge density were monitored (Fig. 4.23). The electrode was always located directly below the soma in a z distance of 100µm. At this location thresholds are not minimal, however, action potentials are initiated in the AIS which makes the investigation independent of dendritic tree morphology.

In comparison to epiretinal stimulation threshold for a 10µm electrode was 10 times higher during subretinal stimulation. Whereas threshold current and charge increase for larger diameters the opposite is true for threshold current density and charge density.
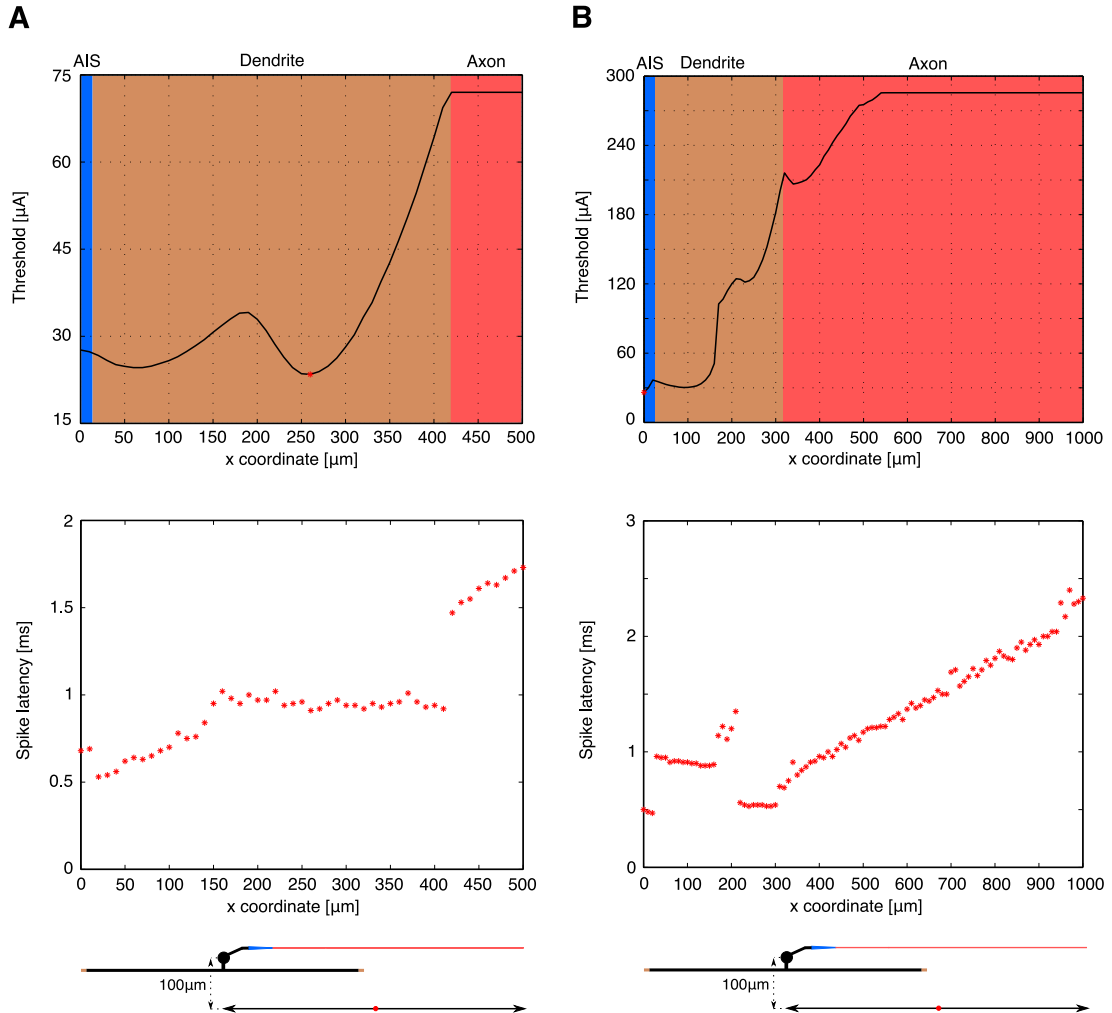
Figure 4.22: **Threshold during subretinal stimulation and SSI -** (A) Again, during cathodic stimulation the SSI changed between AIS, dendrite and axon. Threshold minimum was observed when the electrode was exactly below the dendritic edge (250μm). The latency plot at the bottom reveals the SSI more clearly. Dendritic spikes were not always initiated at the edge of the fiber but also within the dendrite. (B) The threshold map for anodic stimulation did not give a clear hint on SSI. The latency plot, however, discriminated three regions for spike origin. Note that the electrode was shifted much further along the axon during anodic stimulation. Model properties: *Morphology:* simplified; *Channels:* $Na_v1.2$, $Na_v1.6$, K, L; *Temp:* 37°; *Pulse:* monophasic 0.1ms; *Potentials:* analytical (ρ_e=0.1S/m)
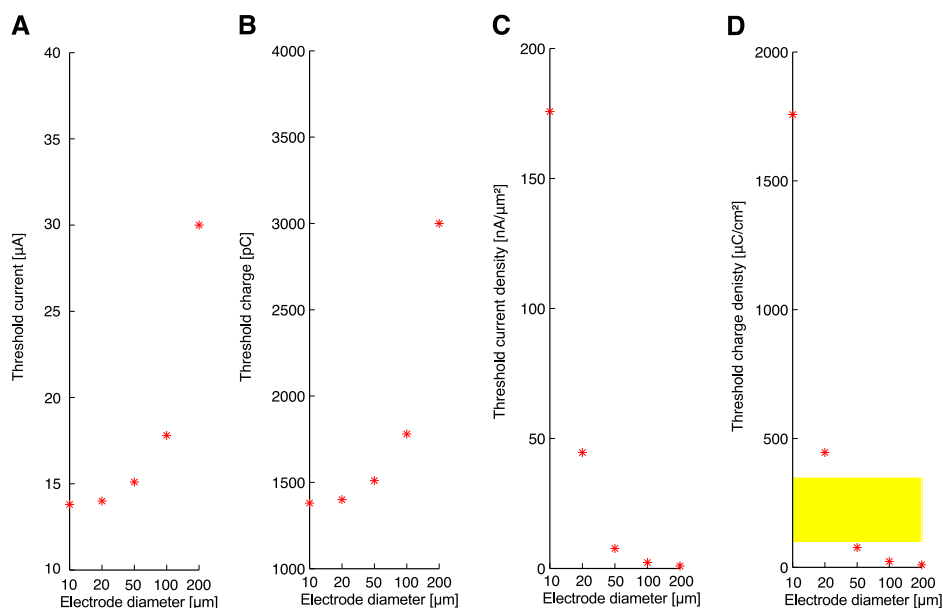
Figure 4.23: **Safety limits during subretinal cathodic stimulation -** (A) Similar to epiretinal stimulation threshold currents increased for larger electrodes. (B) The same held true for injected charge. (C & D) Lower threshold current densities and charge densities were observed during stimulation with larger electrodes. Only electrodes larger than 20µm in diameter were in the safe range for electrical stimulation (limits 100-350µC/cm^2 in yellow, Brummer & Turner (1977); Rose & Robblee (1990)). Model properties: *Morphology:* simplified; *Channels:* Na$_v$1.2, Na$_v$1.6, K, L; *Temp:* 37°; *Pulse:* monophasic 0.1ms; *Potentials:* FEM (ρ_e=0.1S/m)

Safe stimulation was only achieved when electrodes were larger than 20µm (Fig. 4.23D). This is also in agreement with results from an experimental study which stated that used 25µm electrodes were close to, or over, the safety limit (Tsai *et al.* (2009)).

4.13 Comparison with experimental results

Epiretinal stimulation

Thresholds determined with the simplified standard model were also compared to actual experimental thresholds measured in rabbit and rodent retina. While simulated thresholds were shown to fit one experimental study using rodents quite closely (Sekirnjak *et al.* (2006), Fig. 4.10) now more experimental data was gathered for comparison. Jensen and coworkers (2003) measured thresholds in isolated rabbit retina during epiretinal stimulation with a micro-electrode. The cone-shaped electrode had a height

of 5µm and a diameter of 2µm which results in a surface area comparable to a disc electrode 4.5µm in diameter ($16.02µm^2$ vs. $15.9µm^2$). Therefore, a 4.5µm disc electrode was used to compare experimental and simulated results. Median minimum axonal thresholds (>1.5mm distant from the soma) in experiments were reported to be 0.94µA and 6.5µA for cathodic and anodic stimuli whereas computed thresholds were 3 (cathodic) and 13.5µA (anodic).

In a follow-up study Jensen and colleagues again examined thresholds during epiretinal stimulation in rabbit retina, however, they used relatively large micro-electrodes (Jensen *et al.* (2005). Two laterally insulated wires with diameters of 125 and 500µm were employed as stimulating elements. Measured thresholds at the distal axon were in the range of 3.5-29µA and again simulations resulted in higher thresholds. Maximum (anodic) threshold for axonal stimulation with the 500µm electrode was approximately 100µA in simulation. All together, simulated threshold characteristics (strength-duration curves, data not shown) were comparable to experimental results obtained with large electrodes, however, modeled results were higher than experimental thresholds by a factor of ∼3. This difference vanished if a retinal conductivity of $3*10^3\Omega$cm (standard $10^3\Omega$cm) was used.

Temperature was maintained at 34-36° Celsius in both experimental studies which is in the range of the simulation temperature of 37°. Pulse length was 0.1ms in experiments and simulations and only monophasic anodic or cathodic pulses were tested. Comparison of both studies with simulations can be found in table 4.2.

More recently, activation thresholds for epiretinal stimulation were also reported by several other studies (e.g. Boinagrov *et al.* (2014); Cho *et al.* (2012); Eickenscheidt *et al.* (2012); Fried *et al.* (2009); Hadjinicolaou *et al.* (2015); Tsai *et al.* (2012)). Depending on pulse polarity (cathodic, anodic), pulse configuration (monophasic, biphasic), electrode-to-fiber distance, temperature and electrode shape and size thresholds mostly were in the range of a few up to tens of microamperes (except for very large electrodes with higher amplitudes, e.g. Hadjinicolaou *et al.* (2015)).

Subretinal stimulation

Thresholds during subretinal stimulation of the retinal network are more complicated to interpret than cathodic responses. Due to the fact that the electrode-to-fiber distance is much larger (∼100µm) than for epiretinal stimulation activation characteristics become

| | Jensen et al 2003 | | | Jensen et al 2005 | | | |
| | cone & d=4.5µm | | | d=125µm | | d=500µm | |
	c	a		c	a	c	a
Experiment	0.94	6.5		3.5	9	13	29
Simulation	3	13.5		10.6	29.6	41.5	96.2

Table 4.2: **Comparison of experimental and simulated thresholds during epiretinal stimulation -** A 4.5µm electrode was used to compare thresholds to results from Jensen *et al.* (2003). Minimum thresholds at the axon were compared during cathodic (c) and anodic (a) stimulation with a micro-electrode. Thresholds for larger electrodes (125 and 500µm) were compared with results from Jensen and coworkers (2005). All thresholds are given in µA. Model properties for all comparisons: *Morphology:* simplified; *Channels:* $Na_v1.2$, $Na_v1.6$, K, L; *Temp:* 37°; *Pulse:* monophasic 0.1ms; *Potentials:* FEM (ρ_e=0.1S/m).

more complex. Furthermore, during stimulation from the subretinal space it is more likely to also activate secondary neurons in the retina and therefore indirectly activate GCs by synaptic input from ACs and BCs. Several studies investigated the possibility of GC activation from the subretinal space (e.g. Boinagrov *et al.* (2014); Eickenscheidt *et al.* (2012); Jensen & Rizzo (2006, 2008); Lee *et al.* (2013); Tsai *et al.* (2009)). Most of these studies examined at least two spike trains separated in time which arise from direct and indirect activation. Primary (direct) spikes with latencies of <2-3ms were considered as direct spikes from GCs without support of synaptic inputs. Thresholds from one study match simulated thresholds best (Tsai *et al.* (2009), 25µm disc electrode, biphasic 0.1ms pulses, cathodic-first). Median threshold for primary spikes in rabbit GCs was approximately 70µA which is in a comparable range with simulated somatic and axonal thresholds (46 and 68µA).

Another study, however, reported thresholds in contradiction to the presented simulated results. Boinagrov and coworkers (2014) reported that direct activation thresholds for anodic pulses are lower than for cathodic stimuli (4 vs. 23µA) whereas simulated thresholds were always lower when stimulation was applied cathodically (see also Fig. 4.22).

4.14 Discussion

The presented results describe multiple activation characteristics in retinal ganglion cells during extracellular stimulation. Two different types of sodium channels along the AIS were incorporated as suggested by previous studies (Boiko *et al.* (2003); Van Wart *et al.* (2007)). Crucial geometric properties of GCs were investigated to derive a simplified model neuron with the same characteristics as actual GC morphologies during epiretinal stimulation. In addition to computation of extracellular potentials with an analytical solution also stimulation with disc electrodes in various size was simulated by using the method of finite elements. Additionally, focal stimulation of a group of GCs without co-activate passing GC axons was exploited. Thresholds were also examined with regards to safety limits for electrical stimulation. Furthermore, the influence of the dendritic tree on spike generation during sub- and epiretinal for both, anodic and cathodic stimulation, was investigated. Biphasic stimulation and its consequences on threshold and SSI was determined. Finally, thresholds for a range of differently sized disc electrodes were compared to actual experimental results.

The key finding of this study was that focal activation of a small group of closely packed GCs without initiating spikes in passing axons is generally possible. Another important finding was that the dendritic portion of GCs had major influence on spike generation during stimulation, even when stimulation was applied from the epiretinal space. The SSI within the dendritic tree is heavily influenced by electrode-to-fiber distance. Cathodic stimulation generally results in lower thresholds than anodic stimulation, however, under certain circumstances as can be seen in Fig. 4.16 anodic stimulation can be the preferred pulse polarity.

Sodium channels and AIS threshold

Spike initiation in neurons is mainly determined by the activating function and by the distribution of voltage-gated ion channel along the membrane. Sodium channels enable spike generation during extracellular stimulation due to their dominant role during the upstroke of an AP. Up to date, nine distinct types of sodium channels are known in mammals ($Na_v1.1$-$Na_v1.9$, Goldin *et al.* (2000)). Generally, the distinct distribution of two types of sodium channels along the AIS is suggested to be crucial for spike initiation and back-propagation into the soma. Hu and coworkers (2009b) conducted an elegant

experimental and computational study to reveal these mechanisms in cortical pyramidal neurons.

Along the unmyelinated portion of GCs two types of sodium channels are dominant. Boiko and coworkers (2003) reported $Na_v1.2$ to be present in major parts of GCs whereas $Na_v1.6$ channels were shown to occupy only the distal portion of the AIS. In a more recent article from the same group, however, $Na_v1.1$ was reported to be also present in GCs (Van Wart *et al.* (2007)). An available model of $Na_v1.2$ channels, however, was chosen for simulations since no or only limited models (Spampanato *et al.* (2004)) for $Na_v1.1$ were available. Both channels have similar activation and inactivation characteristics, however, data from a previous study suggests activation and inactivation (steady-state) at slightly higher membrane voltages in $Na_v1.1$ (Spampanato *et al.* (2003)). The most important feature of sodium channels within the AIS is that the distal portion is occupied by low-threshold channels ($Na_v1.6$) whereas the proximal AIS exhibits high threshold ($Na_v1.1$ or $Na_v1.2$) channels.

Previous studies reported that thresholds during extracellular cathodic stimulation along GCs show a minimum region which is aligned with the band of highly dense sodium channels in the AIS (Fried *et al.* (2009)). So far, computational studies used membrane models which only incorporated a single type of ion channel (Jeng *et al.* (2011); Werginz *et al.* (2014)). Thus, the major reason for incorporating a specific distribution of two types of ion channels was to see differences to previous studies.

In the presented study threshold characteristics, including a low-threshold region aligned with a high density of sodium channels ($Na_v1.2$ and $Na_v1.6$), were similar to former results. As reported by Jeng and coworkers (2011) lowest threshold was located within the distal part of the AIS. Same results were shown in this study, however, lowest threshold is even more distal because of the accumulation of low-threshold sodium channels within the distal AIS. Aside from this distribution two major geometric properties shape this effect: i) a diameter increase at the soma which acts as a current sink is closer to the proximal AIS and ii) the tapered geometry of the AIS with a connected thin axonal segment.

Dendritic morphology and spike initiation

So far, dendritic influence on AP generation during extracellular stimulation was only investigated in non-retinal neurons (e.g. Rattay & Wenger (2010)). Additionally, mul-

tiple studies revealed electrophysiological properties along the dendritic membrane, however, without investigating the response to extracellular stimulation (e.g. Margolis *et al.* (2010)). Therefore, stronger emphasis was laid on investigations of dendritic response during electrical stimulation and the presented results suggest that activation of the dendritic tree can also influence SSI in GCs.

Electrode-to-fiber distance is the most important factor influencing threshold and similarly the distance between the dendritic tree and the electrode mainly determines its impact on spike generation. During stimulation of GCs the primary neurite, i.e. the first portion of the dendritic tree closest to the soma, is the main factor determining electrode-to-fiber distance. The influence of the depth of the dendritic tree is different for sub- and epiretinal stimulation. Whereas during epiretinal stimulation a longer primary neurite results in a larger distance between the electrode and the dendritic tree the opposite is true for subretinal stimulation.

On morphological basis, ON and OFF GCs can be discriminated by the depth of their dendritic trees. ON GCs connect to longer ON BCs and therefore do not intrude deep into the IPL. OFF GCs, on the other hand, must have contacts down to the terminals of shorter OFF BCs within the outer portion of the IPL. Thus, the following situation arises: During epiretinal stimulation the dendritic tree of ON GCs is more likely to participate in AP generation than dendritic processes of OFF GCs. Contrary, the dendritic tree of OFF GCs is assumed to have a stronger influence on direct activation during subretinal stimulation.

The dendritic tree not only directly influences spiking in GCs by being the SSI but also contributes to activation with depolarizing electrotonic currents into the soma and proximal parts of the axon. Depolarizing axial currents from more than one location along the cell membrane propagate along the fiber and branching points (which aggregate these currents) are candidates for AP generation. This leads to a surprising conclusion: Under certain circumstances not parts of the neuron which are depolarized most become SSI but electrotonic currents along the fiber shift SSI to other cell regions.

Up to date retinal implants mostly employ flat disc electrodes at either the inner or outer surface of the retina. Other electrode configurations with penetrating stimulating elements to achieve closer electrode-to-fiber distance were proposed in the past, however, mostly for the subretinal appraoch (e.g. Butterwick *et al.* (2009); Khraiche *et al.* (2011); Mathieson *et al.* (2012); Palanker *et al.* (2005)). The approach of using

penetrating electrodes in epiretinal implants was proposed too (Ganesan *et al.* (2010)). Therefore, the results from a near-field stimulation of GC dendrites (Fig. 4.18) can also be of high importance for future stimulating strategies in implants.

Noise and spiking

Adding a noisy transmembrane current component allowed to compute spiking probability as a function of stimulus amplitude resulting in sigmoid response curves similar to experimental determined data (see Fried *et al.* (2009); Sekirnjak *et al.* (2008); Tsai *et al.* (2009)). The noise term was presented previously and was only depended on a noise factor k (Rattay *et al.* (2001)). During a stepwise increase of stimulus amplitude the spike response was monitored and afterwards this data was fitted with a sigmoid function (Boltzmann equation). Fitted plots (recruitment curves) resembled experimental data quite well. Spiking probability increases from minimum (no AP) to maximum (each pulse elicits an AP) in the range of ∼50-150% of threshold amplitude current in experiments (Fried *et al.* (2009); Sekirnjak *et al.* (2008); Tsai *et al.* (2009)). By varying the noise factor k it was possible to adjust simulated results to experimental data. Higher values of k led to a broader course between no spiking and 100% spiking whereas low values of k resulted in response curves which almost jump from 0 to 100% spiking within one amplitude step. Results were compared to data from a study which stimulated GCs subretinally (Tsai *et al.* (2009)) and thus response curves might look different than during epiretinal stimulation. Unfortunately, no detailed data from other studies which investigated eprietinal stimulation were available, however, the shape of fitted response curves was similar in all studies.

There is strong evidence for an increased spiking activity (in the range of 10Hz) in GCs due to photoreceptor loss (Dräger & Hubel (1978); Stasheff (2008); Thyagarajan *et al.* (2010)). The origin for this hyperactivity, however, is not well understood so far. A study by Margolis and Detwilder (2011) showed that spontaneous activity in rd1 mice was present as long as glutamatergic inputs from BCs were present. By applying chemical agents to block synaptic inputs the spontaneous spike rate, however, diminished. The same group also reported that GCs exhibited stable electrophysiological responses during long term (36-210 days) observations (Margolis *et al.* (2008)).

In the presented simulations spontaneous spiking occurs at higher values of k than necessary for computing similar results (i.e. recruitment curves) to fit experimental

data. Therefore, together with data from experimental studies simulations with noise suggest that rhythmic activity in the degenerated retina is not initiated by intrinsic properties of GCs but is clearly associated with excitatory synaptic inputs. However, a relatively high level of noise close to the border of spontaneous activity might be present in GCs. Thus, a small disturbance of GC membrane kinetics can lead to random spontaneous spiking as observed in experiments.

Focal stimulation

One great challenge for current epiretinal prostheses is to achieve focal activation of GCs close to the stimulating electrode without activating APs in passing axons. This is also suggested to be the main reason for deformed percepts in clinical trials (Nanduri *et al.* (2012)). Therefore, the possibility and extent of focal stimulation was explored. Comparing lowest threshold within the AIS and threshold of a passing axon resulted in an operating window from 1.44 to 3.18µA for a 20µm disc electrode (z=45µm). By using stimulus amplitudes in this selective operating range co-activation of the passing axons is avoided and only a small group of GCs will be activated. It was shown (see Fig. 4.9) that a group of approximately 18 GCs had thresholds lower than the passing axon. By varying the axonal diameter of the passing axon the number of GC which can be focally activated also changed. Thus, depending on several parameters such as package density of GCs, diameter of passing axons and sodium channel density in the AIS the size and shape of the region which can be activated individually is highly variable.

Safety limits during electrical stimulation

Safe electrical stimulation of the retina is a precondition for developing more efficient retinal implants and avoidance of irreversible electro-chemical processes. Two main mechanisms for charge transfer from an electrode to the surrounding media can be distinguished: i) non-faradaic or capacitive reactions that redistribute charged molecules in the surrounding media and ii) faradaic processes which lead to electron transfer between the two media. While the first of these two mechanisms leads to reversible processes the latter one can result in irreversible reaction due to reduction and oxidation (redox) processes. For an extended review on the electrode-tissue interface and safe application of electrical stimulation see Merrill *et al.* (2005).

4. PART II: GANGLION CELL STIMULATION

Avoidance of irreversible processes damaging neural tissue and the electrode have to be considered when implanting an electrically-driven neurostimulator in humans. Reducing thresholds is one of the key factors for the improvement of future retinal implants. The aim is to have a high number of individually controllable stimulating elements which are positioned in a short and almost constant distance to retina. If future flexible micro-electrode arrays can be implanted in close proximity to their target neurons to provide such a small and constant distance several positive effects would become visible: i) threshold for each electrode would be constantly low; ii) electric cross-talk during simultaneous activation of neighbored electrodes would be minimized and iii) stimulation would be within the safety limit.

Most important for safe stimulation is the so-called charge storage capacity (CSC). CSC describes the amount of charge which can be transferred via an electrode without inducing irreversible reactions on electrode and tissue (faradaic reaction). CSC is a property of the used electrode material and varies strongly across elements and alloys. Platinum and platinum-iridium as standard materials for electrodes used *in-vitro* (e.g. Fried *et al.* (2009); Sekirnjak *et al.* (2006)) and *in-vivo* (e.g. Ayton *et al.* (2014); Stronks & Dagnelie (2014)) in retinal electrical stimulation have a CSC in the range of 100-350µC/cm^2 (Brummer & Turner (1977); Rose & Robblee (1990)). Activated iridium-oxide, on the other hand, has a CSC up to 3900µC/cm^2 under certain circumstances (Cogan *et al.* (2005)). Especially implant designs which are in a relatively large distance to the target fibers and consequent higher stimulating thresholds would benefit from such electrodes. A recent study explored the feasibility of iridium-oxide coated electrodes (bullet-shaped) *in-vitro* and *in-vivo* and determined a 4 times higher CSC in iridium-oxide coated electrodes in contrast to platinum electrodes (Noda *et al.* (2014)). Many more materials for electrodes in neurostimulators are currently under investigation, however, most of them are still lacking proof to also be biocompatible when implanted on a long-term basis.

Another way to increase maximum charge which can safely be applied on an electrode is to increase its surface. Due to fabrication processes surface texture can be made rougher and therefore the actual electrode surface increases. During electro-plating of platinum electrode, for example, the surface of electrodes forms a granular structure which enlarges the real surface area by factors up to 100 (Kim & Oh (1996); Mathieson *et al.* (2004)). More recently, so-called nano-cluster platinum electrodes were

also shown to have a highly increased surface and consequent higher CSC (Shah *et al.* (2013)).

Another approach to avoid electro-chemical reactions during electrical stimulation is to stimulate neural tissue with capacitive currents only (Schoen & Fromherz (2008)). Possible modulation of membrane potential by stimulation with an electrode coated by titanium dioxide was shown. By coating the electrode no electrons are transferred and consequently no redox reactions occur. In a more recent study also the feasibility of retinal stimulation was explored (Eickenscheidt *et al.* (2012)). Thereby, capacitive stimulation resulted in spike trains in both, sub- and epiretinal stimulation.

In sum, by placing stimulating elements close to neuronal targets safety limits for electrical stimulation can also be respected with small (<20µm) electrodes with epiretinal implants. Higher charge densities due to smaller electrode size can be compensated with i) new electrode materials having higher CSC, ii) increased real electrode surface due to surface processing or iii) by employing capacitive stimulation to avoid electrochemical reactions.

Point source vs. disc electrodes

The specific activation characteristics of point source and disc electrodes variable in size were investigated. This rather theoretical examination revealed a surprising effect during stimulation of a simple stick model with large disc electrodes. Stimulation with a point source or small ball electrode always led to spiking right below the electrode for cathodic stimulation (as predicted by the activating function (Rattay (1986))). Disc electrodes, on the other hand, showed large activating functions at their edges and therefore these locations were supposed to be the SSI. However, stimulation at threshold led to spikes which again originated from compartments below the electrode center. The explanation for this effect was that electrotonic currents flowed along the fiber in axial direction and when these depolarizing currents from both electrode edges met at the midpoint of the electrode two sub-threshold depolarizations became one supra-threshold activation. By stimulating the fiber at supra-threshold amplitudes the SSI was shifted towards the electrode edges. However, the amplitude when this shift occurred was depending on the size of the stimulating electrode, i.e. the distance between fiber edges and midpoint. With a small electrode (d=50µm) it was necessary to increase threshold amplitude by 10% in order to shift spike initiation to electrode edges

whereas for a large electrode (d=200µm) stimulation above 101% threshold resulted in two spikes. Aside from electrode size this characteristic is mainly determined by the intracellular (axial) resistivity (ρ_i). Higher values of ρ_i hinder axial currents to spread out in axial direction and therefore a more local activation can be assumed. Contrary, small ρ_i lets electrotonic currents propagate along the fiber fast and therefore facilitates spike initiation at locations far from the actual site of stimulation. In the present study ρ_i was fixed to a value of 130Ωcm which is in close agreement with a previous study in GCs (Fohlmeister *et al.* (2010)).

Biphasic stimulation

In order to obtain insights into stimulation with more realistic pulse paradigms also biphasic stimulation was examined. Therefore, the influence of the interstimulus interval and length of the balancing anodic phase was investigated. Similar as reported in experimental studies (Ahn *et al.* (2015); Hadjinicolaou *et al.* (2015)) also simulated cathodic-first stimulation resulted in lower threshold in contrast to anodic-first stimulation. Furthermore, pseudo-monophasic (i.e. long balancing pulses with low amplitudes) stimulation led to similar threshold maps as monophasic cathodic stimulation.

In epiretinal implants one approach to generate interpretable signals for the brain is to generate APs at high frequencies in a controlled manner. Experimental studies showed that it is possible to reliably elicit APs at frequencies up to 600Hz, depending on GC type (Ahuja *et al.* (2008); Cai *et al.* (2011); Fried *et al.* (2006); Twyford *et al.* (2014)). Pseudo-monophasic stimulation, however, limits the maximum frequency of stimulation.

Experiments vs. modeling

A comparison of experimental and modeling results must be carried out carefully since multiple unknowns are hidden in experimental data. Variations in obtained data can have multiple reasons such as variations in electric components of the experimental setup, placement of the stimulating electrode (e.g. electrode-to-fiber distance and geometric position), variations in the extracted retinal preparations etc. Computer simulations, on the other hand, struggle with many unknown input parameters such as exact distribution of ion channels, intracellular resistance, membrane capacitance and further more. The resistivity of the retina, however, turned out to be the most crucial

parameter when simulated thresholds are compared to experimental data. Reported values for retinal resistivity in different species vary by more than two orders of magnitude (Werginz *et al.* (2015) from Greenberg *et al.* (1999); Karwoski *et al.* (1985); Kasi *et al.* (2011a)).

This study assumed the retina to be electrically homogeneous and its resistivity was set to a value in the medium range of previously reported values (1000Ωcm). During current stimulation, i.e. application of a current density on the electrode surface, the electric resistivity strongly influences the generated electric field. A higher electric resistivity results in higher electric potentials (Ohm's law) and consequently in lower stimulating thresholds. The presented comparison of simulated data with different electrode sizes and experimental data from Jensen and coworkers (Table 4.2, Jensen & Rizzo (2006); Jensen *et al.* (2003, 2005)) showed that computed thresholds differed quantitatively from experimental data, however, were in qualitative agreement. A previous computational study (Werginz *et al.* (2014)) showed that using highest reported values for retinal resistivity (5050Ωcm, Karwoski *et al.* (1985)) resulted in closely matching thresholds as determined in experiments (data from Fried *et al.* (2009)). In the current study a value of approximately 3000Ωcm led to modeled threshold sin close agreement to measured data (data not shown).

Direct GC activation during subretinal stimulation

Subretinal and suprachoroidal implants are located at the outer portion of the retina and primarily stimulate BCs. The approach of direct GC stimulation was also investigated in experiments and it was found to be generally possible (Boinagrov *et al.* (2014); Eickenscheidt *et al.* (2012); Jensen & Rizzo (2006); Tsai *et al.* (2009)). Direct spikes elicited by stimulation from the subretinal space, however, were always associated with indirect spikes with larger latencies, These spiking is generated by the underlying network and it is not quite clear how these medium and long latency spikes influence visual perceptions in clinical trials. Furthermore, a larger electrode-to-fiber distance compared to epiretinal stimulation leads to higher threshold currents for direct stimulation and consequently higher charge densities. As reported previously (Tsai *et al.* (2009)) and confirmed in the current study stimulation with electrodes smaller than 20-30µm exceeds the limit for safe stimulation. In consequence, due to larger stimulating elements resolution and thus visual acuity is not supposed to be as high as during

direct epiretinal stimulation. Furthermore, an increased spread of current due to larger electrodes and electrode-to-fiber distance increases the possibility of electric cross-talk in concurrent stimulation with multiple electrodes in close distance.

Additional aspects / limitations

Several additional questions arose in the course of this study, mostly regarding modeling assumptions and computational simplifications. A simulation study is never capable to cover all potential aspects of actual biological processes. However, it was shown in the past that multiple phenomena and characteristics could been revealed, especially in the field of extracellular electrical stimulation.

Generally, electrophysiologists thinking consists of biological problems such as experimental setup or the design of new experiments. Most of the time experimenters are limited in their studies by physical borders and variations in living tissue. Modelers, on the other hand, don't have to worry about the feasibility of certain experiments and their experimental setup but simply adjust their parameters and compute possible solutions for novel problems. These rather simple approach, however, also has some drawbacks. Many unknowns in the parameters used in models and negligence of important biological or electrical principles may lead to results not even close to actual physiological processes. More complicated models lead to a large number of unknowns, therefore, this section discusses possible misperceptions and their impact on presented results.

Ion channel equipment

Aside from morphological specifications the distribution of ion channels along the neural cell membrane is decisive for spike initiation and signal transmission along a neuron. For GCs, Fohlmeister and coworkers developed accurate ion channel models for various species over the last 25 years (Fohlmeister & Miller (1997); Fohlmeister *et al.* (1990, 2010)). In their last publication a model for cat and rat GCs was introduced which is able to resemble physiologic responses over a wide range of temperature (Fohlmeister *et al.* (2010)). Fohlmeister models were used in multiple previous publications (e.g. Jeng *et al.* (2011); Tsai *et al.* (2012); Werginz *et al.* (2014)) and proved to described actual physiological behavior well. The main reason for not using the original Fohlmeister model in this thesis was a lack of different types of sodium channels in its description.

Focus was laid on the possible impact of $Na_v 1.2$ and $Na_v 1.6$ channels on spike generation during extracellular stimulation. Therefore, a previously published model of the neuronal membrane of pyramidal cells in the prefrontal cortex (Hu *et al.* (2009b)) was adapted to a simplified description of GC membranes. A comparison of thresholds during epiretinal stimulation showed lower thresholds for the Fohlmeister model, however, activation characteristics and site of spike initiation did not vary. Therefore, presented thresholds might be lowered by adjusting ion channel densities along the membrane.

Retina model

The computation of electric potentials within the retina was performed by two different approaches. With a simple analytical solution electric potentials generated by a point source electrode can be calculated. For more complex electrode designs and inhomogeneities of different portions of the retina the more complex numeric method of finite elements was employed.

Whereas the analytical solution is easy to implement and potentials are fast to compute it also has certain drawbacks. Most importantly, a perfect point source generates a totally different electric field as disc electrodes used in neuroprostheses. Furthermore, the retina and its surrounding tissue are not electrically homogeneous which also changes the electric field. Nevertheless, multiple activation characteristics can generally be explained with a point source electrode.

With the finite element model it is feasible to compute generated potentials by complex shaped electrodes within a more natural model of the retina. However, also more (unknown?) parameters have to specified which is associated with a higher chance for distortion of the results.

The most important issue in the presented FEM model is the homogeneous and isotropic specification of the retinal volume. The retina actually consists of multiple cell types with a myriad of connections and distinct layers. Thus, it is improbable that the retina is electrically isotropic in its entirety. It is more likely that electric currents draw random trails through retinal tissue along the path of lowest resistance. The resulting anisotropy, however, is difficult to capture and so far no satisfying approach was introduced. Recently, more complex models as described in the literature also take the distinct layers in the retina (Werginz *et al.* (2014)) or capacitive effects (Minnikanti *et al.* (2010)) into account. Furthermore, Kasi thoroughly investigated factors affecting

the performance of retinal prostheses using a FEM model (Kasi (2011)). In the course of this study Kasi and coworkers also presented an experimental method to measure the resistive properties of retinal tissue (Kasi *et al.* (2011b)). Following their measurements an increasing resistance profile was used in their computations (from 200 (inner retina) to 3500Ωcm (outer retina)) which covers the fixed value of 1000Ωcm in this thesis.

Chapter 5

Conclusions

In summary, this thesis presents a computational framework capable of calculating the response of two types of retinal neurons during extracellular electrical stimulation. The two-step approach combines the computation of an electric field generated by stimulating elements at either the sub- or epiretinal side of the retina with multi-compartment models of either simplified model neurons or traced morphologies.

5.1   Novelty of results

Bipolar cell stimulation

The analysis of synaptic release at BC terminals during subretinal stimulation revealed the crucial mechanism of reversed calcium currents. By utilizing multi-compartment models and a simple mechanism for synaptic exocytosis it was shown that the activation of the retinal network is strongly influenced by the kinetics of calcium channels in BC terminals. Synaptic release does not monotonically increase with stimulus amplitude but the exocytosis patterns depend on pool states, time constants and the current reversal phenomenon. More quantitative data on calcium channel types and their presence in the $\geqslant 10$ groups of BCs is needed to predict the impact of current reversal phenomena such as the center-surround effect on visual sensations elicited by electrical stimulation of the retina. Aside from affecting restoration of vision with (sub)retinal implants the calcium current reversal mechanism is also expected to strongly influence synaptic activity during the usage of other neuroprosthetic devices such as stimulators in the cortex.

Ganglion cell stimulation

Thorough investigation of spike initiation in GCs during sub- and epiretinal stimulation with different pulse polarities led to several novel and interesting findings. It was shown that a realistic model of the axonal portion of a GC is sufficient to compute its response during epiretinal cathodic stimulation. This thesis was the first study to investigate the influence of two types of sodium channels along the proximal portion if GC axons during extracellular electrical stimulation. Additionally, a first computational investigation regarding the influence of membrane fluctuations in spiking probability was in close agreement to experimental studies. Rather surprising activation characteristics involving the dendritic portion of GCs, especially during sub- and intra-retinal stimulation, were explored too. Also these results not only affect electrical stimulation of retinal tissue but can also have impact on stimulation of other parts of the human body. Especially stimulation in close distance to a high number of target neurons like in cortex stimulation might be affected by the presented mechanisms.

5.2 Outlook

The development of new methods and models in order to describe the behavior of the electrically stimulated retina is in constant movement. Pioneering studies in this field by Greenberg (1999) and Resatz (2005) have paved the way for a wide variety of novel modeling approaches and also the presented thesis follows their footsteps.

A key factor for a better understanding of stimulation of the retina will be the integration of computational models in experimental work and vice versa. The design and execution of combined physiological and computational research can add value to this understanding.

Regarding the presented framework and results future simulations should incorporate multiple additional aspects. First, the extension from simple single-electrode stimulation to stimulation with (modeled) multi-electrode array will be of interest and first steps were made in the past (e.g. Benav (2012); Khalili Moghadam *et al.* (2011); Wilke *et al.* (2011)). Thereby, deeper knowledge of how multiple (sequentially or concurrently) working stimulating elements influence the activation and signal transmission in the retina will be obtained. Especially studies of electric properties of the retina in combination with realistic models of electrode arrays seem to be perfectly suited for

simulation studies. Second, modeling of the retinal circuitry with multi-compartment models now became realizable, even without having access to high-performance computing clusters. In the past already models of the retinal circuitry were established (e.g. Sağlam *et al.* (2009); Teeters *et al.* (1997)), however, these models simulate the healthy and not the degenerated retina and are also not feasible to capture the behavior during extracellular electric stimulation accurately. With recent progress in mapping and reconstructing parts of the retina (e.g. Helmstaedter *et al.* (2013)) morphological data became available to establish such large-scale models. Thus, detailed models of small patches of the retina might become tangible in the close future.

Results from recent experimental studies showed that focal stimulation of GCs is generally possible (Jepson *et al.* (2013); Sekirnjak *et al.* (2008)). This is especially interesting for future epiretinal prostheses which might be able to provide precise spatiotemporal AP patterns to the brain as shown *in-vitro* (Jepson *et al.* (2014b)). Furthermore, the possibility of concurrent stimulation with more than a single electrode seems to increase the chance for GC activation in close proximity of the electrode (Jepson *et al.* (2014a)). However, no of these new stimulating strategies made it to clinical trials and there are still many (mostly technological) obstacles to overcome.

5.3 Final words

Up to date, nobody can make reliable forecasts about the progression of retinal implant technology in the future. Since the 1980s much progress has been made, however, restoration of vision using retinal implants still has not reached a satisfying level for both, patients and researchers. Too many unknowns are still hindering a better understanding of processes in the electrically stimulated retina. The presented study as my personal input to this field revealed at least a small portion of these unknown phenomena and therefore hopefully contributes to the development of future retinal neuroprostheses allowing blind people experience a higher quality of vision.

References

AHN, K.N., AHN, J.Y., KIM, J.H., CHO, K., KOO, K.I., SENOK, S.S. & GOO, Y.S. (2015). Effect of stimulus waveform of biphasic current pulse on retinal ganglion cell responses in retinal degeneration (rd1) mice. *Korean J Physiol Pharmacol*, **19**, 167–75. 124

AHUJA, A.K., BEHREND, M.R., KURODA, M., HUMAYUN, M.S. & WEILAND, J.D. (2008). An in vitro model of a retinal prosthesis. *IEEE Trans Biomed Eng*, **55**, 1744–53. 124

AHUJA, A.K., YEOH, J., DORN, J.D., CASPI, A., WUYYURU, V., MCMAHON, M.J., HUMAYUN, M.S., GREENBERG, R.J. & DACRUZ, L. (2013). Factors affecting perceptual threshold in argus ii retinal prosthesis subjects. *Transl Vis Sci Technol*, **2**, 1. 12

ANDERSON, E., BAI, Z., BISCHOF, C., BLACKFORD, S., DEMMER, J., DONGARRA, J., DU CROZ, J., GREENBAUM, A., HAMMARLING, S., MCKENNEY, A. & SORENSEN, D. (1999). *LAPACK Users' Guide*. Society for Industrial and Applied Mathematics. 42

ASANUMA, D.H. & ROSÉN, I. (1973). Spread of mono- and polysynaptic connections within cat's motor cortex. *Exp Brain Res*, **16**, 507–520. 69

ASCOLI, G.A., DONOHUE, D.E. & HALAVI, M. (2007). Neuromorpho.org: a central resource for neuronal morphologies. *J Neurosci*, **27**, 9247–51. 34

AYTON, L.N., BLAMEY, P.J., GUYMER, R.H., LUU, C.D., NAYAGAM, D.A.X., SINCLAIR, N.C., SHIVDASANI, M.N., YEOH, J., MCCOMBE, M.F., BRIGGS, R.J., OPIE, N.L., VILLALOBOS, J., DIMITROV, P.N., VARSAMIDIS, M., PETOE, M.A., MCCARTHY, C.D., WALKER, J.G., BARNES, N., BURKITT, A.N., WILLIAMS, C.E., SHEPHERD, R.K., ALLEN, P.J. & BIONIC VISION AUSTRALIA RESEARCH CONSORTIUM (2014). First-in-human trial of a novel suprachoroidal retinal prosthesis. *PLoS One*, **9**, e115239. 3, 12, 122

BADEN, T., BERENS, P., BETHGE, M. & EULER, T. (2013a). Spikes in mammalian bipolar cells support temporal layering of the inner retina. *Curr. Biol.*, **23**, 48–52. 68

BADEN, T., EULER, T., WECKSTROM, M. & LAGNADO, L. (2013b). Spikes and ribbon synapses in early vision. *Trends Neurosci.*, **36**, 480–488. 70

BAK, M., GIRVIN, J.P., HAMBRECHT, F.T., KUFTA, C.V., LOEB, G.E. & SCHMIDT, E.M. (1990). Visual sensations produced by intracortical microstimulation of the human occipital cortex. *Med Biol Eng Comput*, **28**, 257–9. 2

REFERENCES

BEHREND, M.R., AHUJA, A.K., HUMAYUN, M.S., CHOW, R.H. & WEILAND, J.D. (2011). Resolution of the epiretinal prosthesis is not limited by electrode size. *IEEE Trans Neural Syst Rehabil Eng*, **19**, 436–42. 12

BENAV, H. (2012). *Modelling effects of extracellular stimulation on retinal bipolar cells*. Ph.D. thesis, Eberhard-Karls-Universitaet Tuebingen. 10, 25, 35, 36, 37, 70, 130

BENDALI, A., ROUSSEAU, L., LISSORGUES, G., SCORSONE, E., DJILAS, M., DÉGARDIN, J., DUBUS, E., FOUQUET, S., BENOSMAN, R., BERGONZO, P., SAHEL, J.A. & PICAUD, S. (2015). Synthetic 3d diamond-based electrodes for flexible retinal neuroprostheses: Model, production and in vivo biocompatibility. *Biomaterials*, **67**, 73–83. 12

BENISON, G., KEIZER, J., CHALUPA, L.M. & ROBINSON, D.W. (2001). Modeling temporal behavior of postnatal cat retinal ganglion cells. *J Theor Biol*, **210**, 187–99. 50

BESCH, D., SACHS, H., SZURMAN, P., GÜLICHER, D., WILKE, R., REINERT, S., ZRENNER, E., BARTZ-SCHMIDT, K.U. & GEKELER, F. (2008). Extraocular surgery for implantation of an active subretinal visual prosthesis with external connections: feasibility and outcome in seven patients. *Br J Ophthalmol*, **92**, 1361–8. 25

BOIKO, T., VAN WART, A., CALDWELL, J.H., LEVINSON, S.R., TRIMMER, J.S. & MATTHEWS, G. (2003). Functional specialization of the axon initial segment by isoform-specific sodium channel targeting. *J Neurosci*, **23**, 2306–13. 10, 73, 117, 118

BOINAGROV, D., LOUDIN, J. & PALANKER, D. (2010). Strength-duration relationship for extracellular neural stimulation: numerical and analytical models. *J Neurophysiol*, **104**, 2236–48. 63

BOINAGROV, D., PANGRATZ-FUEHRER, S., SUH, B., MATHIESON, K., NAIK, N. & PALANKER, D. (2012). Upper threshold of extracellular neural stimulation. *J. Neurophysiol.*, **108**, 3233–3238. 63

BOINAGROV, D., PANGRATZ-FUEHRER, S., GOETZ, G. & PALANKER, D. (2014). Selectivity of direct and network-mediated stimulation of the retinal ganglion cells with epi-, sub- and intraretinal electrodes. *J Neural Eng*, **11**, 026008. 64, 115, 116, 125

BOYCOTT, B.B., DOWLING, J.E. & KOLB, H. (1969). Organization of the primate retina: Light microscopy. *Philosophical Transactions of the Royal Society of London B: Biological Sciences*, **255**, 109–184. 6

BRINDLEY, G.S. & LEWIN, W.S. (1968). The visual sensations produced by electrical stimulation of the medial occipital cortex. *J Physiol*, **194**, 54–5P. 2

BRUMMER, S.B. & TURNER, M.J. (1977). Electrical stimulation with pt electrodes: Ii-estimation of maximum surface redox (theoretical non-gassing) limits. *IEEE Trans Biomed Eng*, **24**, 440–3. 87, 114, 122

BUITENWEG, J.R., RUTTEN, W.L.C. & MARANI, E. (2002). Extracellular stimulation window explained by a geometry-based model of the neuron-electrode contact. *IEEE Trans. Biomed. Eng.*, **49**, 1591–1599. 63

BUSSKAMP, V., DUEBEL, J., BALYA, D., FRADOT, M., VINEY, T.J., SIEGERT, S., GRONER, A.C., CABUY, E., FORSTER, V., SEELIGER, M., BIEL, M., HUMPHRIES, P., PAQUES, M., MOHAND-SAID, S., TRONO, D., DEISSEROTH, K., SAHEL, J.A., PICAUD, S. & ROSKA, B. (2010). Genetic reactivation of cone photoreceptors restores visual responses in retinitis pigmentosa. *Science*, **329**, 413–7. 2

BUTSON, C.R. & MCINTYRE, C.C. (2008). Current steering to control the volume of tissue activated during deep brain stimulation. *Brain Stimul*, **1**, 7–15. 13

BUTTERWICK, A., HUIE, P., JONES, B.W., MARC, R.E., MARMOR, M. & PALANKER, D. (2009). Effect of shape and coating of a subretinal prosthesis on its integration with the retina. *Exp Eye Res*, **88**, 22–9. 119

CAI, C., REN, Q., DESAI, N.J., RIZZO, J.F., 3RD & FRIED, S.I. (2011). Response variability to high rates of electric stimulation in retinal ganglion cells. *J Neurophysiol*, **106**, 153–62. 124

CARNEVALE, N. & HINES, M. (2006). *The NEURON Book*. Cambridge University Press. 44

CHAKRAVARTHY, U., WONG, T.Y., FLETCHER, A., PIAULT, E., EVANS, C., ZLATEVA, G., BUGGAGE, R., PLEIL, A. & MITCHELL, P. (2010). Clinical risk factors for age-related macular degeneration: a systematic review and meta-analysis. *BMC Ophthalmol*, **10**, 31. 8

CHO, A.K., SAMPATH, A.P. & WEILAND, J.D. (2012). Physiological response of normal and rd mouse retinal ganglion cells to electrical stimulation. *Conf Proc IEEE Eng Med Biol Soc*, **2012**, 2985–8. 115

CHOW, A.Y., BITTNER, A.K. & PARDUE, M.T. (2010). The artificial silicon retina in retinitis pigmentosa patients (an american ophthalmological association thesis). *Trans Am Ophthalmol Soc*, **108**, 120–54. 3

COBURN, B. (1989). Neural modeling in electrical stimulation. *Crit Rev Biomed Eng*, **17**, 133–78. 26

COGAN, S.F., TROYK, P.R., EHRLICH, J. & PLANTE, T.D. (2005). In vitro comparison of the charge-injection limits of activated iridium oxide (airof) and platinum-iridium microelectrodes. *IEEE Trans Biomed Eng*, **52**, 1612–4. 122

CRANK, J. & NICOLSON, P. (1947). A practical method for numerical evaluation of solutions of partial differential equations of the heat-conduction type. *Proc. Camb. Phil. Soc.*, **43**, 50–67. 28

CUI, J. & PAN, Z.H. (2008). Two types of cone bipolar cells express voltage-gated na+ channels in the rat retina. *Visual Neurosci.*, **25**, 635–645. 70

DESOYER, I. & HOCHMAIR, E. (1977). Implantable eight-channel stimulator for the deaf. In *Solid State Circuits Conference, 1977. ESSCIRC '77. 3rd European*, 87–89. 1

DIFRANCESCO, D. & NOBLE, D. (1985). A model of cardiac electrical-activity incorporating ionic pumps and concentration changes. *Philos. Trans. R. Soc. Lond. Ser. B-Biol. Sci.*, **307**, 353–398. 70

REFERENCES

DOBELLE, W.H. & MLADEJOVSKY, M.G. (1974). Phosphenes produced by electrical stimulation of human occipital cortex, and their application to the development of a prosthesis for the blind. *J Physiol*, **243**, 553–76. 2

DOWLING, J. (2009). Current and future prospects for optoelectronic retinal prostheses. *Eye (Lond)*, **23**, 1999–2005. 2

DRÄGER, U.C. & HUBEL, D.H. (1978). Studies of visual function and its decay in mice with hereditary retinal degeneration. *J Comp Neurol*, **180**, 85–114. 120

DREOSTI, E., ESPOSTI, F., BADEN, T. & LAGNADO, L. (2011). In vivo evidence that retinal bipolar cells generate spikes modulated by light. *Nat. Neurosci.*, **14**, 951–952. 70

DUNCAN, G., RABL, K., GEMP, I., HEIDELBERGER, R. & THORESON, W.B. (2010). Quantitative analysis of synaptic release at the photoreceptor synapse. *Biophys J*, **98**, 2102–10. 39, 69

EICKENSCHEIDT, M. & ZECK, G. (2014). Action potentials in retinal ganglion cells are initiated at the site of maximal curvature of the extracellular potential. *J Neural Eng*, **11**, 036006. 9, 98

EICKENSCHEIDT, M., JENKNER, M., THEWES, R., FROMHERZ, P. & ZECK, G. (2012). Electrical stimulation of retinal neurons in epiretinal and subretinal configuration using a multicapacitor array. *J Neurophysiol*, **107**, 2742–55. 47, 115, 116, 123, 125

ENCKE, J., BENAV, H., WERGINZ, P., ZRENNER, E. & RATTAY, F. (2013). Investigating the influence of 3d cell morphology on neural response during electrical stimulation. *Biomed Tech (Berl)*. 35

EULER, T. & MASLAND, R.H. (2000). Light-evoked responses of bipolar cells in a mammalian retina. *J. Neurophysiol.*, **83**, 1817–1829. 66

EULER, T. & WÄSSLE, H. (1995). Immunocytochemical identification of cone bipolar cells in the rat retina. *J Comp Neurol*, **361**, 461–78. 6, 35, 66

EULER, T., HAVERKAMP, S., SCHUBERT, T. & BADEN, T. (2014). Retinal bipolar cells: elementary building blocks of vision. *Nat Rev Neurosci*, **15**, 507–19. 7, 64

FITZHUGH, R. (1961). Impulses and physiological states in theoretical models of nerve membrane. *Biophys J*, **1**, 445–66. 21

FOHLMEISTER, J.F. & MILLER, R.F. (1997). Impulse encoding mechanisms of ganglion cells in the tiger salamander retina. *J Neurophysiol*, **78**, 1935–47. 126

FOHLMEISTER, J.F., COLEMAN, P.A. & MILLER, R.F. (1990). Modeling the repetitive firing of retinal ganglion cells. *Brain Res*, **510**, 343–5. 21, 50, 70, 126

FOHLMEISTER, J.F., COHEN, E.D. & NEWMAN, E.A. (2010). Mechanisms and distribution of ion channels in retinal ganglion cells: using temperature as an independent variable. *J Neurophysiol*, **103**, 1357–74. 103, 124, 126

FORNOS, A.P., SOMMERHALDER, J., DA CRUZ, L., SAHEL, J.A., MOHAND-SAID, S., HAFEZI, F. & PELIZZONE, M. (2012). Temporal properties of visual perception on electrical stimulation of the retina. *Invest. Ophthalmol. Vis. Sci.*, **53**, 2720–2731. 65

Forti, S., Menini, A., Rispoli, G. & Torre, V. (1989). Kinetics of phototransduction in retinal rods of the newt triturus-christatus. *J. Physiol.-London*, **419**, 265–295. 70

Frankenhaeuser, B. & Huxley, A.F. (1964). The action potential in the myelinated nerve fiber of xenopus laevis as computed on the basis of voltage clamp data. *J Physiol*, **171**, 302–15. 21

Freeman, D.K., Eddington, D.K., Rizzo, J.F., 3rd & Fried, S.I. (2010). Selective activation of neuronal targets with sinusoidal electric stimulation. *J Neurophysiol*, **104**, 2778–91. 11

Fried, S.I., Hsueh, H.A. & Werblin, F.S. (2006). A method for generating precise temporal patterns of retinal spiking using prosthetic stimulation. *J Neurophysiol*, **95**, 970–8. 124

Fried, S.I., Lasker, A.C.W., Desai, N.J., Eddington, D.K. & Rizzo, J.F., 3rd (2009). Axonal sodium-channel bands shape the response to electric stimulation in retinal ganglion cells. *J Neurophysiol*, **101**, 1972–87. 11, 68, 73, 74, 76, 78, 82, 115, 118, 120, 122, 125

Fujikado, T., Morimoto, T., Kanda, H., Kusaka, S., Nakauchi, K., Ozawa, M., Matsushita, K., Sakaguchi, H., Ikuno, Y., Kamei, M. & Tano, Y. (2007). Evaluation of phosphenes elicited by extraocular stimulation in normals and by suprachoroidal-transretinal stimulation in patients with retinitis pigmentosa. *Graefes Arch Clin Exp Ophthalmol*, **245**, 1411–9. 3

Fyk-Kolodziej, B. & Pourcho, R.G. (2007). Differential distribution of hyperpolarization-activated and cyclic nucleotide-gated channels in cone bipolar cells of the rat retina. *J Comp Neurol*, **501**, 891–903. 6

Ganesan, K., Stacey, A., Meffin, H., Lichter, S., Greferath, U., Fletcher, E.L. & Prawer, S. (2010). Diamond penetrating electrode array for epi-retinal prosthesis. *Conf Proc IEEE Eng Med Biol Soc*, **2010**, 6757–60. 120

Ghosh, K.K., Bujan, S., Haverkamp, S., Feigenspan, A. & Wassle, H. (2004). Types of bipolar cells in the mouse retina. *J. Comp. Neurol.*, **469**, 70–82. 66

Goetz, G.A., Mandel, Y., Manivanh, R., Palanker, D.V. & Čižmár, T. (2013). Holographic display system for restoration of sight to the blind. *J Neural Eng*, **10**, 056021. 5

Goldin, A.L., Barchi, R.L., Caldwell, J.H., Hofmann, F., Howe, J.R., Hunter, J.C., Kallen, R.G., Mandel, G., Meisler, M.H., Netter, Y.B., Noda, M., Tamkun, M.M., Waxman, S.G., Wood, J.N. & Catterall, W.A. (2000). Nomenclature of voltage-gated sodium channels. *Neuron*, **28**, 365–8. 117

Greenberg, R.J., Velte, T.J., Humayun, M.S., Scarlatis, G.N. & de Juan, E., Jr (1999). A computational model of electrical stimulation of the retinal ganglion cell. *IEEE Trans Biomed Eng*, **46**, 505–14. 25, 125, 130

Guo, T., Tsai, D., Morley, J.W., Suaning, G.J., Lovell, N.H. & Dokos, S. (2013). Cell-specific modeling of retinal ganglion cell electrical activity. *Conf Proc IEEE Eng Med Biol Soc*, **2013**, 6539–42. 36, 80

REFERENCES

GUO, T., LOVELL, N.H., TSAI, D., TWYFORD, P., FRIED, S., MORLEY, J.W., SUANING, G.J. & DOKOS, S. (2014). Selective activation of on and off retinal ganglion cells to high-frequency electrical stimulation: a computational modeling study. *Conf Proc IEEE Eng Med Biol Soc*, **2014**, 6108–11. 10

HADJINICOLAOU, A.E., SAVAGE, C.O., APOLLO, N.V., GARRETT, D.J., CLOHERTY, S.L., IBBOTSON, M.R. & O'BRIEN, B.J. (2015). Optimizing the electrical stimulation of retinal ganglion cells. *IEEE Trans Neural Syst Rehabil Eng*, **23**, 169–78. 115, 124

HAIM, M. (2002). Epidemiology of retinitis pigmentosa in denmark. *Acta Ophthalmol Scand Suppl*, 1–34. 8

HEIDELBERGER, R. (2001). Electrophysiological approaches to the study of neuronal exocytosis and synaptic vesicle dynamics. *REV PHYSIOL BIOCH P*, **143**, 1–80. 69

HEIDELBERGER, R., HEINEMANN, C., NEHER, E. & MATTHEWS, G. (1994). Calcium dependence of the rate of exocytosis in a synaptic terminal. *Nature*, **371**, 513–5. 39, 69

HEIDELBERGER, R., STERLING, P. & MATTHEWS, G. (2002). Roles of atp in depletion and replenishment of the releasable pool of synaptic vesicles. *J Neurophysiol*, **88**, 98–106. 69

HEINEMANN, C., CHOW, R.H., NEHER, E. & ZUCKER, R.S. (1994). Kinetics of the secretory response in bovine chromaffin cells following flash photolysis of caged ca2+. *Biophys J*, **67**, 2546–57. 39, 69

HELMHOLTZ, H. (1850). Messungen über den zeitlichen Verlauf der Zuckung animalischer Muskeln und die Fortpflanzungsgeschwindigkeit der Reizung in den Nerven. *Archiv für Anatomie, Physiologie und wissenschaftliche Medicin*, **276**. 17

HELMSTAEDTER, M., BRIGGMAN, K.L., TURAGA, S.C., JAIN, V., SEUNG, H.S. & DENK, W. (2013). Connectomic reconstruction of the inner plexiform layer in the mouse retina. *Nature*, **500**, 168–74. 131

HINDMARSH, A., BROWN, P., GRANT, K., LEE, S., SERBAN, R., SHUMAKER, D. & WOODWARD, C. (2005). Sundials: Suite of nonlinear and differential/algebraic equation solvers. *ACM Transactions on Mathematical Software*, **31**, 363–396. 28

HINES, M. (1984). Efficient computation of branched nerve equations. *Int J Biomed Comput*, **15**, 69–76. 30

HINES, M.L. & CARNEVALE, N.T. (1997). The neuron simulation environment. *Neural Comput*, **9**, 1179–209. 17, 44

HODGKIN, A.L. & HUXLEY, A.F. (1952a). The components of membrane conductance in the giant axon of loligo. *J Physiol*, **116**, 473–96. 20

HODGKIN, A.L. & HUXLEY, A.F. (1952b). Currents carried by sodium and potassium ions through the membrane of the giant axon of loligo. *J Physiol*, **116**, 449–72. 20

HODGKIN, A.L. & HUXLEY, A.F. (1952c). The dual effect of membrane potential on sodium conductance in the giant axon of loligo. *J Physiol*, **116**, 497–506. 20

HODGKIN, A.L. & HUXLEY, A.F. (1952d). A quantitative description of membrane current and its application to conduction and excitation in nerve. *J Physiol*, **117**, 500–44. 17, 20

HODGKIN, A.L., HUXLEY, A.F. & KATZ, B. (1952). Measurement of current-voltage relations in the membrane of the giant axon of loligo. *J Physiol*, **116**, 424–48. 20

HU, C., BI, A. & PAN, Z.H. (2009a). Differential expression of three t-type calcium channels in retinal bipolar cells in rats. *Vis Neurosci*, **26**, 177–87. 37, 52, 71

HU, W., TIAN, C., LI, T., YANG, M., HOU, H. & SHU, Y. (2009b). Distinct contributions of na(v)1.6 and na(v)1.2 in action potential initiation and backpropagation. *Nat Neurosci*, **12**, 996–1002. 40, 75, 117, 127

HULL, C., STUDHOLME, K., YAZULLA, S. & VON GERSDORFF, H. (2006). Diurnal changes in exocytosis and the number of synaptic ribbons at active zones of an on-type bipolar cell terminal. *J Neurophysiol*, **96**, 2025–33. 69

HUMAYUN, M.S., PRINCE, M., DE JUAN, E., JR, BARRON, Y., MOSKOWITZ, M., KLOCK, I.B. & MILAM, A.H. (1999). Morphometric analysis of the extramacular retina from postmortem eyes with retinitis pigmentosa. *Invest Ophthalmol Vis Sci*, **40**, 143–8. 11

HUSSIN, A.T., BOYCHUK, J.A., BROWN, A.R., PITTMAN, Q.J. & TESKEY, G.C. (2015). Intracortical microstimulation (icms) activates motor cortex layer 5 pyramidal neurons mainly transsynaptically. *Brain Stimul.*, **8**, 742–750. 68

INGLEHEARN, C.F. (1998). Molecular genetics of human retinal dystrophies. *Eye (Lond)*, **12 (Pt 3b)**, 571–9. 8

IVANOVA, E. & MÜLLER, F. (2006). Retinal bipolar cell types differ in their inventory of ion channels. *Vis Neurosci*, **23**, 143–54. 6

JENG, J., TANG, S., MOLNAR, A., DESAI, N.J. & FRIED, S.I. (2011). The sodium channel band shapes the response to electric stimulation in retinal ganglion cells. *J Neural Eng*, **8**, 036022. 11, 76, 118, 126

JENSEN, R.J. & RIZZO, J.F., 3RD (2006). Thresholds for activation of rabbit retinal ganglion cells with a subretinal electrode. *Exp Eye Res*, **83**, 367–73. 58, 116, 125

JENSEN, R.J. & RIZZO, J.F., 3RD (2008). Activation of retinal ganglion cells in wild-type and rd1 mice through electrical stimulation of the retinal neural network. *Vision Res*, **48**, 1562–8. 116

JENSEN, R.J. & RIZZO, J.F., 3RD (2009). Activation of ganglion cells in wild-type and rd1 mouse retinas with monophasic and biphasic current pulses. *J Neural Eng*, **6**, 035004. 64

JENSEN, R.J., RIZZO, J.F., 3RD, ZIV, O.R., GRUMET, A. & WYATT, J. (2003). Thresholds for activation of rabbit retinal ganglion cells with an ultrafine, extracellular microelectrode. *Invest Ophthalmol Vis Sci*, **44**, 3533–43. 114, 116, 125

REFERENCES

JENSEN, R.J., ZIV, O.R. & RIZZO, J.F., 3RD (2005). Thresholds for activation of rabbit retinal ganglion cells with relatively large, extracellular microelectrodes. *Invest Ophthalmol Vis Sci*, **46**, 1486–96. 115, 116, 125

JEPSON, L.H., HOTTOWY, P., MATHIESON, K., GUNNING, D.E., DABROWSKI, W., LITKE, A.M. & CHICHILNISKY, E.J. (2013). Focal electrical stimulation of major ganglion cell types in the primate retina for the design of visual prostheses. *J Neurosci*, **33**, 7194–205. 131

JEPSON, L.H., HOTTOWY, P., MATHIESON, K., GUNNING, D.E., DABROWSKI, W., LITKE, A.M. & CHICHILNISKY, E.J. (2014a). Spatially patterned electrical stimulation to enhance resolution of retinal prostheses. *J Neurosci*, **34**, 4871–81. 13, 131

JEPSON, L.H., HOTTOWY, P., WEINER, G.A., DABROWSKI, W., LITKE, A.M. & CHICHILNISKY, E.J. (2014b). High-fidelity reproduction of spatiotemporal visual signals for retinal prosthesis. *Neuron*, **83**, 87–92. 13, 131

JONES, B.W., KONDO, M., TERASAKI, H., LIN, Y., MCCALL, M. & MARC, R.E. (2012). Retinal remodeling. *Jpn J Ophthalmol*, **56**, 289–306. 11

KARWOSKI, C.J., FRAMBACH, D.A. & PROENZA, L.M. (1985). Laminar profile of resistivity in frog retina. *J Neurophysiol*, **54**, 1607–19. 25, 125

KASI, H. (2011). *Analysis of factors affecting the performance of retinal prostheses using finite element modelling of electric field distribution in the retina*. Ph.D. thesis, Ecole Polytechnique Federale de Lausanne. 128

KASI, H., HASENKAMP, W., COSENDAI, G., BERTSCH, A. & RENAUD, P. (2011a). Simulation of epiretinal prostheses - evaluation of geometrical factors affecting stimulation thresholds. *J Neuroeng Rehabil*, **8**, 44. 25, 125

KASI, H., MEISSNER, R., BABALIAN, A., LINTEL, H.v., BERTSCH, A. & RENAUD, P. (2011b). Direct localised measurement of electrical resistivity profile in rat and embryonic chick retinas using a microprobe. *Journal of Electrical Bioimpedance*, **1**, 84–92. 128

KESERÜ, M., FEUCHT, M., BORNFELD, N., LAUBE, T., WALTER, P., RÖSSLER, G., VELIKAY-PAREL, M., HORNIG, R. & RICHARD, G. (2012). Acute electrical stimulation of the human retina with an epiretinal electrode array. *Acta Ophthalmol*, **90**, e1–8. 3

KHALILI MOGHADAM, G., WILKE, R., DOKOS, S., SUANING, G. & LOVELL, N. (2011). Electrode design to optimize ganglion cell activation in a retinal neuroprosthesis: A modeling study. In *2011 5th International IEEE/EMBS Conference on Neural Engineering (NER)*, 542–545. 13, 130

KHALILI MOGHADAM, G., WILKE, R., SUANING, G.J., LOVELL, N.H. & DOKOS, S. (2013). Quasi-monopolar stimulation: a novel electrode design configuration for performance optimization of a retinal neuroprosthesis. *PLoS One*, **8**, e73130. 13

KHRAICHE, M.L., LO, Y., WANG, D., CAUWENBERGHS, G., FREEMAN, W. & SILVA, G.A. (2011). Ultra-high photosensitivity silicon nanophotonics for retinal prosthesis: electrical characteristics. *Conf Proc IEEE Eng Med Biol Soc*, **2011**, 2933–6. 119

KIM, C.S. & OH, S.M. (1996). Enzyme sensors prepared by electrodeposition on platinized platinum electrodes. *Electrochim. Acta*, **41**, 2433–2439. 122

KLAUKE, S., GOERTZ, M., REIN, S., HOEHL, D., THOMAS, U., ECKHORN, R., BREMMER, F. & WACHTLER, T. (2011). Stimulation with a wireless intraocular epiretinal implant elicits visual percepts in blind humans. *Invest Ophthalmol Vis Sci*, **52**, 449–55. 3

KOLB, H., NELSON, R. & MARIANI, A. (1981). Amacrine cells, bipolar cells and ganglion cells of the cat retina: a golgi study. *Vision Res*, **21**, 1081–1114. 6

KONG, J.H., FISH, D.R., ROCKHILL, R.L. & MASLAND, R.H. (2005). Diversity of ganglion cells in the mouse retina: unsupervised morphological classification and its limits. *J Comp Neurol*, **489**, 293–310. 103, 104, 105

KUTTA, M. (1901). Beitrag zur näherungsweisen Integration totaler Differentialgleichungen. *Zeitschrift für Mathematik und Physik*, **46**, 435–453. 28

LEE, S.W., EDDINGTON, D.K. & FRIED, S.I. (2013). Responses to pulsatile subretinal electric stimulation: effects of amplitude and duration. *J Neurophysiol*, **109**, 1954–68. 116

LOGIUDICE, L., STERLING, P. & MATTHEWS, G. (2009). Vesicle recycling at ribbon synapses in the finely branched axon terminals of mouse retinal bipolar neurons. *Neuroscience*, **164**, 1546–56. 39

LORACH, H., GOETZ, G., MANDEL, Y., LEI, X., KAMINS, T.I., MATHIESON, K., HUIE, P., DALAL, R., HARRIS, J.S. & PALANKER, D. (2015a). Performance of photovoltaic arrays in-vivo and characteristics of prosthetic vision in animals with retinal degeneration. *Vision Res*, **111**, 142–8. 64

LORACH, H., GOETZ, G., SMITH, R., LEI, X., MANDEL, Y., KAMINS, T., MATHIESON, K., HUIE, P., HARRIS, J., SHER, A. & PALANKER, D. (2015b). Photovoltaic restoration of sight with high visual acuity. *Nat Med*, **21**, 476–82. 3, 5

LU, Y., YAN, Y., CHAI, X., REN, Q., CHEN, Y. & LI, L. (2013). Electrical stimulation with a penetrating optic nerve electrode array elicits visuotopic cortical responses in cats. *J Neural Eng*, **10**, 036022. 2

MAGUIRE, G., MAPLE, B., LUKASIEWICZ, P. & WERBLIN, F. (1989). Gamma-aminobutyrate type b receptor modulation of l-type calcium channel current at bipolar cell terminals in the retina of the tiger salamander. *Proc Natl Acad Sci U S A*, **86**, 10144–7. 37

MAINEN, Z.F., JOERGES, J., HUGUENARD, J.R. & SEJNOWSKI, T.J. (1995). A model of spike initiation in neocortical pyramidal neurons. *Neuron*, **15**, 1427–39. 41

MARC, R.E., JONES, B.W., ANDERSON, J.R., KINARD, K., MARSHAK, D.W., WILSON, J.H., WENSEL, T. & LUCAS, R.J. (2007). Neural reprogramming in retinal degeneration. *Invest Ophthalmol Vis Sci*, **48**, 3364–71. 11

MARGOLIS, D.J. & DETWILER, P.B. (2011). Cellular origin of spontaneous ganglion cell spike activity in animal models of retinitis pigmentosa. *J Ophthalmol*, **2011**. 120

REFERENCES

MARGOLIS, D.J., NEWKIRK, G., EULER, T. & DETWILER, P.B. (2008). Functional stability of retinal ganglion cells after degeneration-induced changes in synaptic input. *J Neurosci*, **28**, 6526–36. 120

MARGOLIS, D.J., GARTLAND, A.J., EULER, T. & DETWILER, P.B. (2010). Dendritic calcium signaling in on and off mouse retinal ganglion cells. *J. Neurosci.*, **30**, 7127–7138. 119

MARMONT, G. (1949). Studies on the axon membrane; a new method. *J Cell Physiol*, **34**, 351–82. 21

MASLAND, R.H. (2001). The fundamental plan of the retina. *Nat Neurosci*, **4**, 877–86. 6, 7

MASLAND, R.H. (2012a). The neuronal organization of the retina. *Neuron*, **76**, 266–80. 7

MASLAND, R.H. (2012b). The tasks of amacrine cells. *Vis Neurosci*, **29**, 3–9. 6, 7, 67

MATHIESON, K., KACHIGUINE, S., ADAMS, C., CUNNINGHAM, W., GUNNING, D., O'SHEA, V., SMITH, K.M., CHICHILNISKY, E.J., LITKE, A.M., SHER, A. & RAHMAN, M. (2004). Large-area microelectrode arrays for recording of neural signals. *IEEE Trans. Nucl. Sci.*, **51**, 2027–2031. 122

MATHIESON, K., LOUDIN, J., GOETZ, G., HUIE, P., WANG, L., KAMINS, T.I., GALAMBOS, L., SMITH, R., HARRIS, J.S., SHER, A. & PALANKER, D. (2012). Photovoltaic retinal prosthesis with high pixel density. *Nat Photonics*, **6**, 391–397. 119

MATHIESON, K., MOODIE, A.R., GRANT, E. & MORRISON, J.D. (2013). Development and evaluation of thin-film flexible microelectrode arrays for retinal stimulation and recording. *J Med Eng Technol*, **37**, 79–85. 12

MATTEUCCI, P.B., CHEN, S.C., TSAI, D., DODDS, C.W.D., DOKOS, S., MORLEY, J.W., LOVELL, N.H. & SUANING, G.J. (2013). Current steering in retinal stimulation via a quasimonopolar stimulation paradigm. *Invest Ophthalmol Vis Sci*, **54**, 4307–20. 13

MCNEAL, D.R. (1976). Analysis of a model for excitation of myelinated nerve. *IEEE Trans Biomed Eng*, **23**, 329–37. 23

MEFFIN, H., TAHAYORI, B., GRAYDEN, D.B. & BURKITT, A.N. (2012). Modeling extracellular electrical stimulation: I. derivation and interpretation of neurite equations. *J Neural Eng*, **9**, 065005. 17

MEFFIN, H., TAHAYORI, B., SERGEEV, E.N., MAREELS, I.M.Y., GRAYDEN, D.B. & BURKITT, A.N. (2014). Modelling extracellular electrical stimulation: part 3. derivation and interpretation of neural tissue equations. *J Neural Eng*, **11**, 065004. 23

MENNERICK, S. & MATTHEWS, G. (1996). Ultrafast exocytosis elicited by calcium current in synaptic terminals of retinal bipolar neurons. *Neuron*, **17**, 1241–1249. 69

MERRILL, D.R., BIKSON, M. & JEFFERYS, J.G.R. (2005). Electrical stimulation of excitable tissue: design of efficacious and safe protocols. *J Neurosci Methods*, **141**, 171–98. 121

MINNIKANTI, S., COHEN, E. & PEIXOTO, N. (2010). Quasi-static analysis of electric field distributions by disc electrode in a rabbit eye model. In K.E. Herold, J. Vossoughi & W.E. Bentley, eds., *26th Southern Biomedical Engineering Conference SBEC 2010, April 30 - May 2, 2010, College*

Park, Maryland, USA, no. 32 in IFMBE Proceedings, 385–388, Springer Berlin Heidelberg, dOI: 10.1007/978-3-642-14998-6_98. 127

NANDURI, D., FINE, I., HORSAGER, A., BOYNTON, G.M., HUMAYUN, M.S., GREENBERG, R.J. & WEILAND, J.D. (2012). Frequency and amplitude modulation have different effects on the percepts elicited by retinal stimulation. *Invest. Ophthalmol. Vis. Sci.*, **53**, 205–214. 11, 121

NEHER, E. & SAKABA, T. (2008). Multiple roles of calcium ions in the regulation of neurotransmitter release. *Neuron*, **59**, 861–872. 69

NODA, T., SASAGAWA, K., TOKUDA, T., TERASAWA, Y., TASHIRO, H., KANDA, H., FUJIKADO, T. & OHTA, J. (2014). Performance improvement and functionalization of an electrode array for retinal prosthesis by iridium oxide coating and introduction of smart-wiring technology using cmos microchips. *Sens. Actuator A-Phys.*, **211**, 27–37. 122

NORMANN, R.A., GREGER, B., GREGER, B.A., HOUSE, P., ROMERO, S.F., PELAYO, F. & FERNANDEZ, E. (2009). Toward the development of a cortically based visual neuroprosthesis. *J Neural Eng*, **6**, 035001. 2

NOWAK, L.G. & BULLIER, J. (1998). Axons, but not cell bodies, are activated by electrical stimulation in cortical gray matter ii. evidence from selective inactivation of cell bodies and axon initial segments. *Exp. Brain Res.*, **118**, 489–500. 68

OLTEDAL, L. & HARTVEIT, E. (2010). Transient release kinetics of rod bipolar cells revealed by capacitance measurement of exocytosis from axon terminals in rat retinal slices. *J Physiol*, **588**, 1469–87. 37, 39, 51, 52, 68

OSTERBERG, G. (1935). Topography of the layer of rods and cones in the human retina. *Acta Ophtalmol*, **13**, 1–103. 6

PALANKER, D., VANKOV, A., HUIE, P. & BACCUS, S. (2005). Design of a high-resolution optoelectronic retinal prosthesis. *J Neural Eng*, **2**, S105–20. 119

PAN, Z.H. (2000). Differential expression of high- and two types of low-voltage-activated calcium currents in rod and cone bipolar cells of the rat retina. *J. Neurophysiol.*, **83**, 513–527. 71

PAN, Z.H., HU, H.J., PERRING, P. & ANDRADE, R. (2001). T-type ca2+ channels mediate neurotransmitter release in retinal bipolar cells. *Neuron*, **32**, 89–98. 71

PANETSOS, F., SANCHEZ-JIMENEZ, A., CERIO, E.D.D., DIAZ-GUEMES, I. & SANCHEZ, F.M. (2011). Consistent phosphenes generated by electrical microstimulation of the visual thalamus. an experimental approach for thalamic visual neuroprostheses. *Front Neurosci*, **5**, 84. 2

PETERSON, N.R., PISONI, D.B. & MIYAMOTO, R.T. (2010). Cochlear implants and spoken language processing abilities: review and assessment of the literature. *Restor Neurol Neurosci*, **28**, 237–50. 1

PEZARIS, J.S. & REID, R.C. (2007). Demonstration of artificial visual percepts generated through thalamic microstimulation. *Proc Natl Acad Sci U S A*, **104**, 7670–5. 2

POLYAK, S. (1941). *The Retina*. University of Chicago Press, Chicago. 5, 6

REFERENCES

PROTTI, D.A. & LLANO, I. (1998). Calcium currents and calcium signaling in rod bipolar cells of rat retinal slices. *J Neurosci*, **18**, 3715–24. 50, 52, 68

QUIGLEY, H.A., ADDICKS, E.M. & GREEN, W.R. (1982). Optic nerve damage in human glaucoma. iii. quantitative correlation of nerve fiber loss and visual field defect in glaucoma, ischemic neuropathy, papilledema, and toxic neuropathy. *Arch Ophthalmol*, **100**, 135–46. 6

RALL, W. (1962a). Electrophysiology of a dendritic neuron model. *Biophys J*, **2**, 145–67. 17

RALL, W. (1962b). Theory of physiological properties of dendrites. *Ann N Y Acad Sci*, **96**, 1071–92. 17

RALL, W. (1964). *Neural Theory and Modeling*, chap. Theoretical significance of dendritic trees for neuronal input-output relations, 73–97. Stanford University Press. 17

RANCK, J.B., JR (1975). Which elements are excited in electrical stimulation of mammalian central nervous system: a review. *Brain Res*, **98**, 417–40. 9

RATNAPRIYA, R. & CHEW, E.Y. (2013). Age-related macular degeneration-clinical review and genetics update. *Clin Genet*, **84**, 160–6. 8

RATTAY, F. (1986). Analysis of models for external stimulation of axons. *IEEE Trans Biomed Eng*, **33**, 974–7. 9, 25, 26, 67, 89, 100, 123

RATTAY, F. (1988). Modeling the excitation of fibers under surface electrodes. *IEEE Trans Biomed Eng*, **35**, 199–202. 89

RATTAY, F. (1999). The basic mechanism for the electrical stimulation of the nervous system. *Neuroscience*, **89**, 335–46. 9, 10, 23, 26, 44, 67, 102

RATTAY, F. (2014). On the upper threshold phenomenon of extracellular neural stimulation. *J Neurophysiol*, **112**, 2664–5. 36

RATTAY, F. & WENGER, C. (2010). Which elements of the mammalian central nervous system are excited by low current stimulation with microelectrodes? *Neuroscience*, **170**, 399–407. 40, 41, 68, 118

RATTAY, F., LUTTER, P. & FELIX, H. (2001). A model of the electrically excited human cochlear neuron. i. contribution of neural substructures to the generation and propagation of spikes. *Hear Res*, **153**, 43–63. 41, 120

RATTAY, F., GREENBERG, R.J. & RESATZ, S. (2003). *Handbook of Neuroprosthetic Methods*, chap. Neuron modeling. CRC Press LLC. 19

RATTAY, F., PAREDES, L.P. & LEAO, R.N. (2012). Strength-duration relationship for intra-versus extracellular stimulation with microelectrodes. *Neuroscience*, **214**, 1–13. 68, 69

RESATZ, S. (2005). *Analysis of Retinal Cell Excitation with Visual Neuroprostheses*. Ph.D. thesis, Vienna University of Technology. 19, 130

RISTAU, T., ERSOY, L., HAHN, M., DEN HOLLANDER, A.I., KIRCHHOF, B., LIAKOPOULOS, S. & FAUSER, S. (2014). Nongenetic risk factors for neovascular age-related macular degeneration. *Invest Ophthalmol Vis Sci*, **55**, 5228–32. 8

RIZZO, J.F., 3RD (2011). Update on retinal prosthetic research: the boston retinal implant project. *J Neuroophthalmol*, **31**, 160–8. 3

RIZZO, S., BELTING, C., CINELLI, L., ALLEGRINI, L., GENOVESI-EBERT, F., BARCA, F. & DI BARTOLO, E. (2014). The argus ii retinal prosthesis: 12-month outcomes from a single-study center. *Am J Ophthalmol*, **157**, 1282–90. 3

ROSE, T.L. & ROBBLEE, L.S. (1990). Electrical stimulation with pt electrodes. viii. electrochemically safe charge injection limits with 0.2 ms pulses. *IEEE Trans Biomed Eng*, **37**, 1118–20. 87, 114, 122

SAĞLAM, M., HAYASHIDA, Y. & MURAYAMA, N. (2009). A retinal circuit model accounting for widefield amacrine cells. *Cogn Neurodyn*, **3**, 25–32. 131

SAKABA, T., TACHIBANA, M., MATSUI, K. & MINAMI, N. (1997). Two components of transmitter release in retinal bipolar cells: exocytosis and mobilization of synaptic vesicles. *Neurosci Res*, **27**, 357–70. 69

SAKAGUCHI, H., KAMEI, M., FUJIKADO, T., YONEZAWA, E., OZAWA, M., CECILIA-GONZALEZ, C., USTARIZ-GONZALEZ, O., QUIROZ-MERCADO, H. & TANO, Y. (2009). Artificial vision by direct optic nerve electrode (av-done) implantation in a blind patient with retinitis pigmentosa. *J Artif Organs*, **12**, 206–9. 2

SANTOS, A., HUMAYUN, M.S., DE JUAN, E., JR, GREENBURG, R.J., MARSH, M.J., KLOCK, I.B. & MILAM, A.H. (1997). Preservation of the inner retina in retinitis pigmentosa. a morphometric analysis. *Arch Ophthalmol*, **115**, 511–5. 11

SAVAGE, C.O., KIRAL-KORNEK, F.I., TAHAYORI, B. & GRAYDEN, D.B. (2012). Can electric current steering be used to control perception of a retinal prosthesis patient. *Conf Proc IEEE Eng Med Biol Soc*, **2012**, 3013–6. 13

SCHOEN, I. & FROMHERZ, P. (2008). Extracellular stimulation of mammalian neurons through repetitive activation of na+ channels by weak capacitive currents on a silicon chip. *J Neurophysiol*, **100**, 346–57. 123

SEKIRNJAK, C., HOTTOWY, P., SHER, A., DABROWSKI, W., LITKE, A.M. & CHICHILNISKY, E.J. (2006). Electrical stimulation of mammalian retinal ganglion cells with multielectrode arrays. *J Neurophysiol*, **95**, 3311–27. 87, 88, 114, 122

SEKIRNJAK, C., HOTTOWY, P., SHER, A., DABROWSKI, W., LITKE, A.M. & CHICHILNISKY, E.J. (2008). High-resolution electrical stimulation of primate retina for epiretinal implant design. *J Neurosci*, **28**, 4446–56. 82, 120, 131

SHAH, K.G., TOLOSA, V.M., TOOKER, A.C., FELIX, S.H. & PANNU, S.S. (2013). Improved chronic neural stimulation using high surface area platinum electrodes. *Conf Proc IEEE Eng Med Biol Soc*, **2013**, 1546–9. 123

REFERENCES

SHEPHERD, R.K., SHIVDASANI, M.N., NAYAGAM, D.A.X., WILLIAMS, C.E. & BLAMEY, P.J. (2013). Visual prostheses for the blind. *Trends Biotechnol*, **31**, 562–71. 2

SIKORA, M.A., GOTTESMAN, J. & MILLER, R.F. (2005). A computational model of the ribbon synapse. *J Neurosci Methods*, **145**, 47–61. 37

SINGER, J.H. & DIAMOND, J.S. (2003). Sustained ca2+ entry elicits transient postsynaptic currents at a retinal ribbon synapse. *J Neurosci*, **23**, 10923–33. 56, 71

SINGER, J.H. & DIAMOND, J.S. (2006). Vesicle depletion and synaptic depression at a mammalian ribbon synapse. *J Neurophysiol*, **95**, 3191–8. 38, 39, 56, 57, 69

SINGER, J.H., LASSOVA, L., VARDI, N. & DIAMOND, J.S. (2004). Coordinated multivesicular release at a mammalian ribbon synapse. *Nat. Neurosci.*, **7**, 826–833. 57, 65

SMITH, W., ASSINK, J., KLEIN, R., MITCHELL, P., KLAVER, C.C., KLEIN, B.E., HOFMAN, A., JENSEN, S., WANG, J.J. & DE JONG, P.T. (2001). Risk factors for age-related macular degeneration: Pooled findings from three continents. *Ophthalmology*, **108**, 697–704. 8

SNELLMAN, J., ZENISEK, D. & NAWY, S. (2009). Switching between transient and sustained signalling at the rod bipolar-aii amacrine cell synapse of the mouse retina. *J Physiol*, **587**, 2443–55. 56, 66

SOLINÍS, M.Á., DEL POZO-RODRÍGUEZ, A., APAOLAZA, P.S. & RODRÍGUEZ-GASCÓN, A. (2014). Treatment of ocular disorders by gene therapy. *Eur J Pharm Biopharm*. 2

SOTO, F., BLECKERT, A., LEWIS, R., KANG, Y., KERSCHENSTEINER, D., CRAIG, A.M. & WONG, R.O.L. (2011). Coordinated increase in inhibitory and excitatory synapses onto retinal ganglion cells during development. *Neural Dev*, **6**, 31. 6

SPAMPANATO, J., ESCAYG, A., MEISLER, M.H. & GOLDIN, A.L. (2003). Generalized epilepsy with febrile seizures plus type 2 mutation w1204r alters voltage-dependent gating of na(v)1.1 sodium channels. *Neuroscience*, **116**, 37–48. 118

SPAMPANATO, J., ARADI, I., SOLTESZ, I. & GOLDIN, A.L. (2004). Increased neuronal firing in computer simulations of sodium channel mutations that cause generalized epilepsy with febrile seizures plus. *J Neurophysiol*, **91**, 2040–50. 118

STASHEFF, S.F. (2008). Emergence of sustained spontaneous hyperactivity and temporary preservation of off responses in ganglion cells of the retinal degeneration (rd1) mouse. *J Neurophysiol*, **99**, 1408–21. 120

STERLING, P. & MATTHEWS, G. (2005). Structure and function of ribbon synapses. *Trends Neurosci*, **28**, 20–9. 39

STINGL, K., BARTZ-SCHMIDT, K.U., BESCH, D., BRAUN, A., BRUCKMANN, A., GEKELER, F., GREPP-MAIER, U., HIPP, S., HÖRTDÖRFER, G., KERNSTOCK, C., KOITSCHEV, A., KUSNYERIK, A., SACHS, H., SCHATZ, A., STINGL, K.T., PETERS, T., WILHELM, B. & ZRENNER, E. (2013). Artificial vision with wirelessly powered subretinal electronic implant alpha-ims. *Proc Biol Sci*, **280**, 20130077. 3, 58, 64

STRONKS, H.C. & DAGNELIE, G. (2014). The functional performance of the argus ii retinal prosthesis. *Expert Rev Med Devices*, **11**, 23–30. 122

TAHAYORI, B., MEFFIN, H., DOKOS, S., BURKITT, A.N. & GRAYDEN, D.B. (2012). Modeling extracellular electrical stimulation: Ii. computational validation and numerical results. *J Neural Eng*, **9**, 065006. 17

TAHAYORI, B., MEFFIN, H., SERGEEV, E.N., MAREELS, I.M.Y., BURKITT, A.N. & GRAYDEN, D.B. (2014). Modelling extracellular electrical stimulation: part 4. effect of the cellular composition of neural tissue on its spatio-temporal filtering properties. *J Neural Eng*, **11**, 065005. 23

TEETERS, J., JACOBS, A. & WERBLIN, F. (1997). How neural interactions form neural responses in the salamander retina. *J Comput Neurosci*, **4**, 5–27. 131

THOMAS, L. (1949). Elliptic problems in linear differential equations over a network. Tech. rep., Columbia University, New York. 30

THOMSON, W. (1854). On the theory of the electric telegraph. *Proceedings of the Royal Society of London*, **7**, 382–399. 17

THORESON, W.B. (2000). Dihydropyridine-sensitive calcium currents in bipolar cells of salamander retina are inhibited by reductions in extracellular chloride. *Neurosci Lett*, **280**, 155–8. 37

THYAGARAJAN, S., VAN WYK, M., LEHMANN, K., LÖWEL, S., FENG, G. & WÄSSLE, H. (2010). Visual function in mice with photoreceptor degeneration and transgenic expression of channelrhodopsin 2 in ganglion cells. *J Neurosci*, **30**, 8745–58. 120

TOCHITSKY, I., POLOSUKHINA, A., DEGTYAR, V.E., GALLERANI, N., SMITH, C.M., FRIEDMAN, A., VAN GELDER, R.N., TRAUNER, D., KAUFER, D. & KRAMER, R.H. (2014). Restoring visual function to blind mice with a photoswitch that exploits electrophysiological remodeling of retinal ganglion cells. *Neuron*, **81**, 800–13. 2

TOLIAS, A.S., SULTAN, F., AUGATH, M., OELTERMANN, A., TEHOVNIK, E.J., SCHILLER, P.H. & LOGOTHETIS, N.K. (2005). Mapping cortical activity elicited with electrical microstimulation using fmri in the macaque. *Neuron*, **48**, 901–911. 69

TREXLER, E.B., LI, W. & MASSEY, S.C. (2005). Simultaneous contribution of two rod pathways to aii amacrine and cone bipolar cell light responses. *J Neurophysiol*, **93**, 1476–85. 56

TSAI, D., MORLEY, J.W., SUANING, G.J. & LOVELL, N.H. (2009). Direct activation and temporal response properties of rabbit retinal ganglion cells following subretinal stimulation. *J. Neurophysiol.*, **102**, 2982–2993. 67, 81, 82, 83, 114, 116, 120, 125

TSAI, D., CHEN, S., PROTTI, D.A., MORLEY, J.W., SUANING, G.J. & LOVELL, N.H. (2012). Responses of retinal ganglion cells to extracellular electrical stimulation, from single cell to population: model-based analysis. *PLoS One*, **7**, e53357. 115, 126

TWYFORD, P., CAI, C. & FRIED, S. (2014). Differential responses to high-frequency electrical stimulation in on and off retinal ganglion cells. *J Neural Eng*, **11**, 025001. 10, 124

REFERENCES

Usui, S., Ishihara, A., Kamiyama, Y. & Ishii, H. (1996). Ionic current model of bipolar cells in the lower vertebrate retina. *Vision Res.*, **36**, 4069–4076. 70

Van Wart, A., Trimmer, J.S. & Matthews, G. (2007). Polarized distribution of ion channels within microdomains of the axon initial segment. *J Comp Neurol*, **500**, 339–52. 10, 40, 74, 117, 118

Veraart, C., Raftopoulos, C., Mortimer, J.T., Delbeke, J., Pins, D., Michaux, G., Van-lierde, A., Parrini, S. & Wanet-Defalque, M.C. (1998). Visual sensations produced by optic nerve stimulation using an implanted self-sizing spiral cuff electrode. *Brain Res*, **813**, 181–6. 2

Villalobos, J., Nayagam, D.A.X., Allen, P.J., McKelvie, P., Luu, C.D., Ayton, L.N., Free-mantle, A.L., McPhedran, M., Basa, M., McGowan, C.C., Shepherd, R.K. & Williams, C.E. (2013). A wide-field suprachoroidal retinal prosthesis is stable and well tolerated following chronic implantation. *Invest Ophthalmol Vis Sci*, **54**, 3751–62. 3

von Gersdorff, H., Vardi, E., Matthews, G. & Sterling, P. (1996). Evidence that vesicles on the synaptic ribbon of retinal bipolar neurons can be rapidly released. *Neuron*, **16**, 1221–7. 39

Walston, S.T., Chow, R.H. & Weiland, J.D. (2015). Patch clamp recordings of retinal bipolar cells in response to extracellular electrical stimulation in wholemount mouse retina. In *2015 37th Annual International Conference of the IEEE Engineering in Medicine and Biology Society (EMBC)*, 3363–3366. 70

Wan, Q.F. & Heidelberger, R. (2011). Synaptic release at mammalian bipolar cell terminals. *Vis Neurosci*, **28**, 109–19. 39

Wan, Q.F., Vila, A., Zhou, Z.Y. & Heidelberger, R. (2008). Synaptic vesicle dynamics in mouse rod bipolar cells. *Vis Neurosci*, **25**, 523–33. 39, 69

Wan, Q.F., Zhou, Z.Y., Thakur, P., Vila, A., Sherry, D.M., Janz, R. & Heidelberger, R. (2010). Sv2 acts via presynaptic calcium to regulate neurotransmitter release. *Neuron*, **66**, 884–95. 39

Wässle, H. (2004). Parallel processing in the mammalian retina. *Nat Rev Neurosci*, **5**, 747–57. 7

Wässle, H., Puller, C., Müller, F. & Haverkamp, S. (2009). Cone contacts, mosaics, and territories of bipolar cells in the mouse retina. *J Neurosci*, **29**, 106–17. 6

Weitz, A.C., Nanduri, D., Behrend, M.R., Gonzalez-Calle, A., Greenberg, R.J., Humayun, M.S., Chow, R.H. & Weiland, J.D. (2015). Improving the spatial resolution of epiretinal implants by increasing stimulus pulse duration. *Sci Transl Med*, **7**, 318ra203. 64

Werginz, P. & Rattay, F. (2015). Past, present, future: a review on visual prostheses. *Minerva Med*, **106**, 65–77. 2, 4, 14

Werginz, P., Benav, H., Encke, J., Zrenner, E. & Rattay, F. (2013). Neural activation for different electrode designs in subretinal implants: a modeling study. *Biomed Tech (Berl)*. 14, 35

WERGINZ, P., FRIED, S.I. & RATTAY, F. (2014). Influence of the sodium channel band on retinal ganglion cell excitation during electric stimulation–a modeling study. *Neuroscience*, **266**, 162–77. 11, 68, 118, 125, 126, 127

WERGINZ, P., BENAV, H., ZRENNER, E. & RATTAY, F. (2015). Modeling the response of on and off retinal bipolar cells during electric stimulation. *Vision Res*, **111**, 170–81. 10, 14, 35, 47, 66, 125

WILEY, J.D. & WEBSTER, J.G. (1982). Analysis and control of the current distribution under circular dispersive electrodes. *IEEE Trans Biomed Eng*, **29**, 381–5. 90

WILKE, R.G.H., MOGHADAM, G.K., LOVELL, N.H., SUANING, G.J. & DOKOS, S. (2011). Electric crosstalk impairs spatial resolution of multi-electrode arrays in retinal implants. *J Neural Eng*, **8**, 046016. 13, 130

WOLLNER, D.A. & CATTERALL, W.A. (1986). Localization of sodium channels in axon hillocks and initial segments of retinal ganglion cells. *Proc Natl Acad Sci U S A*, **83**, 8424–8. 10

WONG, W.L., SU, X., LI, X., CHEUNG, C.M.G., KLEIN, R., CHENG, C.Y. & WONG, T.Y. (2014). Global prevalence of age-related macular degeneration and disease burden projection for 2020 and 2040: a systematic review and meta-analysis. *Lancet Glob Health*, **2**, e106–16. 8

Y CAJAL, R. (1893). La retine des vertebres. *Cellule*, **9**, 119–255. 5

ZHOU, Z.Y., WAN, Q.F., THAKUR, P. & HEIDELBERGER, R. (2006). Capacitance measurements in the mouse rod bipolar cell identify a pool of releasable synaptic vesicles. *J Neurophysiol*, **96**, 2539–48. 39

ZRENNER, E. (2013). Fighting blindness with microelectronics. *Sci Transl Med*, **5**, 210ps16. 2

ZRENNER, E., RÜTHER, K. & APFELSTEDT-SYLLA, E. (1992). Retinitis pigmentosa. clinical findings, results of molecular genetic techniques and research perspectives. *Ophthalmologe*, **89**, 5–21. 8

REFERENCES

Appendix A

Description of the framework

As described in chapter 2 a framework was established able to compute the response of neurons to intra- and extracellular stimulation fast and accurately. The following sections present all major components of the framework and describes their usage and functionality.

Parameter specification

The following information has to be provided to the framework prior to computation.

- file name of morphology file (.swc)

- intracellular (axial) resistivity

- specific membrane capacitance

- stimulation mode

  - extracellular stimulation

  - intracellular stimulation (current clamp)

  - voltage clamp

- stimulation paradigm

  - single pulse

  - biphasic pulse

  - repetitive stimulation

- stimulus amplitude and location

- somatic geometry (sphere or cylinder)

- temperature

- resting potential

- ion channel densities

- temporal parameters (delay, stimulus duration, total duration)

- plot flags

- for extracellular stimulation only

  - analytical or numerical solution

  - extracellular resistivity

  - sub- or epiretinal stimulation

All data are stored in four structs. *Neuron* stores data which is related to the neuron, *Stim* contains stimulus data, *Solution* stores the solution and *Plot* has all plot attributes in it. The solution contains membrane voltage, ion currents and gating states for each compartment over time as well as the activating function and the stimulus current at each compartment. The solution from BC computations additionally implies intracellular calcium concentration and synaptic release for each terminal compartment.

Program execution

The main file executes all procedures necessary for computation. After initialization of all parameters (initializeParameters.m) the Hines ordering procedure is executed (computeHines.m). After computation of geometric parameters such as compartment length, surface, volume etc. (computeGeometry.m) extracellular potentials (only if in extracellular mode) at compartment centers are calculated (computePotentials.m). After computing all electric parameters (computeElectric.m) the solver is called which further calls C files via MATLABs **MEX** (**M**ATLAB **EX**ecutable) interface (solveODE.m). After obtaining the solution the plot function is called to visualize the output (plotResults.m).

```matlab
% Main file
clear all

% Timer
totalTime = tic;

% Initialization of parameters
[Neuron,Stim,Plot] = initializeParameters();

% Hines ordering of .swc file and computation of neigborhood matrix
Neuron = computeHines(Neuron,Stim);
% Compute geometry parameters
Neuron = computeGeometry(Neuron);
% Compute external potentials
Neuron = computePotentials(Neuron,Stim);
% Compute electrical parameters
Neuron = computeElectric(Neuron);
% Compute cell response (solve ODE) and plot results
[Solution,Neuron] = solveODE(Neuron,Stim);
```

```
plotResults(Solution,Stim,Neuron,Plot);

% Display computation time
Solution.totalTime = toc(totalTime);
clear totalTime;
fprintf('Total time was %.3fs. \n',Solution.totalTime)
```

COMSOL model

In contrast to the previously presented analytical solution for the potential distribution in a homogeneous volume (see section 2.3) COMSOL Multiphysics allows to compute the solution for more complicated problems including arbitrary volume geometries as well as elaborated electrode configurations.

The used version of COMSOL Multiphysics (4.4) incorporates an easy to handle user interface which facilitates the generation of simple models in a short amount of time. After choosing the intended space dimension (3D), physics (Electric currents (ec)) and study type (stationary), the volume to be modeled is drawn in the CAD editor and material properties are applied. In a next step suitable boundary conditions are chosen. In all computations the external boundaries were set to ground and the electrode carrier was electrically insulated. The following mesh process consists of selecting a predefined element (tetrahedrons) size. After solving the model multiple plot, evaluation and export options are available. Computed solutions, i.e. potentials on a user-defined three-dimensional grid (10µm spacing in x-, y- and z-direction) in the volume, were stored in .txt files in grid (i.e. two-dimensional matrix) format. These .txt files were converted to .mat files containing a three-dimensional matrix filled with the electric potential at each coordinate in space. In order to obtain electric potentials at coordinates in between stored grid points MATLABs *interp3* function (method *cubic*) was used.

Availability

If anyone is interested in the framework in more detail I will be happy to share parts of the source code. Please feel free to contact me at paul.werginz@tuwien.ac.at.

A. DESCRIPTION OF THE FRAMEWORK

Appendix B

Curriculum Vitae

Profile

Paul Werginz
Wimbergergasse 42/11
1070 Vienna, Austria

Tel.: +43 1 58801 10166
Email: paul.werginz@tuwien.ac.at

Date of Birth: 14.07.1986, Klagenfurt
Nationality: Austria

Education

| since 04/13 | Doctoral student (Dr. techn., PhD) - *Engineering Sciences* |
| | Vienna University of Technology |

| 04/10 - 04/12 | Masters degree (Dipl.-Ing., MSc) - *Biomedical Engineering* |
| | Vienna University of Technology |

| 10/06 - 03/10 | Bachelors degree (BA) - *Biomedical Informatics* |
| | Vienna University of Technology |

B. CURRICULUM VITAE

10/04 - 12/05	Medical studies (not completed)
	Medical University Graz
09/96 - 06/04	Secondary school
	Bundesrealgymnasium Feldkirchen, Carinthia

International Experience

02/11 - 08/11	Research scholar at Fried-Lab, Harvard Medical School, Boston, MA (USA), Masters thesis *Influence of the sodium channel band on retinal ganglion cell excitation during electric stimulation - A computer simulation*

Scholarships

02/11 - 08/11	Marshall-Plan Scholarship, Austrian Marshall Plan Foundation

Funding

09/14 - 08/17	Co-author of project *Selective cell stimulation with retinal implants*, Austrian Science Fund, P27335-B23.

Work Experience

since 07/14	Project Assistant (Austrian Science Fund). Vienna University of Technology, Institute for Analysis and Scientific Computing
since 04/10	Private tutor in Mathematics and Physics
09/11 - 06/14	Project work with Prof. Rattay at Vienna University of Technology, Modeling of the response of retinal neurons during electric stimulation

Invited Talks

03/17/15   *Biophysical based models of extracellular electric stimulation of the retina*, Departmental seminar, Institute for Ophthalmic Research, University Hospital Tuebingen

Papers in Peer-reviewed Journals

2016   **Werginz P.**, Rattay F., 2016. *The impact of calcium current reversal on neurotransmitter release in the electrically stimulated retina.* in review

2015   **Werginz P.**, Benav H., Zrenner E., Rattay F., 2014. *Modeling the response of ON and OFF retinal bipolar cells during electric stimulation.* Vision Res. 111, pp. 170-181, doi:10.1016/j.visres.2014.12.002

2015   **Werginz P.**, Rattay F., 2015. *Past, present, future: A review on visual prostheses.* Minerva Med 105, pp. 65-77

2014   **Werginz P.**, Fried S.I., Rattay F., 2014. *Influence of the sodium channel band on retinal ganglion cell excitation during electric stimulation - A modeling study.* Neuroscience 266, pp. 162-77, doi:10.1016/j.neuroscience.2014.01.067

Papers in Conference Proceedings

2013   **Werginz P.**, Benav H., Encke J., Zrenner E., Rattay F., 2013. *Neural activation for different electrode designs in subretinal implants: A modeling study.* Biomed Tech (Berl), doi:10.1515/bmt-2013-4036

2013   Encke J., Benav H., **Werginz P.**, Zrenner E., Rattay F., 2013. *Investigating the influence of 3D cell morphology on neural response during electrical stimulation.* Biomed Tech (Berl), doi:10.1515/bmt-2013-4035

Conference Contributions / Poster Presentations

2016	**Werginz P.**, Hadjinicolaou A.E., Fried S.I., Rattay F., 2016. *Focal activation of retinal ganglion cells with epiretinal implants: The AIS as a key component.* Annual meeting ARVO 2016, Seattle, WA
2016	Hadjinicolaou A.E., **Werginz P.**, Raghuram V., Rattay F., Fried S.I., 2016. *Sodium channel band expression in the AIS: Fundamentals of activation threshold.* Annual meeting ARVO 2016, Seattle, WA
2015	**Werginz P.**, Encke J., Jalligampala A., Rathbun DL., Rattay F., 2015. *Modeled direct and indirect activation of retinal ganglion cells during subretinal stimulation.* Invest Ophthalmol Vis Sci. 56(7), E-Abstract 771. Annual meeting ARVO 2015, Denver, CO
2010	Benav H., Rattay F., Wilke R., Feiertag D., Freystätter C., Kitzler G., **Werginz P.**, Zrenner E., 2010. *Modeled responsivity of retinal bipolar cells during subretinal stimulation.* Invest Ophthalmol Vis Sci. 51(13), E-Abstract 3035. Annual meeting ARVO 2010, Fort Lauderdale, FL

Teaching

2015W	Rattay F., **Werginz P.**, *Computer simulation in medicine*, Lecture with demonstrations (VU 101.498, 2 ECTS), Vienna University of Technology
2015W	Rattay F., **Werginz P.**, *Computer simulation in medicine*, Exercise (UE 101.529, 3 ECTS), Vienna University of Technology